Cold Gas Dynamic Spray Additive Manufacturing of Moisture-Electric Energy Transformation Devices

By

Amir Daoud

Thesis submitted to the Department of Mechanical Engineering in partial fulfillment of the requirements for the degree of

Master of Applied Science

in Mechanical Engineering

University of Ottawa

Ottawa, Ontario, Canada

September 4th, 2019

Abstract

The ever-growing Internet of Things is promoting more data acquisition, data exchange and fewer human interactions, engendering a higher demand for sensors and therefore power. While in most cases it is possible to directly connect these sensors to the power grid, it will not always be feasible with emerging technologies, especially in remote areas where human access is limited.

Moisture-Electric Energy Transformation (MEET) devices are components that use moisture as a “fuel” to generate electrical power. Upon contact with moisture, a potential difference results from a diffusion mechanism, allowing charge to be stored locally in capacitors or rechargeable batteries to be utilized for useful work.

The focus of the present work was to investigate the potential of Cold Gas Dynamic Spray (CGDS) as an additive manufacturing (AM) process for the fabrication of MEET devices. Following a layer-by-layer approach, MEET devices were successfully built by CGDS, by combining aluminum (electrode material) and an in-situ composite of polyether ether ketone (PEEK) and alumina (diffusion medium).

The main challenges of this work were the determination of the spray parameters of PEEK and the investigation of the MEET capability of the manufactured devices. On the other hand, the main contributions of this work were the demonstration of the viability of CGDS in the deposition of PEEK/Al_2O_3 on aluminum 6061-T6 substrates, as well as the potential of PEEK as a MEET-capable material. The diffusion mechanisms that govern power generation were also hypothesized, explained and summarized.

Initial tests of a MEET device of 66 mm x 34 mm indicate an uninterrupted power generation cycle of over 30 hours, and a maximum output voltage of 268 mV with a 6.8 MΩ load. The output power and power per unit area of the device were computed to be 10.63 nW and 4.736 $\mu W/m^2$ respectively. The output current and current density were evaluated to 39.53 nA and 17.62 $\mu A/m^2$.

Acknowledgements

First, I would like to take this opportunity to express my gratitude and appreciation to my thesis supervisor, Professor Bertrand Jodoin. His guidance and encouragement over the last two years have been essential. Thank you for being a mentor and for having such a positive influence on my life. It was a real honour and a privilege to work with you. *Chapeau bas!*

I would also like to thank NSERC and the University of Ottawa for their financial support.

I wish to acknowledge the help provided by the technicians from the machine shop at the University of Ottawa. I would especially like to thank Stan and Jacques for their speed and precision. Your skills were crucial in completing this work.

I would like to thank my colleagues for making this an amazing and fun experience both inside and outside of the lab. Saeed Rahmati, Samuel Croteau, Maryam Razavipour, Daniel MacDonald, Roghayeh Nikbakht, Aleksandra Nastic, Mathieu Hinse, Rocio Dominguez, Justin Perry, Deliang (Leon) Goudl, and Roberto Fernandez. Thank you for your help with this project.

Lastly, I wish also to thank my family for their unconditional support and encouragement during my studies. I couldn't have done it without you.

Ce travail t'est dédié, papa.

Table of Contents

List of Figures

List of Tables

1 Introduction

1.1 Background

The Internet of Things (IoT) is a network of smart connected devices and systems that exchange data acquired from actuators and sensors in machines and other objects. The aim of enabling devices to communicate independently of human interaction is to facilitate data exchange, generate new revenue sources and favour efficiency [1]. IoT devices have a wide range of applications: they can be used at home to understand human activities and adjust lighting and temperature to minimize energy consumption, in cities to monitor air quality and implement efficient lighting, as well as in agriculture to monitor soil conditions and control watering and pesticide spraying [2]–[6]. **Figure 1.1** shows some potential applications of the IoT.

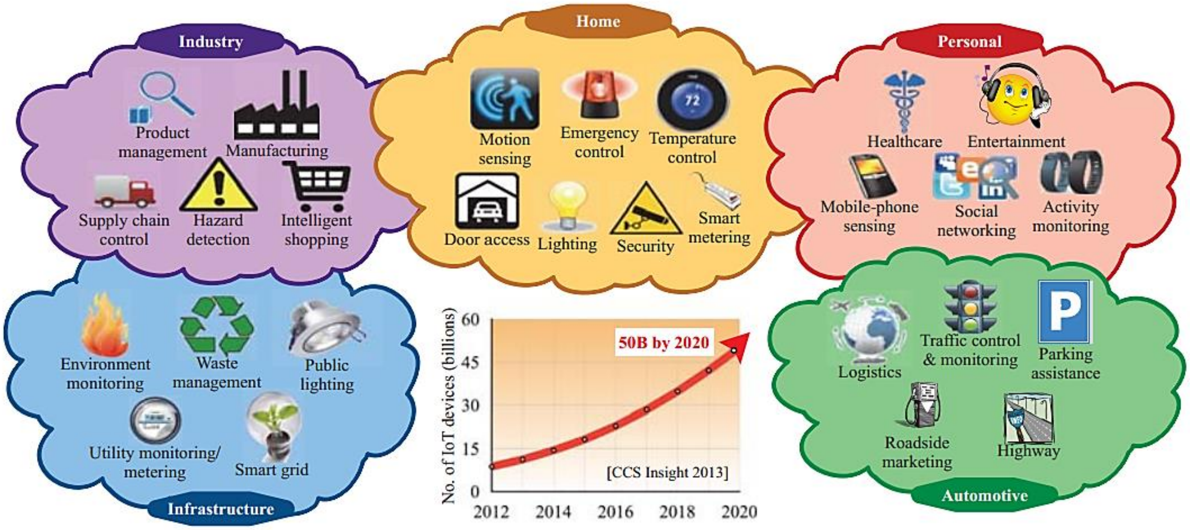

Figure 1.1. An overview of the current and future applications, as well as the growth projections of the IoT [7] (© 2014 Hrishikesh Jayakumar).

As the IoT promotes more independence from human interaction, the need for more sensory and communication functionalities gives rise to a higher demand for energy [4], [5], [8]. Consequently, efforts are made to develop more energy efficient components by miniaturization [9]. Moreover, the development of the IoT and the rising awareness about global warming and cleaner energy sources [10] paves the path for the development of more creative methods to harvest energy from the environment such as thermal gradients, electromagnetic radiation (light and RF waves) and mechanical motion [2], [5], [7], [8], [11]. **Figure 1.2** shows the design of a shoe that scavenges mechanical and vibrational energy from the human body through the use of piezoelectric materials.

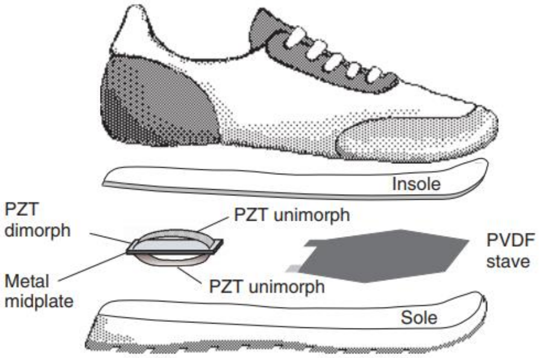

Figure 1.2. Piezoelectric energy harvesting in a shoe by using a lead zirconate titanate (PZT) dimorph under the heel or a polyvinylidene fluoride (PVDF) stave under the toes [12] (© 2001 IEEE).

Since 2014, moisture-electric energy transformation (MEET) technology has emerged as a new approach to energy scavenging from environmental moisture and water droplets. The fundamental mechanism of this technology lies in the extraction of electrical power from the diffusion of hydrogen ions (H^+) that get released by some materials upon exposure to moisture. Despite focusing mostly on carbon-based materials, different configurations and preparation methods have been investigated, showing great promise in regards to power and efficiency figures [13]–[20].

The development of interesting water-collection methods like the Warka Tower is an excellent opportunity to democratize MEET technology and put it to use in isolated communities. Built specifically in remote areas where access to water is limited and infrastructure non-existent, Warka Towers provide potable water at no energy cost by collecting rain and harvesting fog and dew through natural phenomena such as gravity, condensation and evaporation. These towers can produce up to 80 litres of water a day and therefore, can house MEET technology to harvest energy from the available humid air and water. This combination would provide the isolated communities with electrical energy to facilitate education, communication and improve the standards of living in general [21]. **Figure 1.3** shows a picture of a Warka Tower and condensed water droplets on its polyester mesh.

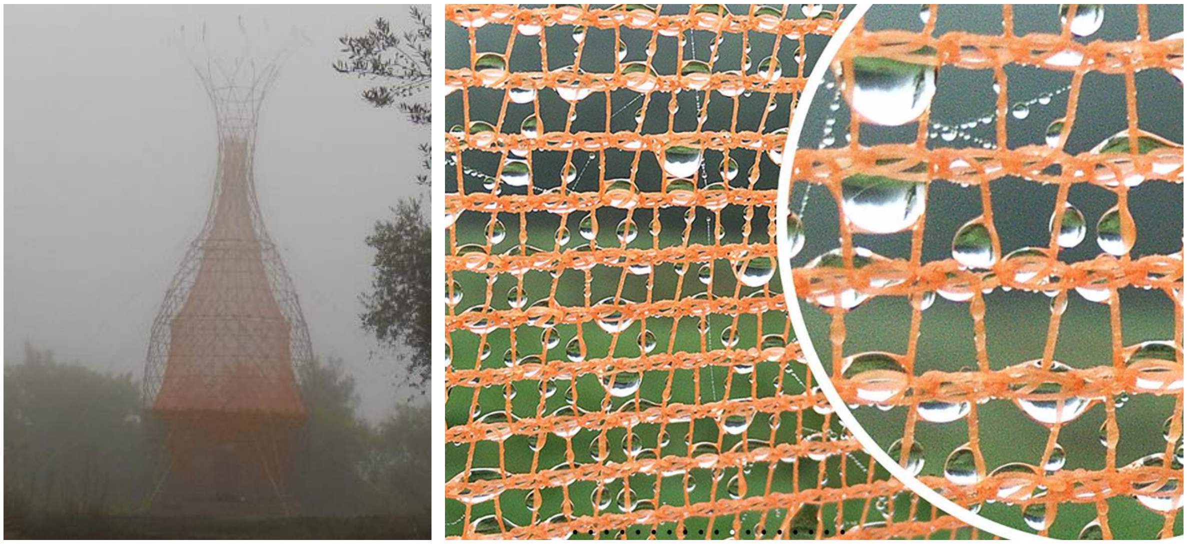

Figure 1.3. Picture of a Warka Tower (left) and the condensation of water droplets on the polyester mesh used to build the tower (right) [21] (© 2017 Arturo Vittori).

Polyether ether ketone (PEEK) has promising potential to be a MEET material because of its chemistry and its excellent mechanical, thermal and electrical properties. Despite its high cost, its resistance to chemical degradation makes it an excellent solution for MEET applications, including in high temperature environments. Additionally, PEEK's water sorption and desorption properties make it a suitable material for long-term power generation as its time to saturation in water is considerably long [22]–[31]. Such an attribute is crucial because it allows the generation of a DC current for long periods of time, unlike the carbon-based materials that are currently used and that can only generate DC current for short intervals (a few minutes), before polarity reversal or saturation take place [13]–[20].

Currently proposed methods to build MEET devices use multiple chemical processes or a combination of chemical and electrical processes that can be hard to scale up for large volume production [13]–[20]. It is believed that Cold Gas Dynamic Spray (CGDS), or Cold Spray (CS), is a simpler process for the production of MEET devices that can be adapted to large-scale manufacturing. It is also a green process as it uses air or nitrogen gas and electricity, and has shown promise in regards to powder recycling [32].

CGDS additive manufacturing (AM) applications have been studied and are for the most part focused on the repair of components [33]–[38] and the production of heat exchangers [39]–[43]. Nevertheless, the improvement of the process and the enhanced understanding of its fundamentals are extending its use to the production of near-net shape parts with minimal machining [33].

Hence, the objective of this research is to investigate the AM potential of the CGDS process for the manufacturing of PEEK-based MEET devices.

1.2 Motivation and Objectives

The present study was motivated by the use of the CGDS process in the manufacturing of MEET devices. The first objective of this research was to achieve successful deposition of PEEK on aluminum substrates by using commercially available CGDS apparatus and feedstock powders. Subsequently, the goal of this work was to test the PEEK-based MEET device and characterize its properties by performing data acquisition.

In order to complete the objectives of this research, the following steps were followed:

1) The spray parameters of PEEK and PEEK composites on aluminum substrates with different surface preparations were investigated.
2) The effects of the size of the substrate and substrate preheating were studied in an effort to achieve process repeatability.
3) The electrical properties of the MEET device were evaluated after performing data acquisition with Arduino.

1.3 Thesis Arrangement

The content of this thesis is arranged in seven chapters. **Chapter 1** presents the motivating factors and goals of this work, as well as a general introduction to the research topics of the thesis.

An up to date summary of relevant literature is presented in **Chapter 2**. The first section provides a background on MEET Technology and its working principles. The second section of the literature review gives an overview of PEEK as well as its mechanical and water sorption properties that make it a candidate for MEET applications. The third section briefly discusses aluminum use in electrical components and finally, the last section gives an overview of the CGDS process and its fundamental concepts.

Chapter 3 outlines the specific objectives of this research. This chapter provides a detailed plan to reach the main objective of this thesis, by specifying the challenges related to this work and the steps undertaken to overcome them.

Chapter 4 provides detailed information related to the experimental procedures, materials, equipment and characterization tools used to satisfy the research objectives.

Chapter 5 details the experimental design, including the CGDS parameters, surface preparation and other iterations undertaken towards satisfying the main objectives of this work from a CGDS standpoint. It also provides the detailed data acquisition setup and parameters used for the measurement of the output voltage of the MEET device. The results and discussion of each step are provided in this section.

Finally, **Chapter 6** presents a summary of the findings of this work. It also provides a list of recommendations for future work that should be undertaken in order to further the research. A list of references and appendices follow this chapter.

2 Literature Review

2.1 MEET Technology

2.1.1 Background

MEET is a recent technology that drew considerable attention starting from 2014 [13]. Before its advent, successful attempts to extract power from environmental energy were made: piezoelectric [12], [44]–[48], and more recently triboelectric [49]–[54] and fluidic electric [20], [55]–[59] materials were developed to take advantage of vibration, friction and water-flow-induced ion distribution to generate electricity.

MEET technology was developed in an effort to further expand our utilization of environmental energy sources like thermal power, hydropower, wind power and solar energy. The goal of the development of such a technology was to extract power from environmental moisture with as few conversion processes as possible to satisfy an ever-growing demand for new and more portable energy sources [13]–[17], [60].

2.1.2 Working Principles

2.1.2.1 Hydrogen Ion Gradient Establishment and Ion Migration

The materials used in the manufacturing of MEET devices are prepared and disposed in such a way that a gradient of H^+ ions is established through their thickness upon exposure to water or moisture. To guarantee such a gradient, hydrogen-releasing functional groups must be present through the thickness of the MEET device with an increasing/decreasing concentration, commonly oxygen-rich carboxyl (-COOH) and hydroxyl groups (-OH) [13]–[17], [60] as shown in **Figure 2.1.**

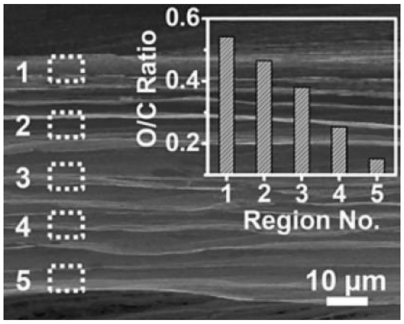

Figure 2.1. Cross-sectional scanning electron microscope (SEM) image with X-ray energy dispersive spectroscopy (EDS) inset, showing the decreasing oxygen-to-carbon (O/C) ratio through the thickness of a graphene-oxide-based MEET device [16] (© 2016 John Wiley & Sons).

Water sorption occurs in the hydrophilic oxygen-rich parts of the MEET device. Water molecules cause the local solvation of the oxygen-containing groups, weakening the bonds between the oxygen $O^{\delta-}$ and the hydrogen $H^{\delta+}$ in the carboxyl or hydroxyl groups and freeing a hydrogen ion or proton (H^+) from the molecule. The negatively charged oxygen atoms O^- remain stationary as they are linked to large molecules. Subsequently, the protons migrate from the oxygen-rich (and thus proton-rich) side to the low-concentration side through a diffusion mechanism, giving rise to an electrical current [13]–[17], [60]. The hydration process as well as the diffusion mechanism are shown in **Figure 2.2**.

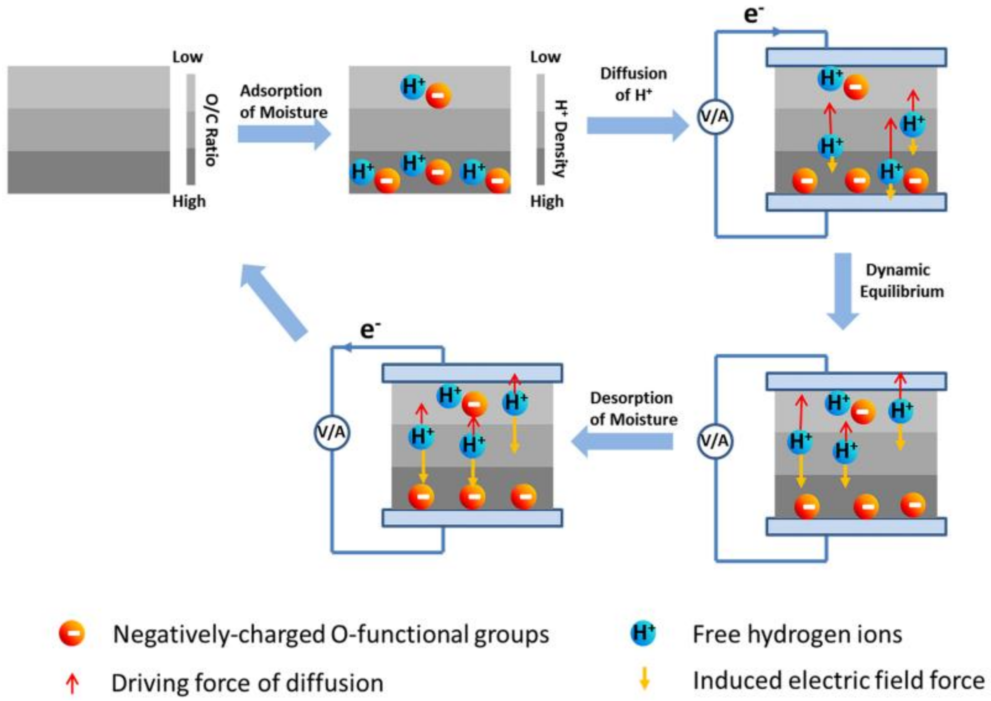

Figure 2.2. Schematic of the hydration of a graphene-oxide-based MEET device [18] (© 2018 Springer Nature).

As the hydrogen ion migration process takes place, and even if moisture keeps being added to the device, the H$^+$ and O$^-$ ions become fully separated and a dynamic balance is reached. In other words, the force applied by the electric field induced by the negatively charged oxygen-rich functional groups and the diffusion force reach equal magnitudes [13]–[15], [18], [61]. The hydrogen ions' movement is therefore impeded, resulting in the voltage dropping to zero, and sometimes pole reversal (negative voltage) as evaporation takes place, as shown in **Figure 2.3**.

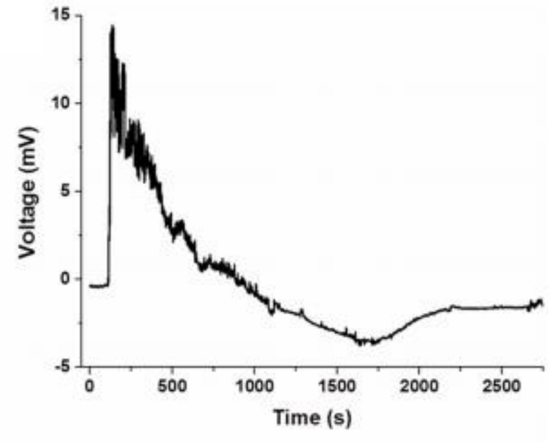

Figure 2.3. Voltage response of a gradient polyoxometalates-modified sponge-like graphene oxide monolith as a function of time, under a relative humidity of 80% [18] (© 2018 Springer Nature).

Desorption of moisture from the MEET device may be achieved by exposing it to dry air, causing the generation of a reverse voltage. This is explained by the recombination of the oxygen-containing groups (like $-COO^-$) and H^+, as the protons travel in the opposite direction as opposed to the hydration process. Design variations that allow evaporation to enhance the process exist, by constantly removing water molecules from the film, thus preventing dynamic balance from occurring and allowing direct-current same-sign voltage generation [13]–[15], [18], [61].

2.1.2.2 Water-Evaporation Induced Electricity Generation

Water-evaporation-induced electricity generating components rely on the same previously explained H^+ diffusion mechanism to generate electricity. However, they are partially submerged in water and use a combination of capillary flow and evaporation to generate a gradient of H^+ ions within the film. The bottom electrodes are connected to the submerged part of the film and therefore contain a large concentration of H^+ ions. Water molecules travel up the film via capillary action, resulting in a decrease in proton concentration along the height of the component. The top electrode is connected to the top part of the film where H^+ concentration is low. Exposure of the film to atmospheric air, excluding the bottom electrode, causes water evaporation which prevents dynamic balance from occurring [61]. **Figure 2.4** shows four of these components connected in series.

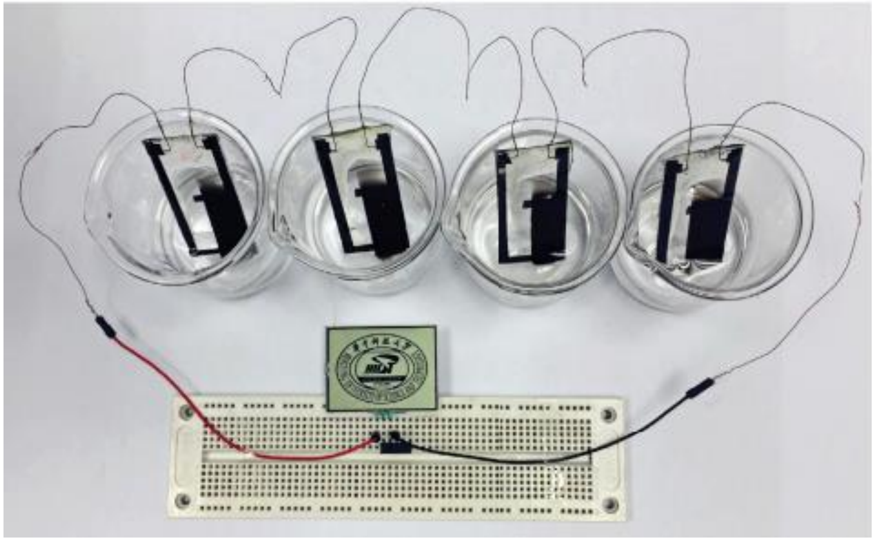

Figure 2.4. Photograph of four water-evaporation-induced electricity generating devices connected in series [61] (© 2017 Springer Nature).

Figure 2.5 illustrates the effects of the diffusion of water by capillary action on the recorded voltage between neighbouring electrodes numbered from 1 to 7. Electrodes 1 and 2 are both submerged in water and electrodes 3 to 7 are exposed to dry air. It can be seen from the figure that in the absence of evaporation, the voltage between two adjacent electrodes is zero (electrodes 1 and 2). The voltage across each pair of neighbouring electrodes increases along the height of the MEET device because the evaporation rate increases as the capillary height increases ($V_{2\text{-}3}$, $V_{3\text{-}4}$, $V_{4\text{-}5}$ and $V_{5\text{-}6}$). However, at some point, capillary water cannot travel past the sixth electrode and therefore $V_{6\text{-}7}$ is zero. Finally, $V_{1\text{-}7}$ is the voltage difference between the bottommost and topmost electrodes: it is essentially the addition of all the previous voltages shown on the figure [61].

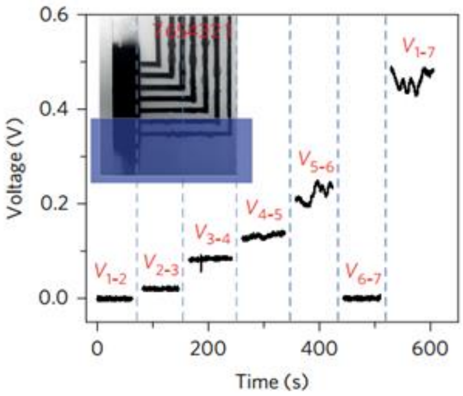

Figure 2.5. Saturated voltage differences between neighbouring electrodes and between electrodes (1) and (7). The space between the electrodes is fixed to 5 mm [61] (© 2017 Springer Nature).

2.1.2.3 Relative Humidity Effects

For water-evaporation-induced electricity generating components, dryer air promotes more evaporation and therefore, causes more H^+ to migrate from the submerged electrode to the top electrode. Since more water molecules are removed at the top electrode, the driving force for diffusion is enhanced, thus producing a higher output voltage [61]. **Figure 2.6** displays the output voltage of a water-evaporation-induced electricity generating component exposed to different levels of relative humidity (RH).

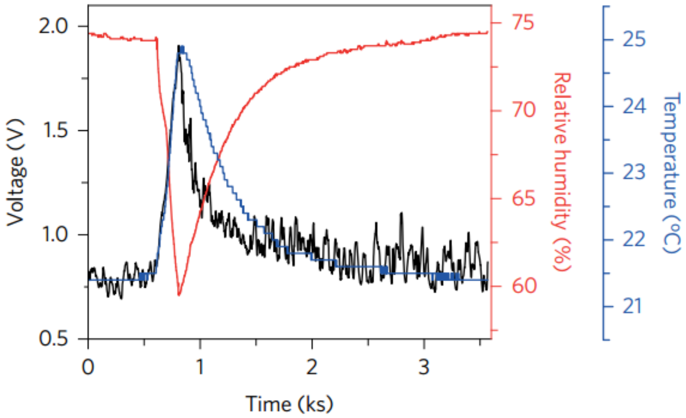

Figure 2.6. Open-circuit voltage of a water-evaporation-induced electricity generating device under varying RH conditions [61] (© 2017 Springer Nature).

Moreover, the volumetric flowrate of dry gas circulating at the top end of the device has an impact on the output voltage of water-evaporation-induced electricity generating components. An increase in the flowrate results in a higher evaporation rate of H_2O molecules from the top electrode, therefore increasing the driving force for diffusion and resulting in higher voltages as seen in **Figure 2.7.**

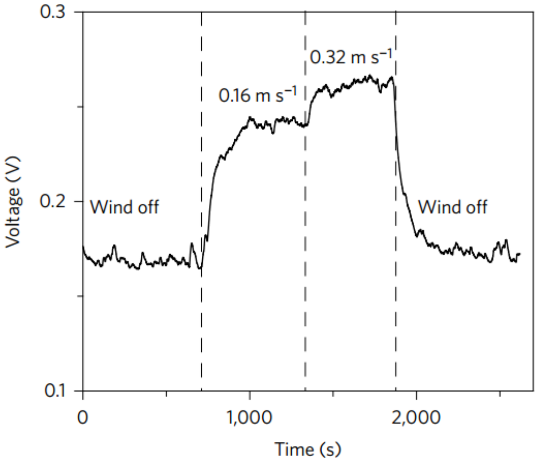

Figure 2.7. Open-circuit voltage output of a water-evaporation-induced electricity generating device under varying flowrates for a fixed RH [61] (© 2017 Springer Nature).

RH is an important parameter for the operation of MEET devices. As the RH of the moisture-laden gas increases with respect to the initial environmental humidity, the output voltage of the devices increases until saturation of the film. This can be explained by the fact that more water molecules infiltrate the film with higher RH values, resulting in a higher concentration of H^+ ions [13]–[16], [60].

Figure 2.8 shows the output voltage and current density of a graphene oxide nanoribbon MEET device after RH was increased from 5% to 35% as a function of time.

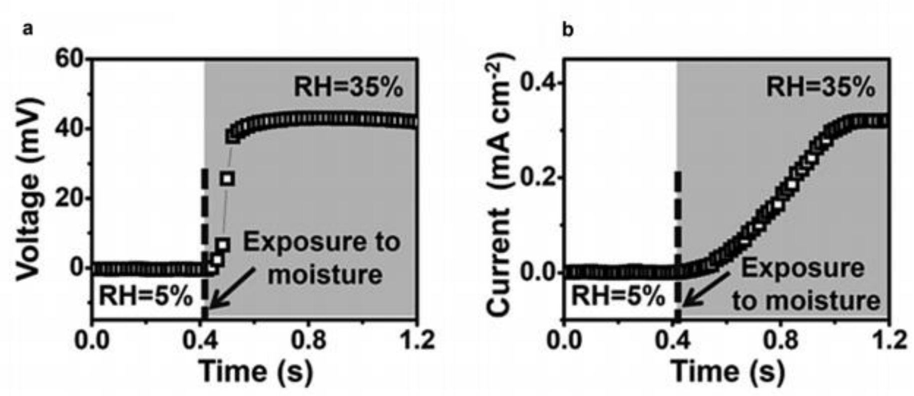

Figure 2.8. Open-circuit voltage (a) and short-circuit current (b) of a graphene oxide nanoribbon MEET device exposed to RH = 5% and RH = 35% [16] (© 2016 John Wiley & Sons).

Nonetheless, it is important and more accurate to report ΔRH numbers and not simply RH because there is no power generation if ΔRH is zero, as the driving force for diffusion of hydrogen ions is non-existent. ΔRH is defined as the difference in relative humidity between the initial environmental conditions to which the MEET device has been exposed for a long time (equilibrium conditions), and the RH of the moisture-laden gas [13]–[16], [19], [60]. **Figure 2.9** shows the output voltage of a MEET device exposed to different levels of relative humidity for a fixed N_2 gas flowrate.

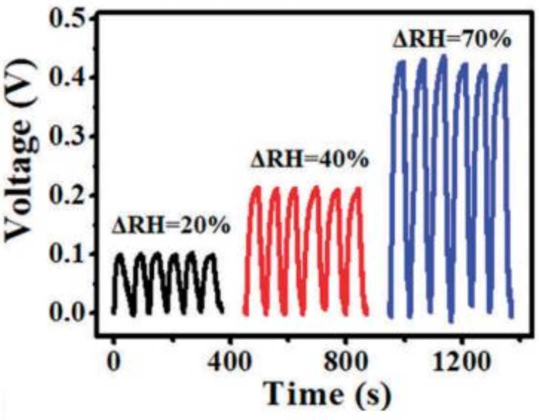

Figure 2.9. The output voltage of a graphene oxide film MEET device exposed to different levels of RH with respect to the initial RH conditions [60] (© 2018 RSC Publishing).

2.1.3 Materials and Configurations

Carbon-based materials are predominately used in the manufacturing of MEET devices. Graphene-based films rich in oxygen-containing functional groups, like hydroxyls and carboxyls, or doped with nucleophilic elements, have been extensively used for harvesting electrical power from moist air and water droplets [13]–[18], [60], [62].

These oxygen-rich graphene-based materials, or graphene oxides, are prepared following different methods in order to establish a gradient of oxygen-rich proton-releasing functional groups. One way to form such a gradient is to apply a bias voltage to two sides of a graphene oxide sheet in a humid environment. This process results in an increase in the oxygen-to-carbon (O/C) ratio at the positive-electrode-contacting side, and a decrease in that same ratio at the negative-electrode-contacting side. This process is called Moisture-Electric Annealing (MeA) and is represented in **Figure 2.10** [13], [14].

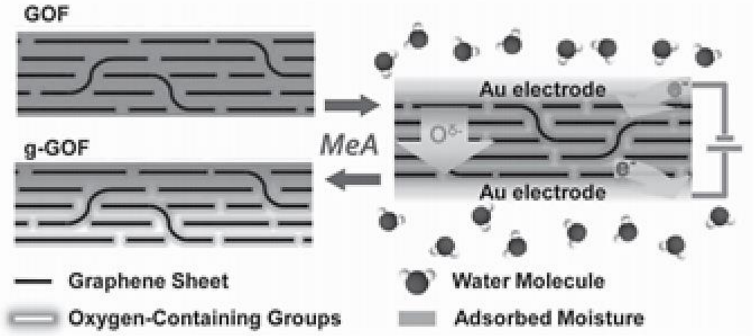

Figure 2.10. MeA process applied to a graphene-oxide film under humid environment [13] (© 2015 John Wiley & Sons).

Another way to establish a hydrogen ion gradient within the film is to fabricate devices that are asymmetric. The graphene oxide film in this case does not contain a gradient of oxygen-rich groups through its thickness. It rather uses a moisture-insulating side (like glass or paper), only allowing water molecules to infiltrate the film from one side as illustrated in **Figure 2.11** [60]**.**

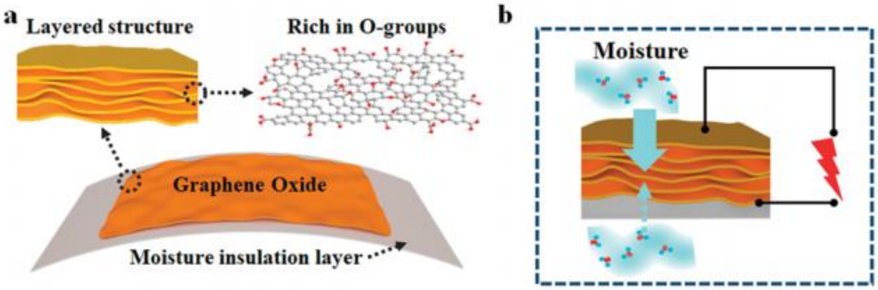

Figure 2.11. (a) MEET device consisting of a graphene-oxide sheet applied to a moisture-impermeable substrate. (b) Schematic of the asymmetrically induced potential of the MEET device upon exposure to moisture [60] (© 2018 RSC Publishing).

Such a configuration ensures that the side exposed to moisture always contains a higher concentration of hydrogen ions, thus allowing the diffusion mechanism to take place from the moisture permeable side to the moisture insulating side [60]. Ion migration causes a net flow of positive charge (current) which translates into a potential difference across the electrodes as shown in **Figure 2.12**.

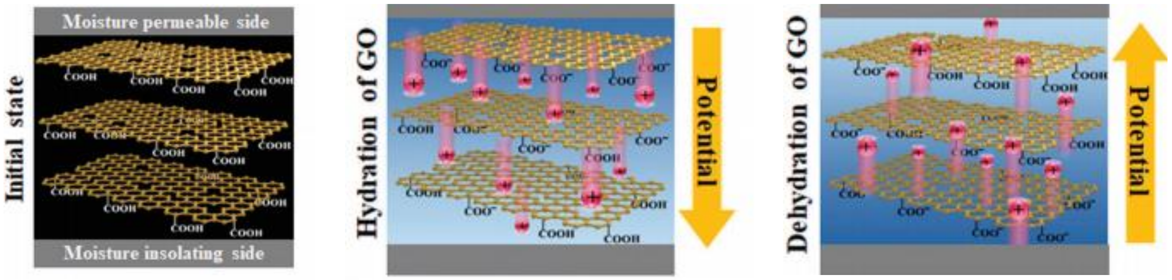

Figure 2.12. Graphene-oxide-based MEET device in its initial state and with asymmetric hydration/dehydration [60] (© 2018 RSC Publishing).

Both the asymmetric and the O/C gradient-based designs are prone to dynamic balance and can therefore only produce a positive potential periodically [13]–[16], [18], [61]. **Figure 2.13** shows the voltage output of an O/C gradient-based MEET device upon exposure to moist air. It is notable that the voltage reaches its peak value at about 22 mV before RH reaches its maximum value of 30%, hence reflecting the dynamic balance that takes place within the graphene oxide film.

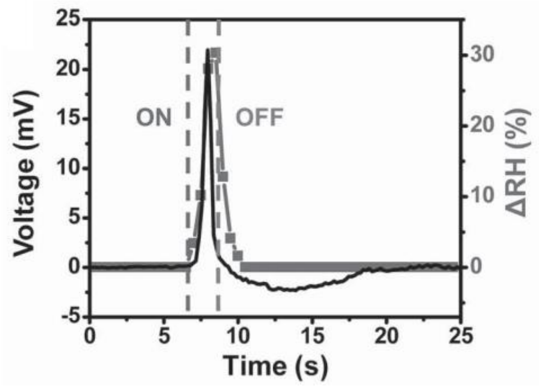

Figure 2.13. Voltage output of an O/C gradient-based MEET device matched with the relative humidity of the impinging gas [13] (© 2015 John Wiley & Sons).

Xue *et al.* produced a MEET device by affixing two electrodes made of multiwalled carbon nanotubes (MWCNT) on a quartz substrate. Carbon black was subsequently collected on the surface of the substrate between the two electrodes over an ethanol flame, followed by annealing and plasma treatment. It was reported that the plasma treatment of the carbon black film changed its affinity for water from hydrophobic to hydrophilic with the contact angle dropping from 143.25° to 10.15°. This phenomenon was explained by the fact that plasma treatment resulted in the formation of oxygen-containing functional groups [61]. **Figure 2.14** shows the Fourier-transform infrared spectroscopy (FTIR) spectra of the pristine and the annealed-plasma-treated carbon black film, as well as their contact angle pre and post-treatment. There is increased photon absorption (low normalized intensity values) at wavenumbers that correspond to oxygen-rich groups, reflecting their presence in numbers after the plasma treatment.

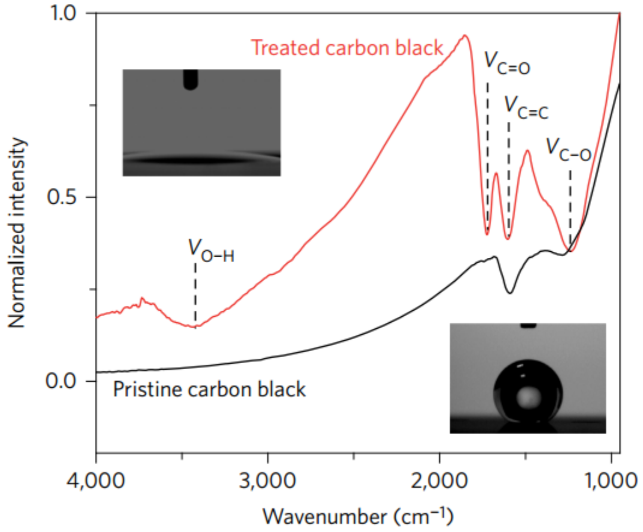

Figure 2.14. FTIR spectra and the contact angle (inset) of the pristine and the annealed-plasma-treated carbon black (black), showing increased photon absorption for oxygen-rich groups in the plasma-treated sample [61] (© 2017 Springer Nature).

Liu *et al.* developed a MEET device by synthesizing a graphene oxide film rich in phosphotungstic acid molecules. A graphene oxide suspension was first prepared following a modified Hummers method, after which it was mixed with ethylenediamine (EN) and heated to 95 °C for 6 hours. This process caused ring-opening reactions between the epoxy groups in the graphene oxide and amino groups of EN. The process was followed by the addition of phosphotungstic acid ($H_3PW_{12}O_{40}\text{-}28H_2O$, HPW): the amino groups previously introduced get protonated in the acid and hence carry a positive charge. On the other hand, the HPW molecules occupy interstitial spaces between the interlayers of the graphene oxide after submersion in the acidic solution [18]. **Figure 2.15** shows an illustration of the synthesis process of an HPW graphene-oxide film.

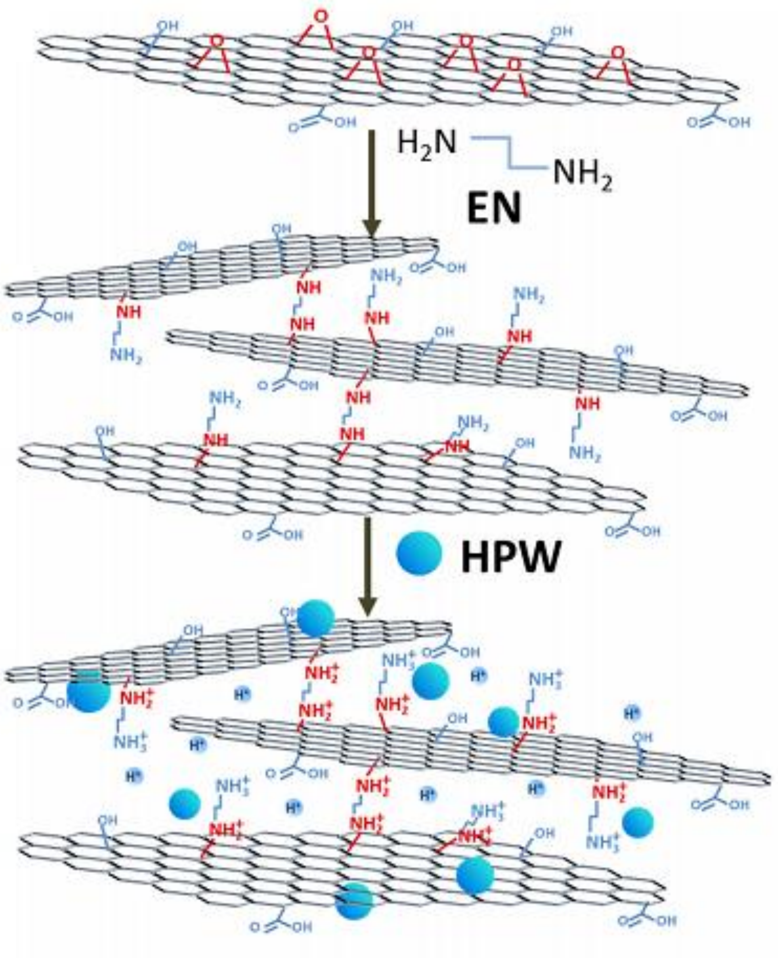

Figure 2.15. Schematic of an HPW-graphene oxide films. EN was attached to the GO through ring-opening reactions and the HPW molecules were inserted between the interlayers after submersion in the acidic solution [18] (© 2018 Springer Nature).

HPW molecules become negatively charged, releasing H^+ ions upon exposure to water. However, in order to extract useful electrical power from these components, an H^+ gradient must be established through the thickness of the film. To do so, the graphene oxide film was dipped in increasingly more concentrated solutions of HPW as illustrated in **Figure 2.16**: the hierarchical soaking (entire film, two-third and one-third) was done in order establish a gradient of proton releasing HPW groups [18].

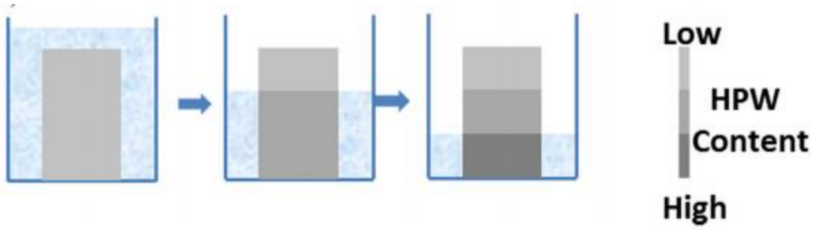

Figure 2.16. Hierarchical soaking of the graphene oxide film in HPW [18] (© 2018 Springer Nature).

Other methods have been investigated to generate electricity from environmental moisture including titanium dioxide (TiO_2) nanowire networks [19] and conductive polymers in which an ionic gradient is implemented via electrolytic-electric annealing (similar to MeA) [63]. The working principles of these design variations also rely on proton diffusion and charge separation, like carbon-based MEET devices. These designs are also prone to saturation and either stop generating power or undergo pole reversal when dynamic balance and later evaporation, take place [19].

2.2 PEEK

2.2.1 Background

The research and development of polyaryl ether ketones (PAEKs) started in the 1960s. In 1978, Imperial Chemical Industries (ICI) filed a patent on thermoplastic aromatic polyetherketones. The patent related to some PAEKS, which have the general formula –Ar–O–, where Ar is is an aryl (aromatic radical). The invention stated that at least some of the aryls must contain a ketone linkage [31]. The principal functional groups of PAEKs are represented in **Figure 2.17.**

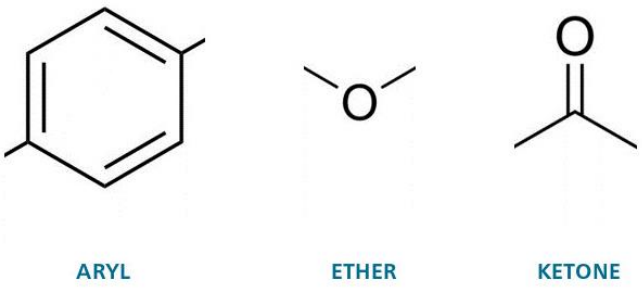

Figure 2.17. The main functional blocks of PAEKs [25] (© 2017 VICTREX® PLC).

These polymers emerged as a solution for the insulation of electric wires subjected to high operation temperatures. The goal of the development of PEEK was to fulfill high melting point, excellent mechanical and electrical insulating properties as well as high toughness requirements at high operating temperatures. VICTREX® was the first company to commercialize the polymer in 1981 [25], [29], [31].

2.2.2 Structure and Mechanical Properties

PEEK, or poly(oxy-1,4-phenyleneoxy-1,4-phenylenecarbonyl-1,4-phenylene), is a semi-crystalline thermoplastic polymer, part of the polyaryl ether ketone family. It is composed of ketone and ether linkages on either side of aryl moieties [25], [27], [29]. The PEEK molecule is presented in **Figure 2.18**: this building block is repeated on average between 200 to 300 times, forming a single PEEK chain [25].

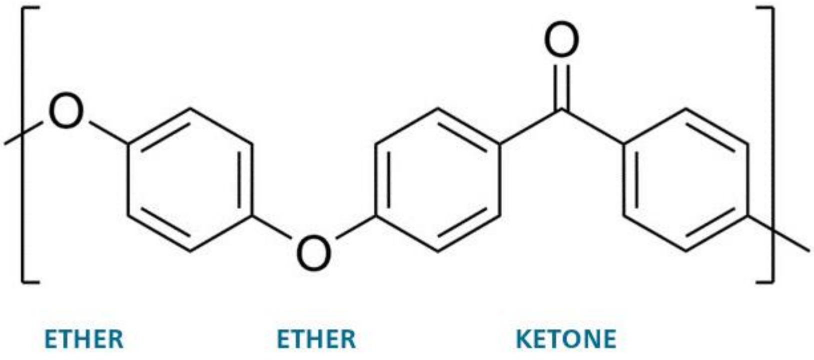

Figure 2.18. PEEK molecule [25] (© 2017 VICTREX® PLC).

The natural grade of PEEK is semi-crystalline and has a density in the range of 1.26 – 1.32 g/cm^3, depending on the percentage of crystallinity [26], [64], [65]. The natural degree of crystallinity of PEEK is typically in the range of 30 – 35%, showing little variance over a wide range of cooling rates. Notwithstanding, crystallinity values from 0 to 40% can be obtained with more extreme thermal histories: rapid quenching (above 700°C/min) results in amorphous structures, whereas slower cooling rates and annealing produce more crystalline structures [29], [66].

Shorter chains have lower molecular weights and tend to crystallize faster. On the other hand, longer chains have a higher molecular weight and tend to result in more amorphous structures [66], [67]. VICTREX® PEEK grade naming represents the molecular weight of the chains, with PEEK 90G having a lower molecular weight than 150G and 450G respectively. Interestingly, the molecular weight is roughly proportional to the viscosity of the polymer at moderate shear rates [66]. **Table 2.1** presents the mechanical properties of three different grades of PEEK.

Table 2.1. Some mechanical properties of different grades of PEEK [66].

	PEEK 90 G	PEEK 150 G	PEEK 450 G
Tensile Strength (MPa)	110	110	100
Tensile elongation (%)	15	25	45
Flexural modulus (GPa)	4.3	4.3	4.1

Pure PEEK exhibits very good mechanical properties for a thermoplastic polymer [66], [67]. However, the retention of the mechanical properties at high temperatures and in hostile environments is what makes PEEK an interesting alternative to other plastics [66]. Typical mechanical properties are presented in **Table 2.2**.

Table 2.2. Mechanical properties of PEEK at different temperatures [29], [64], [66].

Mechanical data	Temperature	Units	Typical values
Tensile strength	23 °C	MPa	92 – 105
	100 °C		50
	200 °C		12
	300 °C		10
Tensile elongation at break	23 °C	%	30 – 50
Young’s Modulus in Tension	23 °C	GPa	4.1
Flexural strength	23°C	MPa	175
	125°C		90
	175°C		20
	275°C		13.5
Flexural modulus	23 °C	GPa	3.7 – 4.3
	100 °C		3.6
	200 °C		0.5
	300 °C		0.3

Reinforcements are commonly added to PEEK matrices to enhance the overall mechanical properties as shown in **Table 2.3** [66]–[70].

Table 2.3. Comparison of some typical mechanical properties of PEEK with PEEK composites [66], [68].

	PEEK	PEEK 30% glass fibre	PEEK 40% carbon fiber
Tensile strength (MPa)	100	180	250
Tensile elongation at break (%)	45	2.7	1.6
Flexural modulus (GPa)	4.1	11.3	28
Density (g/cm^3)	1.32	1.51	1.44

The addition of reinforcement to PEEK matrices results in an increase in the tensile strength, the flexural and Young's modulus. The tensile elongation at break decreases with an increase in the filler's content [66]–[70].

2.2.3 Thermal Properties

PEEK's thermal properties are of the utmost importance given the sensitivity of the mechanical properties of polymers to temperature changes [26], [64], [65], [71] as previously shown in **Table 2.2**. PEEK's glass transition temperature (T_g) is 143 °C (onset) and melting point (T_m) is 343 °C [64]–[66], [68]. The addition of fillers to PEEK has no influence on the T_g and T_m of the polymer [68], [70].

The linear coefficient of thermal expansion (LCTE) is an important variable to account for when dissimilar materials are combined. The LCTE of semi-crystalline PEEK ranges from 47 $\times 10^{-6}$ °C^{-1} below T_g to 140 $\times 10^{-6}$ °C^{-1} above T_g. It is important to point out that the LCTE of bulk semi-crystalline and amorphous PEEK are different, and that they are both temperature dependent [26], [29], [64], [68]. **Figure 2.19** shows the variation of the LCTE as a function of temperature for semi-crystalline PEEK.

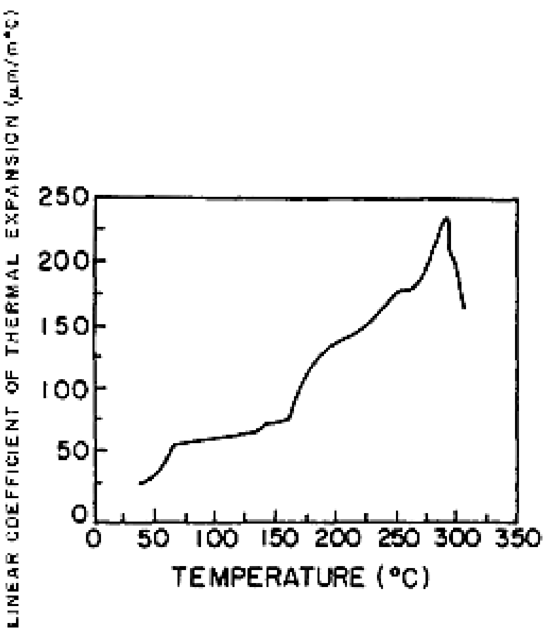

Figure 2.19. LCTE vs. temperature of semi-crystalline PEEK [26] (© 1996 Elsevier) .

Goyal *et al.* studied the LCTE of a composite of PEEK and alumina. The composite was obtained by mixing different %wt. of Al_2O_3 with PEEK powder in ethanol from which a slurry was produced. The slurry was subsequently dried in a vacuum. The experimental LCTE of virgin PEEK was found to be 58×10^{-6} °C^{-1} and the reported LCTE of alumina was 6.6×10^{-6} °C^{-1}. It was concluded that the addition of both micro and nano-sized alumina particles to PEEK resulted in a decrease in its LCTE. For the same target LCTE, a lower amount of nano-sized alumina (in %wt.) is needed in comparison to micro-sized alumina [72]. **Figure 2.20** shows the effect of the addition of both micro-sized and nanosized alumina particles on the LCTE of PEEK/alumina composite.

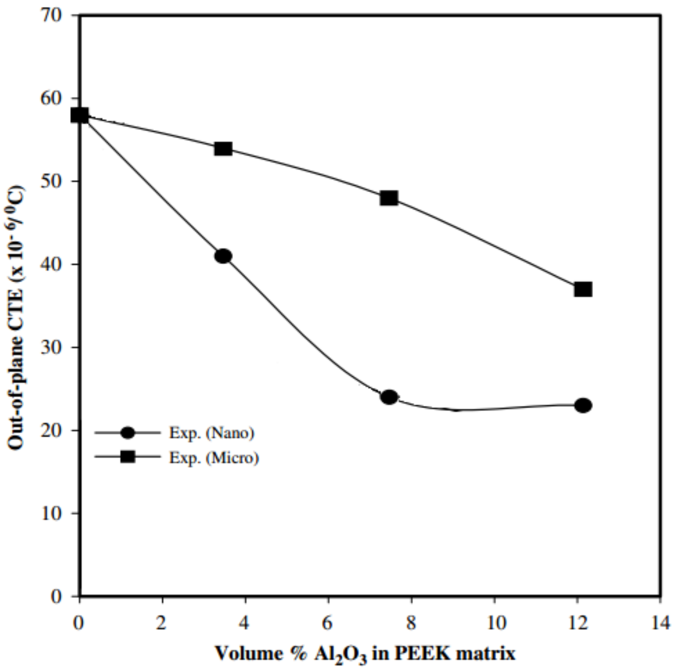

Figure 2.20. Experimental LCTE of PEEK/alumina composite as a function of alumina content for micro-sized and nano-sized alumina particles [72] (© 2008 IOP Publishing).

2.2.4 Resistance and Degradation

2.2.4.1 Chemical Resistance

PEEK's chemical resistance is an important criterion in its selection as a design material. It is resistant to numerous types of acids, alcohols, aldehydes, ketones, bases, hydrocarbons, oils and other inorganic solutions up to 200°C. More importantly, PEEK's resistance to degradation in tap water, distilled water as well as sea water is excellent [29], [66], [68], [73].

2.2.4.2 Thermal Degradation

The melting point of PEEK is 343 °C but its thermal degradation, or weight loss, only occurs in the vicinity of 500 °C [30], [71]. In fact, pure PEEK's degradation temperature at 1% weight loss is 565 °C in N_2 and 531 °C in air. Glass fiber (30 %wt.) reinforced PEEK (PEEK-GL30) has a degradation temperature at 1% weight loss of 562 °C in N_2 and 526 °C in air, and finally carbon fiber (30 %wt.) reinforced PEEK (PEEK-CA30) has a degradation temperature at 1% weight loss of 554°C in N_2 and 531°C in air [30]. **Figure 2.21** shows the weight percentage of PEEK and its composites when exposed to high temperatures in nitrogen gas.

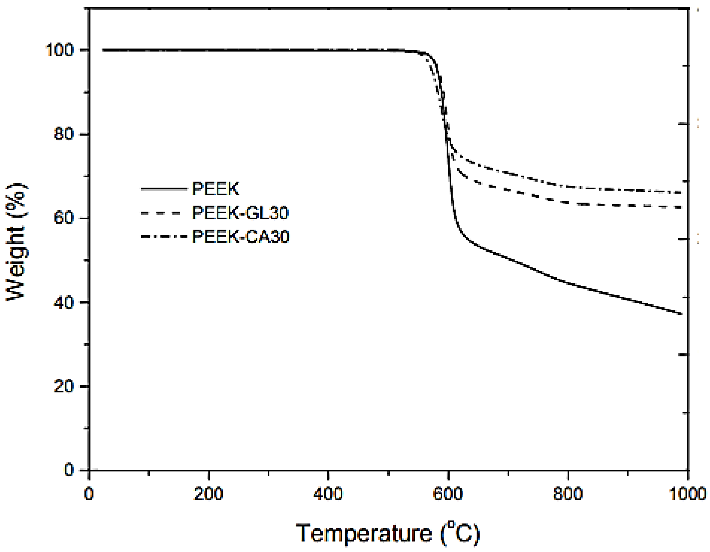

Figure 2.21. Thermal decomposition of PEEK and its composites in N_2 [30] (© 2003 Huiqing Zhang).

2.2.5 Electrical Properties and Fuel Cell Applications

PEEK is a good electrical insulator in a wide range of environments and temperatures. In fact, it was developed to insulate electric wires [31], [68]. Nevertheless, it has been shown that crystallinity reduces conductivity (or increases resistivity) in polymers, especially at higher temperatures [65], [74]. This is also true for PEEK as seen in **Figure 2.22**.

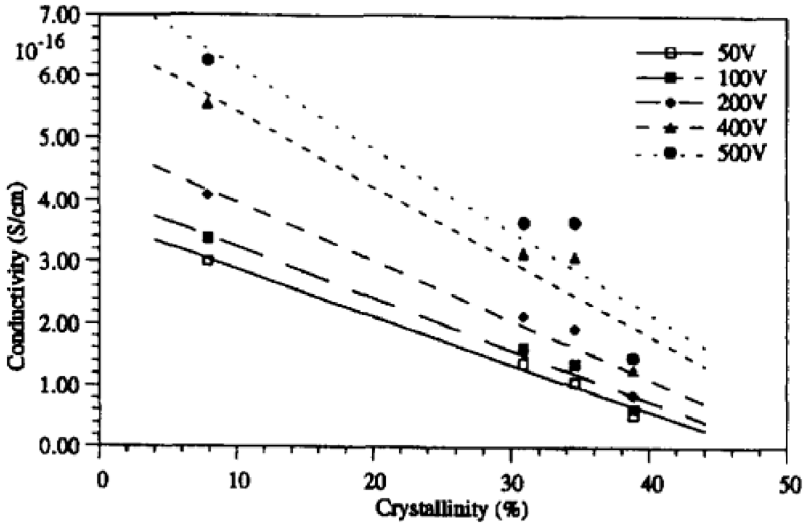

Figure 2.22. Conductivity vs. crystallinity for a 25µm PEEK film at different voltages [65] (© 1994 IEEE).

Resistivity ρ is expressed in ohm-meters (Ω.m) and is inversely proportional to conductivity:

$$\rho = \frac{1}{\sigma} \tag{2.1}$$

σ is conductivity and has siemens per metre units (S/m). One siemens (S) is simply defined as:

$$S = \Omega^{-1} \tag{2.2}$$

Interestingly, and despite being an insulator of electrons, PEEK is used as a proton exchange membrane in fuel cells (PEMFC) [75]–[81].

Fuel cells operate following the reverse process of electrolysis. They are electrical cells that generate an output of electrical power by converting hydrogen or hydrogen-containing fuels and oxygen into water. In hydrogen fuelled PEMFC, hydrogen is catalytically oxidized at the anode to produce protons that are transferred via a membrane to the cathode. At the cathode, the hydrogen ions react with the oxygen gas producing water and releasing energy [81]. The process is illustrated in **Figure 2.23**.

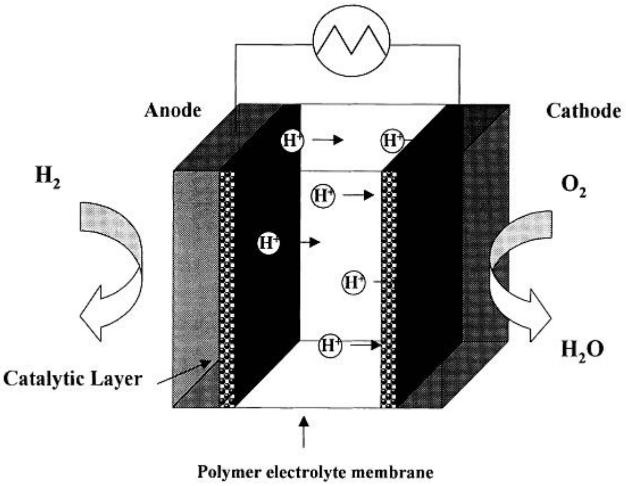

Figure 2.23. Schematic of a polymer electrolyte fuel cell [82] (© 2000 Elsevier).

The chemical reactions are given by **equations (2.3) – (2.5)** [82].

At the anode:

$$2H_2 \rightarrow 4H^+ + 4e^- \tag{2.3}$$

At the cathode:

$$O_2 + 4H^+ + 4e^- \rightarrow 2H_2O \tag{2.4}$$

The overall reaction is:

$$2H_2 + O_2 \rightarrow 2H_2O + \text{Heat} + \text{Electrical Energy} \tag{2.5}$$

PEEK is mainly used in its sulfonated form (SPEEK) as a membrane material in PEMFC. Despite Nafion™ being the most popular choice for the manufacturing of PEMFC membranes, PEEK has been suggested as a replacement because Nafion™ is prone to fuel crossover (leakage) from the anode to the cathode. Furthermore, Nafion™ performance drops at temperatures above 80°C [75]–[81].

2.2.6 Water Sorption Properties

2.2.6.1 Fickian Diffusion

Fickian diffusion describes the movement of a species (atoms, molecules or ions) through a solid medium: matter migrates from the high concentration to the low concentration side, following the laws of diffusion [83], [84]. **Figure 2.24** shows an illustration of the Fickian diffusion concept.

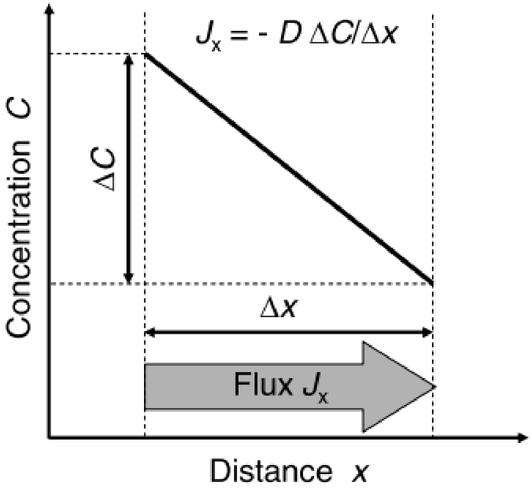

Figure 2.24. Illustration of Fickian diffusion in one dimension [83] (© 2007 Springer Nature).

Fick's first law, in one dimension and for isotropic materials is given by [83]:

$$J_x = -D \frac{\partial C}{\partial x} \tag{2.6}$$

Where J_x is the flux in the x-direction in mol/(s.m^2), D is the diffusion coefficient (or diffusivity) in m^2/s and C is the concentration in mol/m^3. A more generalized Fick's first law for isotropic materials is given by [83]:

$$\mathbf{J} = -D\boldsymbol{\nabla}\mathbf{C} \tag{2.7}$$

Where $\mathbf{J}$ is a vector of the diffusion flux and $\mathbf{\nabla C}$ is the concentration gradient vector ($\frac{dC}{dx}\hat{\imath} + \frac{dC}{dy}\hat{\jmath} + \frac{dC}{dz}\hat{k}$). It is worth noting that $\mathbf{\nabla C}$ always points in the direction where the concentration field is subjected to the fastest increase [83].

In the case of anisotropic materials, the generalization of Fick's first law for anisotropic materials becomes [83]:

$$\mathbf{J} = -\mathbf{D\nabla C} \tag{2.8}$$

In this case, diffusivity **D** is direction dependent and is expressed by a second-order tensor in the three orthogonal principal axes [83]:

$$\mathbf{D} = \begin{pmatrix} D_1 & 0 & 0 \\ 0 & D_2 & 0 \\ 0 & 0 & D_3 \end{pmatrix}$$

where D_1, D_2 and D_3 are called the principal diffusion coefficient or principal diffusivities. Consequently, the diffusion fluxes in each principal axis are given by [83]:

$$J_1 = -D_1 \frac{\partial C}{\partial x} \tag{2.9}$$

$$J_2 = -D_2 \frac{\partial C}{\partial y} \tag{2.10}$$

$$J_3 = -D_3 \frac{\partial C}{\partial z} \tag{2.11}$$

Fick's second law is the result of the combination of the first law (**equation (2.7)**) and continuity. It is given by [83]:

$$\frac{\partial C}{\partial t} = \mathbf{\nabla}.(D\mathbf{\nabla C}) \tag{2.12}$$

where t is time and D is the diffusivity in an isotropic medium (scalar). $\nabla.$ is the divergence operator.

2.2.6.2 Fickian and Non-Fickian Diffusion in Polymers

Rubbery polymers tend to generally experience Fickian diffusion, where any change in their condition (movement of polymer chains or change of density) results in a new equilibrium volume rapidly (instant relaxation). On the other hand, glassy polymers follow non-Fickian diffusion because there is a delay between the onset and the end of the transition in their properties. In other words, glassy polymers have time-dependent behaviours: deviations from the Fickian model are attributed to the finite rates at which the polymer structure evolves as a result of the sorption of penetrants [84].

Glassy polymers are subjected to relaxation mechanisms below T_g. In the presence of water, polymers that contain polar groups form hydrogen bonds with the water molecules, resulting in changes in the dielectric properties of the material. These changes in the dielectric constant reflect loss mechanisms that are due to molecule rotation and movement (relaxation) [84], [85]. In fact, glassy polymers are thermodynamically unstable and tend to minimize their energy over time, causing a change in their properties such as increased modulus, decreased permeability and increased brittleness. The addition of water makes these changes easier and hence, more noticeable [86].

The relaxation times of polymers tend to decrease as the penetrant's concentration or the temperature is increased and thus, the motion of the polymer chains is enhanced. As such, a proposed classification based on the relative rates of diffusion and relaxation has been made [84]:

1. **Case I Fickian diffusion:** the rate of diffusion is significantly less than the rate of relaxation.
2. **Case II diffusion:** the rate of diffusion is very rapid compared to the relaxation process.
3. **Non-Fickian diffusion:** the rate of diffusion and relaxation are comparable, giving rise to complex sorption behaviours.

Case I and II are simple inasmuch as they can be described by a single parameter, respectively the diffusion coefficient and the constant velocity of the advancing front of the moving penetrant. The non-Fickian diffusion mechanism on the other hand requires two or more parameters to express the effects of the interacting relaxation and diffusion mechanisms [84].

Figure 2.25 shows the moisture content of two materials that obey Fickian and non-Fickian diffusion mechanisms as a function of time.

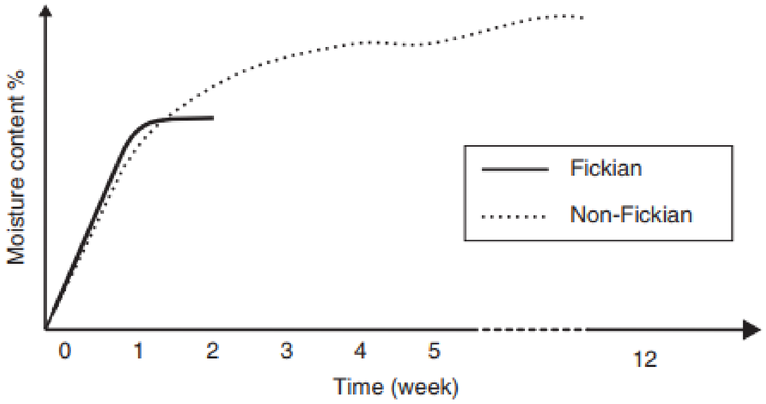

Figure 2.25. Fickian and non-Fickian diffusion behaviours in polymeric materials [87] (© 2019 Elsevier).

2.2.6.3 Diffusion in Polymer/Ceramic Composites

It is believed that two parallel diffusion processes occur in polymer composites: diffusion through the polymer matrix, and diffusion through a network of micro-channels named “mesoscopic free volume”, taking place between the polymer matrix and the filler particles, but also in voids between the polymer chains [87]–[89].

The crystalline regions of materials are inaccessible to most solvents, and most of the absorption takes place in amorphous regions and voids [90]. It is therefore reasonable to attribute the faster absorption kinetics for composites (compared to pure polymers) to the voids at the interface between the matrix and the filler [89].

Once the interfacial voids have been filled with water, the diffusion mechanism is slowed down as it is limited by the kinetics of diffusion in the polymer matrix: water molecules infiltrate the amorphous regions and the free volume between them, which was shown to be a slow process [22], [23], [87], [89].

Water absorption in voids (micro and macro) is believed to follow a Fickian diffusion behaviour, whereas water molecules that infiltrate the free volume between chains (in the amorphous regions) are thought to follow a non-Fickian diffusion mechanism. This is attributed to the fact that non-Fickian diffusion results from the formation of hydrogen bonds between the water molecules and the polar groups of the polymer. These hydrogen bonds push the polymer chain apart, resulting in the expansion of the free space and subsequently, more water uptake [87].

The water absorption kinetics of polymer composites are shown in **Figure 2.26**.

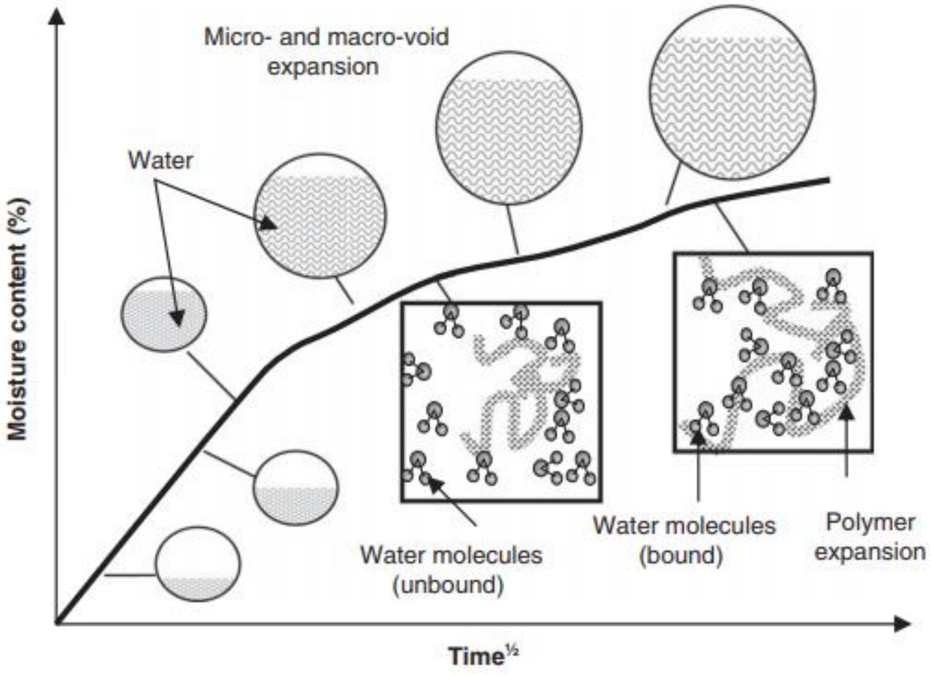

Figure 2.26. Suggested effect of water absorption on the micro and macro voids in the polymer (non-Fickian diffusion) [87] (© 2019 Elsevier).

2.2.6.4 Diffusion in PEEK

PEEK’s ketone group is polar and can therefore interact with water molecules via hydrogen bonds as well as react with water to form hydrates. Despite the reaction favouring the reactants rather than the products (equilibrium constant <0.001), it results in the formation of hydroxyl groups that are crucial in the operation of MEET devices [91] as shown in **Figure 2.27**.

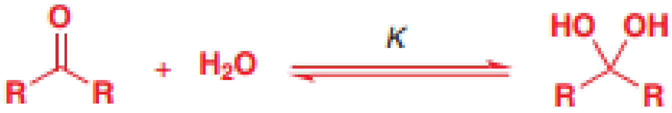

Figure 2.27. The hydration reaction of ketones, with *K* being the equilibrium constant [91] (© 2012 Oxford University Press).

Grayson *et al.* showed that water solubility in semi-crystalline PEEK increases from 0.44 %wt. at 35°C to 0.55 %wt. at 95°C. It was also shown that faster water uptake takes place at higher temperatures. The diffusion process for sorption, desorption and resorption at 35°C, 50°C, 65°C, 80°C and 95°C were reported to be the same and shown to follow a classical Case I Fickian diffusion process [22].

Figure 2.28 shows the sorption of water in two 2 and 6 mm thick PEEK sheets at different temperatures, function of the square root of time.

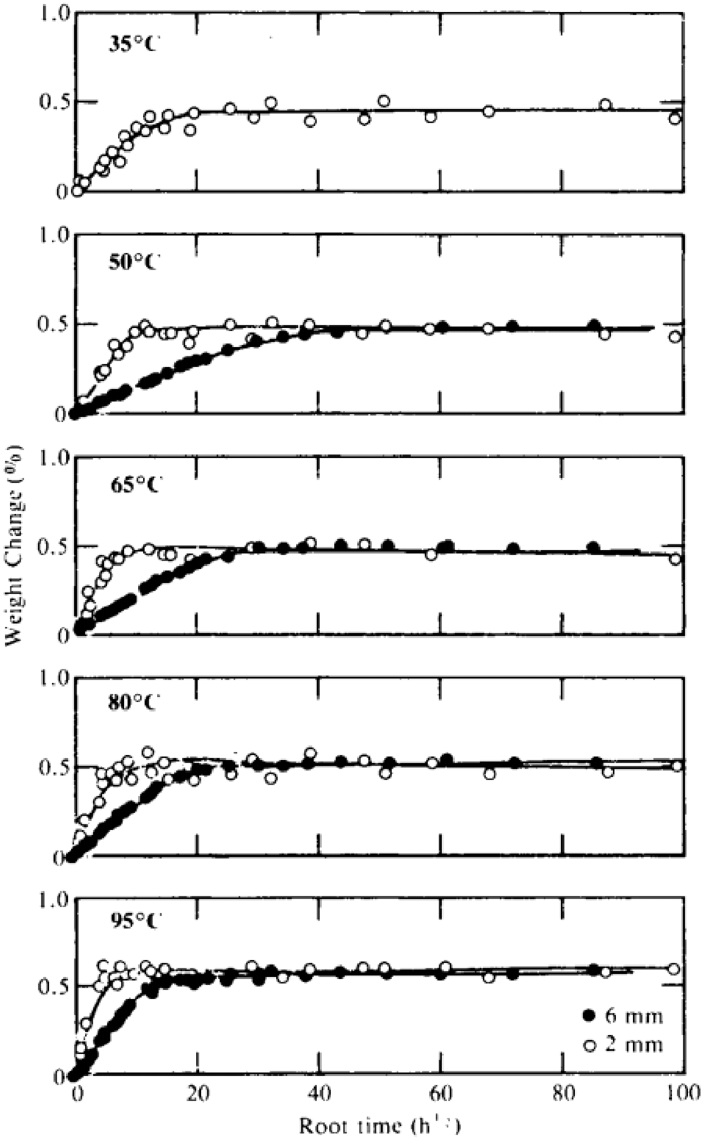

Figure 2.28. Sorption of liquid water in a 2-mm and 6-mm thick semicrystalline PEEK samples at 35°, 50°C, 65°C, 80°C and 95°C as a function of the square root of exposure time. The solid lines represent the Fickian model [22] (© 2003 John Wiley & Sons) .

It is clear that thinner films approach saturation earlier than thicker films. Moreover, it is noticeable that an increase in temperature results in a larger rate of weight change during the first hours of exposure to water. Times to saturation are over hundreds of hours for the different temperatures [22].

Interestingly, it was found that water sorption in PEEK at temperatures between 50°C and 95°C did not cause a change in PEEK's density. In other words, the ratio of the combined mass of PEEK and the sorbed water to the expanded volume of the PEEK film remained constant. It was suggested that a fraction of the water entered the voids in the PEEK film (about one third) and did not cause a volume change, whereas the remaining two thirds of the water gave rise to changes in the dimensions of the film [22].

Mensitieri *et al.* studied the water sorption properties of semicrystalline PEEK at 5°C, 20°C, 40°C and 60°C (below T_g) as well as an amorphous PEEK film at 60°C . It was concluded that liquid water sorption in semicrystalline and amorphous PEEK followed the classical case I Fickian mechanism. At higher water activity (water vapor) however, it was determined that the amorphous film underwent a diffusion mechanism that consisted of the linear superposition of a Fickian diffusion process and a first-order relaxation term [23]. Similarly to what Grayson *et al.* reported [22], higher temperatures occasioned faster water uptake, resulting in earlier saturation.

At 20°C, the ratio of the mass of sorbed liquid water at time (t) (M(t)) over the total mass of water sorbed by the PEEK film at saturation (M_∞) approaches unity after $t^{1/2}/l \approx 8000$ s. l is the thickness of the film in centimetres and evaluated at 0.2 cm in this study. Therefore, $M/M_\infty \approx 1$ when $t \approx 711$ hours or roughly 29 days. The value of M_∞ did not considerably vary with temperature and was reported to be around 0.48% [23]. **Figure 2.29** shows the water sorption behaviour of a 2 mm thick semicrystalline (30%) PEEK sheet at different temperatures.

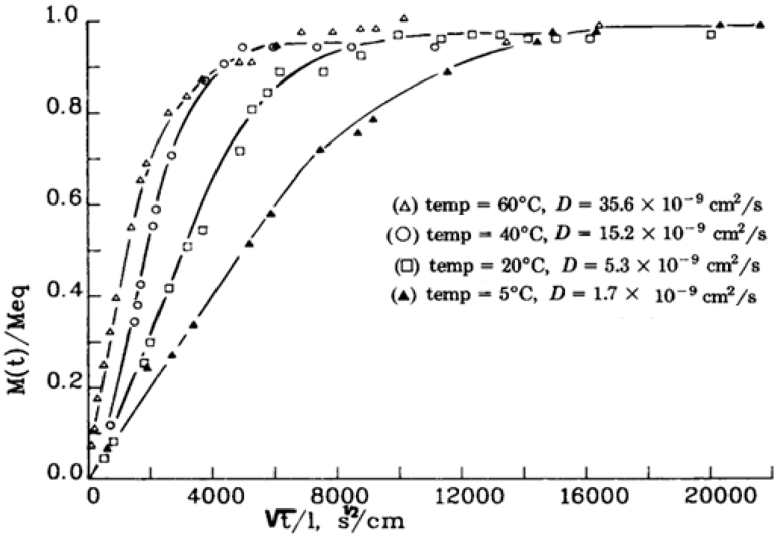

Figure 2.29. Ratio of liquid water sorption to maximum water content at saturation for a 2 mm thick semicrystalline (30%) PEEK sheet. The solid lines represent the Fickian model having *D* as a diffusion coefficient [23] (© 2003 John Wiley & Sons).

Buchman *et al.* studied the water sorption properties of APC (a composite consisting of continuous carbon fibers embedded in a PEEK matrix). The PEEK content was measured to be about 30%. After submersion in water at 71°C, samples were reported to attain equilibrium at around 26-35 days. Nevertheless, as shown in **Figure 2.30**, there is no clear asymptote indicating saturation for the PEEK composite. The sorption process is sharp at the beginning and its slope decreases with time [24]. This behaviour resembles the non-Fickian diffusion observed in polymer composites shown in **Figure 2.26**.

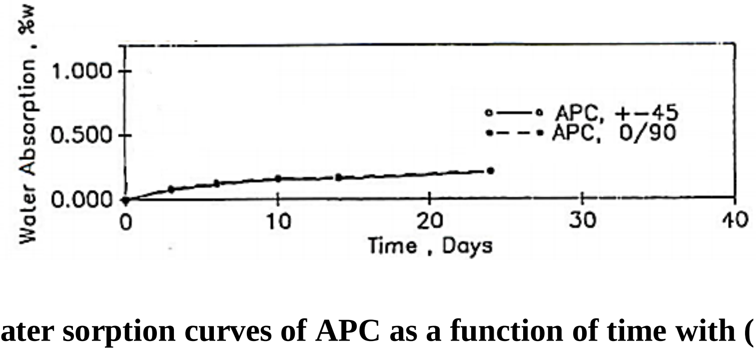

Figure 2.30. Water sorption curves of APC as a function of time with (+-45) and (0/90) representing the carbon fiber orientation in the PEEK matrix [24] (© 1991 Alisa Buchman).

Water sorption for 32 %wt. PEEK carbon fiber was estimated to be around 0.2 wt.% at the end of the experiment and appeared to be independent of fiber orientation [24].

2.3 Aluminum in Electrical Components

Aluminum is the fourth most conductive metal after silver, copper and gold respectively, but its cost per unit mass is the lowest out of the most conductive metals [67], [92]. It typically displays electrical conductivity values above 3.0×10^7 $\Omega.m^{-1}$ [67] and on an equivalent weight basis, its electrical conductivity is approximately twice that of copper [93].

Different aluminum alloys exist to suit different needs. Depending on their strengthening mechanism, which can be work hardening or precipitation hardening, their mechanical properties, their susceptibility to corrosion and their manufacturability vary [93], [94]. **Table 2.4** shows the various aluminum series classifications according to their alloying elements.

Table 2.4. Classification of wrought aluminum alloys according to their strengthening mechanism [93].

Alloy system	Aluminum series
Work-hardenable alloys	
Pure Al	1xxx
Al-Mn	3xxx
Al-Si	4xxx
Al-Mg	5xxx
Al-Fe	8xxx
Al-Fe-Ni	8xxx
Precipitation-hardenable alloys	
Al-Cu	2xxx
Al-Cu-Mg	2xxx
Al-Cu-Li	2xxx
Al-Mg-Si	6xxx
Al-Zn	7xxx
Al-Zn-Mg	7xxx
Al-Zn-Mg-Cu	7xxx
Al-Li-Cu-Mg	8xxx

Despite being mainly used in construction, transportation and packaging, around 13% of the global use of aluminum in 2015 was directed towards the production of electrical and electronic components: it is a popular choice in the manufacturing of passive electrical components like capacitors, but also in motors and in power lines [92]–[95]. Furthermore, aluminum has been used in the manufacturing of MEET devices [17]–[19].

The 6xxx wrought alloys are precipitation-hardenable aluminum alloy series that have moderately high strength and very good resistance to corrosion. They use magnesium and silicon as principal alloying elements and are used for structural, marine, building, machinery and process-equipment applications. Aluminum 6061 specifically is a general purpose alloy: its wide availability on the market and its relatively low cost make it a suitable choice for the initial design of MEET devices [93], [94].

2.4 Cold Gas Dynamic Spray (CGDS)

CGDS is a solid-state deposition process, part of the thermal spray family. It relies solely on the kinetic energy of impinging feedstock particles to form coatings, as opposed to thermal energy, therefore suppressing the need to melt the feedstock material. In order to accelerate the particles of the feedstock material, the material in its powder form is injected into a heated inert gas stream that is accelerated through a converging-diverging (de Laval) nozzle. The particles that reach adequately high velocities prior to impact on the substrate deform plastically upon impact and bond with the substrate [96]–[100].

The stagnation pressure and temperature of the compressed gas, also called the working gas, are controlled by a pressure regulator and a gas heater respectively. After going through the gas heater, the working gas is accelerated in a de Laval nozzle to supersonic velocities (up to 1200 m/s). This same compressed gas is injected into a powder feeder to drive the particles of the feedstock powder into the nozzle: they can be injected upstream (before the throat) or downstream (after the throat) to be accelerated by the gas flow as shown in **Figure 2.31**. An optional powder heater can be used to preheat the feedstock powder before its injection into the nozzle [96]–[98].

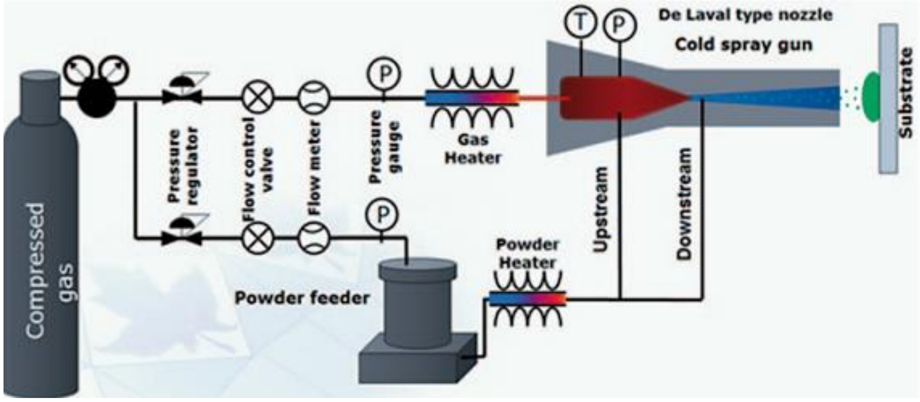

Figure 2.31. Schematic illustrating the CGDS process for upstream (high pressure) and downstream (low pressure) powder injection [98] (© 2015 Springer Nature).

2.4.1 Background

CGDS was developed in the mid-1980s at the Institute of Theoretical and Applied Mechanics of the Siberian Division of the Russian Academy of Science in Novosibirsk. The process was accidentally discovered when professor Papyrin and his colleagues were studying models subjected to a supersonic two-phase flow composed of gas and solid particles in a wind tunnel. The main aim of the wind tunnel experiments was to study the influence of solid particles on flow structure and their interaction with bodies. In order to visualize this interaction, particles of different sizes and materials were injected into the gas flow. It was observed that trace particles were deposited on the leading edge of the bodies under certain conditions [96]. The two-phase flow visualization is presented in **Figure 2.32**. Subsequently, the process was further developed by adding gas heating, powder injection systems and improving nozzle designs in order to enhance the quality of the deposits, which were improved to become coatings [96], [97]. A patent for the process was filed in 1990 and granted in 1994 [97].

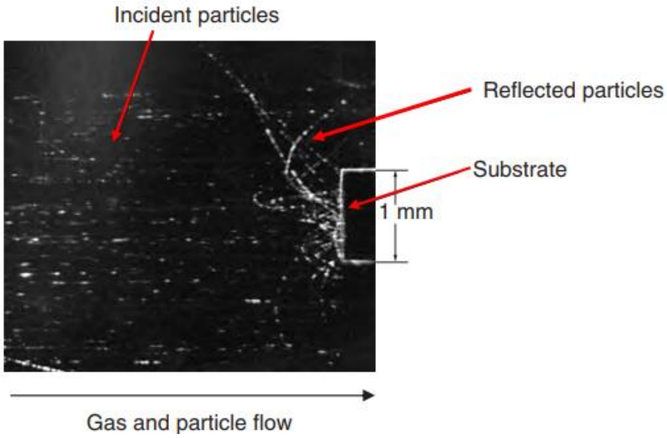

Figure 2.32. Two-phase flow visualization using scattered light showing the particle trajectories when impinging onto a substrate in a wind tunnel [96] (© 2007 Elsevier) .

2.4.2 Adhesion Mechanism

Adhesion in CGDS can be achieved by creating mechanical or metallic bonds between the particle and substrate, or between the particle and previously deposited particles [101], [102].

For bonding to occur, the feedstock particles must be accelerated to velocities that are over a minimum threshold, named the critical velocity, to ensure that sufficient deformation of the particle and/or the substrate takes place [96], [103], [104]. An example of mechanical anchoring is presented in **Figure 2.33.**

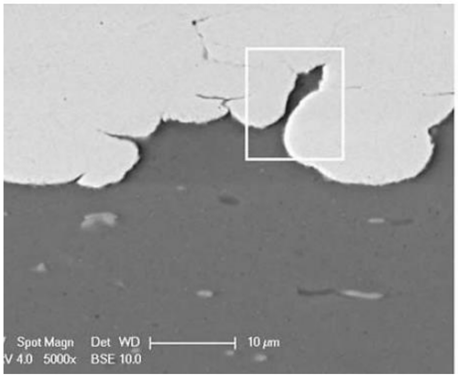

Figure 2.33. Mechanical interlocking between copper particles (light color) and an aluminum substrate (darker color) [101] (© 2009 Springer Nature).

Mechanical anchoring can be improved by increasing the substrate roughness by means of grit blasting, pulsed waterjet or other surface preparation methods for certain particle/substrate material combinations. This results in the cleaning of the surface and the creation of asperities that could promote particle anchoring onto the substrate [101], [105], [106].

Nevertheless, increasing the substrate's surface roughness can be detrimental to adhesion to some particle/substrate material combinations as the likelihood of developing metallic bonds between the particle and the substrate decreases with increasing surface roughness. Metallic bonds are intrinsically stronger than mechanical interlocking and reducing the former results in overall lower adhesion strength. For pure mechanical adhesion however, increasing surface roughness results in higher bond strengths [101], [102]. Nastic *et al.* showed that grit embedment for pure mechanical bonding does not affect bond strength [102].

Metallic bonding takes place when intimate contact occurs between the clean metallic surfaces of the particle and the substrate, or between an impinging and a deposited particle [104]. **Figure 2.34** illustrates metallic bonding sites between particles of Ti-6Al-4V sprayed on a mild steel substrate.

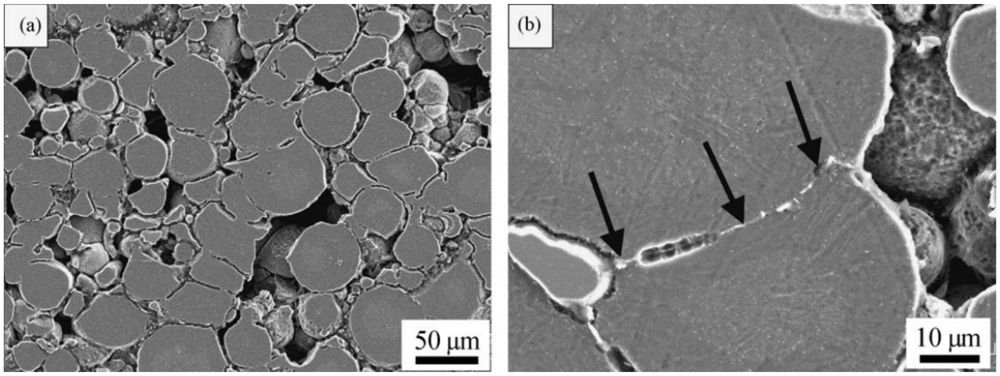

Figure 2.34. Cross-sectional SEM pictures of a Ti-6Al-4V coating sprayed on a mild steel substrates in its etched state (a,b), with (b) containing arrows pointing to local metallurgical bonding sites between deposited particles [107] (© 2007 Elsevier) .

Simulations showed that material deformation in CGDS can reach strain rates of up to 10^9 s^{-1} and strains of 10 in the bonding area [108]. Thus, upon impact, extremely localized heat generation, confined to a thin region adjacent to the particle/substrate or particle/particle interface, occurs because of the high plastic strain energy and the short time scales inherent to the CGDS process (in the order of 50 ns). The generated heat does not have sufficient time to dissipate in the material, and consequently, a localized increase in temperature takes places, resulting in the localized softening of the material and the mitigation of the work hardening effects. Reduction in the flow stress ensues and the material flows outwards forming jets. This phenomenon is known as adiabatic shear instability [103], [104], [109]. Jet formation is credited with breaking up surface oxides, allowing intimate contact between the two metals [103]. **Figure 2.35** shows peripheral jetting of a copper particle deposited on a copper substrate.

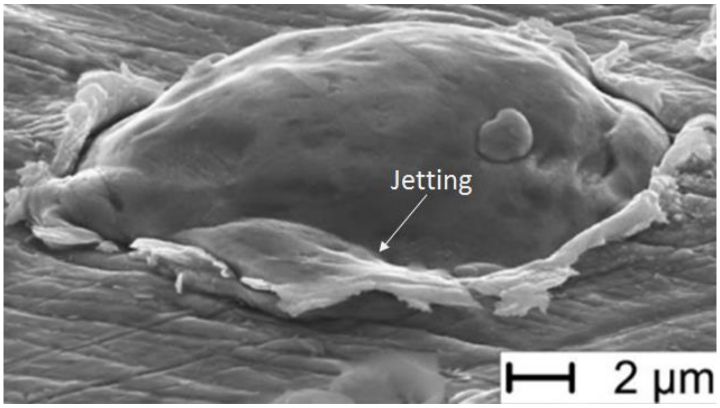

Figure 2.35. SEM picture (secondary electron mode) of a copper particle on a copper substrate. Jetting of the material is observed [104] (© 2003 Elsevier).

In order to assess the quality of the bonds established between the particles and the substrate, or between the particles in the coating, adhesion tests are usually conducted [110]–[112]. The ASTM C633 standard specifies the testing method, where tensile stresses are applied to a coated sample (bond cap/substrate) glued to another cylindrical sample (mating cap) as illustrated in **Figure 2.36.** The force vs. displacement data obtained from the tensile test is recorded and the ultimate tensile stress of the coating is computed by dividing the force at the breaking point over the area of the cylindrical sample.

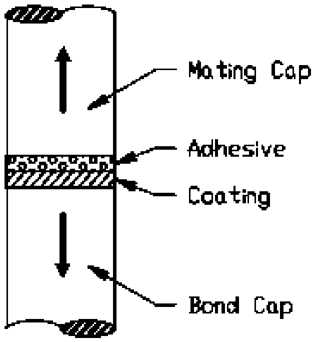

Figure 2.36. Adhesion test configuration according to ASTM C633 [111] (© 2013 Springer Nature) .

2.4.3 Critical Velocity

The critical velocity is defined as the minimum velocity required for the feedstock particles of a given material to bond to a substrate. It is a function of the feedstock powder material, the substrate material, the particle size, the substrate/particle surface and particle oxide content and the temperature of both the substrate and the feedstock material at impact [103], [104], [109], [113], [114].

Velocities that are lower than the critical velocity typically result in the rebounding of the impinging particles and unsuccessful coating build-up. Conversely, velocities that are too high can result in the erosion of the substrate as the rebounding energy of the particles can overcome the bonding energy and therefore, no deposition occurs. Hence, it is important that the impact velocities of the particles lie in the range between the critical velocity and the erosion velocity [109]. **Figure 2.37** shows the range of deposition velocities between the critical velocity (lower boundary, in green) and the erosion velocity (upper boundary, in red) for different materials.

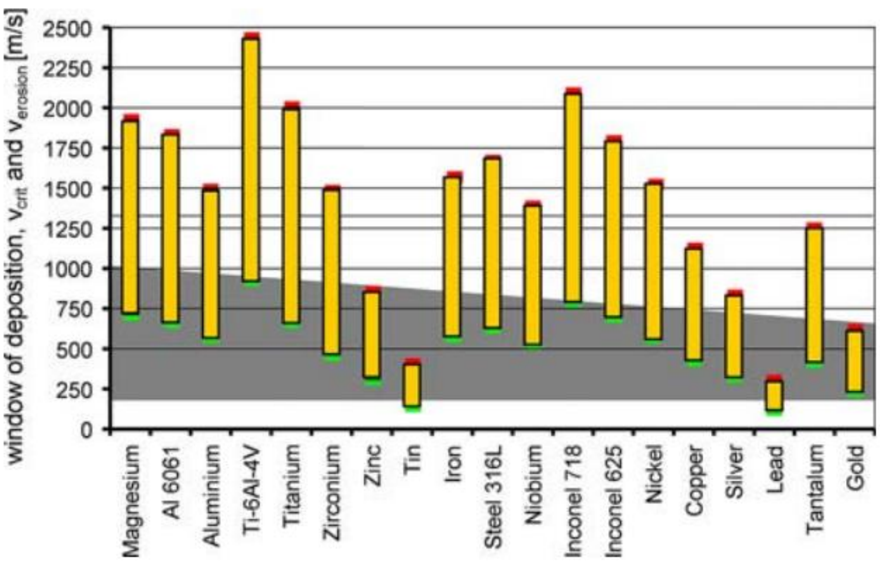

Figure 2.37. Window of deposition of 25 µm particles of different materials sprayed on same-material substrates at an impact temperature of 20°C. The gray area indicates the accessible velocity range using the experimental apparatus in the study [109] (© 2009 Springer Nature).

The particle impact velocity and critical velocity as a function of particle size are presented in **Figure 2.38**. Smaller particles attain higher in-flight velocities than larger particles as dictated by the gas dynamic principles of the process [115]. However, very small particles (< 10 µm) get drastically slowed down by the bow shock that forms in front of the substrate, causing lower impact velocities. Larger particles on the other hand get accelerated to lower velocities than the small particles, but are less decelerated by the bow shock, resulting in higher impact velocities. At a certain size (~ 10 µm in **Figure 2.38**), the impact velocity of the particle reaches a maximum as the effects of the bow shock are essentially overcome and any additional increase in size results in lower in-flight velocities and consequently, lower impact velocities [108], [116].

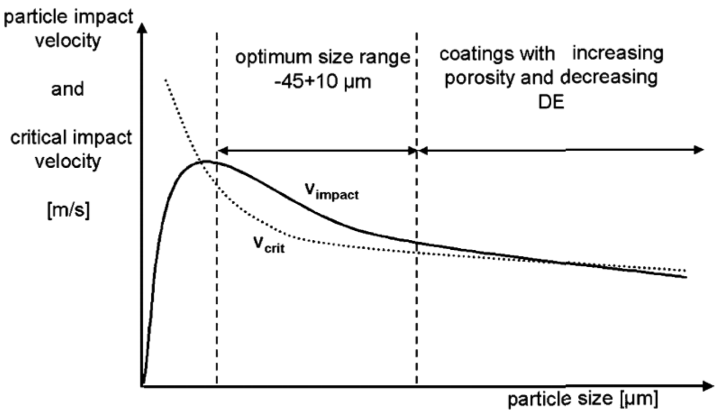

Figure 2.38. The particle impact velocity (v_{impact}) and critical velocity (v_{crit}) function of particle size [108] (© 2006 Elsevier).

The critical velocity is known to decrease with increasing particle size [108], [116]. This is believed to be due to the fact that the surface to volume ratio is high for smaller particles, which translate into higher amounts of oxides hindering bonding and therefore, higher velocities are needed for bonding. Other reasons include heat conduction and strain rate hardening effects [108].

The zone labelled “optimum size range” is ideal for CGDS as the impact velocity is higher than the critical velocity and therefore successful deposition occurs. It is important to select a powder size value in the range where the difference between the impact velocity and the critical velocity curves is maximal, for increased bond strength and coating quality [116].

Finally, it is important to note that the critical velocity between the particle and the substrate is different from the critical velocity between the particles [117].

2.4.4 Deposition Efficiency

Deposition efficiency (DE) represents the ratio of the mass of the powder deposited on the substrate to the total mass of powder sprayed. High DE is not reflective of better coating quality as some materials can be sprayed with high efficiency but form coatings with poor characteristics like pores, poor adhesion and poor cohesion [98], [109]. Increasing the particle velocity, by increasing the gas stagnation pressure or temperature, typically results in higher DE [118]–[120]. **Figure 2.39** shows the DE of zinc and aluminum as a function of the particle velocity.

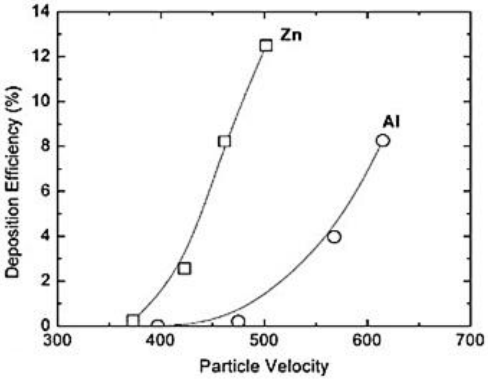

Figure 2.39. DE as a function of particle velocity for zinc and aluminum [119] (© 2007 Springer Nature).

Very high DE values (~ 95%) are usually obtained for high impact velocities [98], [120]. Nevertheless, the velocity must remain under the erosion velocity limit to avoid erosion of the substrate as shown in **Figure 2.40.** For an ideally ductile material, the critical velocity is defined by Schmidt *et al.* to be the impact velocity required to reach a DE of 50%. As the impact velocity increases past the critical velocity, the DE sees a sharp increase and eventually stabilizes close to 100% (saturation limit). After the saturation limit, the DE decreases with further increase in particle impact velocity due to the erosive effects of the impinging particles. By contrast, spraying brittle materials below their melting point results in the erosion of the substrate and therefore loss of mass, which is mathematically equivalent to a negative DE [109].

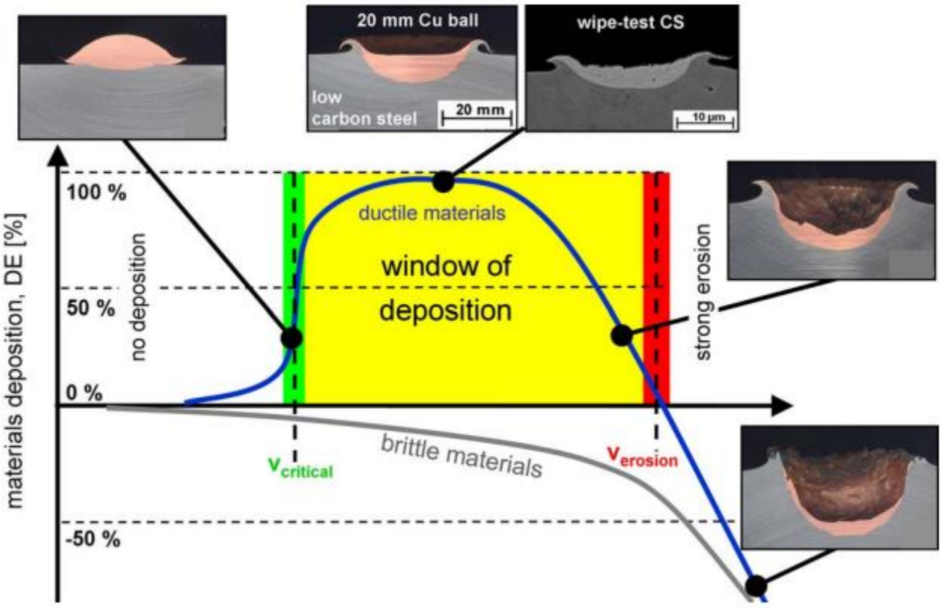

Figure 2.40. Schematic showing the relationship between DE and particle impact velocity for a constant impact temperature [109] (© 2009 Springer Nature).

2.4.5 Gas Dynamic Principles in Cold Gas Dynamic Spray

The performance of the CGDS process depends on the principles of gas dynamics. In order to accelerate the feedstock particles to high velocities, the gas flow must first be accelerated to supersonic velocities in a converging-diverging (de Laval) nozzle. Subsequently, and by the means of drag forces, the momentum of the accelerated gas is transferred to the injected feedstock particles, causing their acceleration before their impingement onto the substrate.

For an ideal gas, the speed of sound C is given by the relation [121], [122]:

$$C = \sqrt{kRT_{gas}} \qquad \textbf{(2.13)}$$

Where k is the gas specific heat ratio, R is the gas constant and T_{gas} is the gas temperature.

The velocity of the gas V_{gas} can be expressed as a function of the speed of sound as follows [121], [122]:

$$V_{gas} = MC = M\sqrt{kRT_{gas}} \tag{2.14}$$

Where M is the Mach number that is dictated by the nozzle's geometry.

The momentum transfer from the gas to the particle obeys Newton's second law:

$$F_p = m_p a_p \tag{2.15}$$

where F_p is the force that the feedstock particle is subjected to, m_p is the mass of the particle and a_p is the acceleration of the particle resulting from the drag forces exerted by the gas flow. The drag force F_D a flow exerts on a solid is given by the following relation [121], [122]:

$$F_D = \frac{1}{2}\rho V^2 C_D A_p \tag{2.16}$$

ρ is the gas density, V is the relative velocity of the flow with respect to the solid, C_D is the drag coefficient and A_p is the projected area of the particle on a plane perpendicular to the direction of the flow.

Since the particle's net force is, neglecting the gravitational effects, only a result of the drag force, **equation (2.15)** is equal to **equation (2.16)**:

$$F_p = m_p a_p = \frac{1}{2}\rho V^2 C_D A_p \tag{2.17}$$

The relative velocity of the flow with respect to the solid particles, is presented as:

$$V = V_{gas} - V_p \tag{2.18}$$

V_{gas} is the absolute velocity of the gas and V_p is the absolute velocity of the injected particle. Therefore, **equation (2.17)** can be written as:

$$F_p = m_p a_p = \frac{1}{2}\rho\left(V_{gas} - V_p\right)^2 C_D A_p \qquad \textbf{(2.19)}$$

Substituting **equation (2.14)** in **equation (2.19):**

$$F_p = m_p a_p = \frac{1}{2}\rho\left(M\sqrt{kRT_{gas}} - V_p\right)^2 C_D A_p \qquad \textbf{(2.20)}$$

If a particle is assumed to be spherical, its mass is computed as follows:

$$m_p = \frac{4}{3}\rho_p\left(\frac{d_p}{2}\right)^3 \qquad \textbf{(2.21)}$$

where ρ_p is the density of the particle and d_p its diameter.

Hence, substituting **equation (2.21)** in **equation (2.20)**, the force applied on a spherical particle injected into the accelerated gas flow is given by:

$$F_p = \frac{4}{3}\rho_p\left(\frac{d_p}{2}\right)^3 a_p = \frac{1}{2}\rho\left(M\sqrt{kRT_{gas}} - V_p\right)^2 C_D A_p \qquad \textbf{(2.22)}$$

From **equation (2.22)**, it is seen that increasing the particle diameter results in a lower acceleration and therefore lower in-flight velocities [114], [120].

Additionally, irregular particles tend to have higher drag coefficients and can therefore reach higher velocities as can be deduced from **equation (2.22)** [123], [124].

Gas temperature is also a crucial parameter in determining the performance of the CGDS process, as demonstrated by the one-dimensional isentropic relation [121], [122]:

$$\frac{T_0}{T_{gas}} = 1 + \frac{k-1}{2} M^2 \tag{2.23}$$

Where T_{gas} is the gas temperature at a given coordinate along the converging-diverging nozzle, T_0 is the gas stagnation temperature. An increase in the gas stagnation temperature would result in an increase in local gas temperature, which is beneficial for accelerating the gas flow as seen in **equation (2.14)**. This increase in the gas temperature results in a larger particle acceleration as per **equation (2.20)** and therefore results in larger in-flight and impact velocity [109], [119], [120], [125]. **Figure 2.41** shows the trend of particle impact velocity as gas temperature is increased.

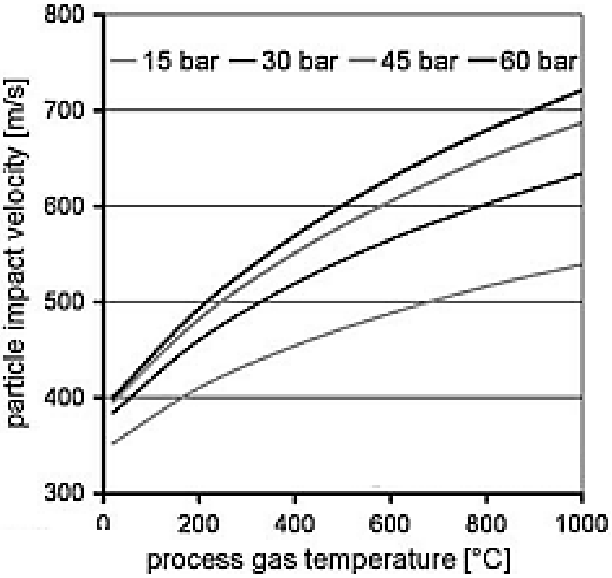

Figure 2.41. Particle impact velocity as a function of the gas flow temperature for 25 µm copper particles sprayed with nitrogen [109] (© 2009 Springer Nature).

Increasing the gas temperature also increases the particle impact temperature for a given gas pressure [109], [118] as illustrated in **Figure 2.42.**

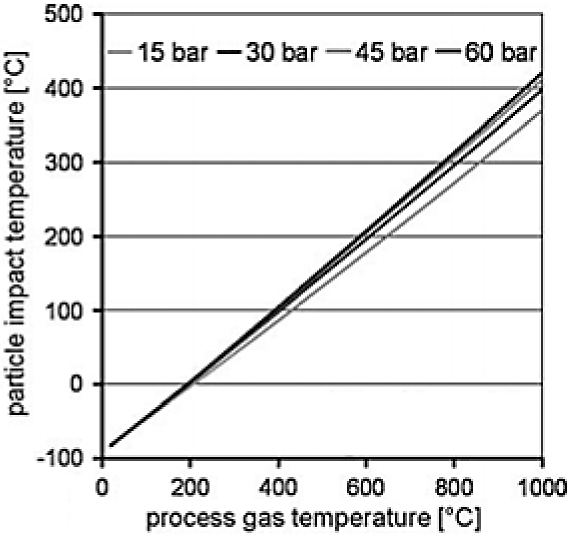

Figure 2.42. Particle impact temperature as a function of the gas flow temperature for a 25 µm copper particles sprayed with nitrogen [109] (© 2009 Springer Nature).

Gas density also affects particle acceleration. The one-dimensional isentropic relation gives the following relationship [121], [122]:

$$\frac{\rho_0}{\rho} = \left(1 + \frac{k-1}{2} M^2\right)^{\frac{1}{k-1}} \quad \textbf{(2.24)}$$

where ρ_0 is the stagnation density.

The stagnation pressure P_0, assuming a perfect gas, can be expressed as a function of the stagnation density and temperature:

$$P_0 = \rho_0 R T_0 \quad \textbf{(2.25)}$$

An increase in the stagnation pressure, assuming a constant stagnation temperature, translates into an increase in the stagnation density as per **equation (2.25)**. This increase in stagnation density engenders an increase in the local flow density ρ as shown in **equation (2.24)** and consequently an increase in the drag force the particle experiences in the flow as per **equation (2.20)**. This increase in drag force ultimately results in higher particle velocities as shown in the previously presented **Figure 2.41** and **Figure 2.42**, and **Figure 2.43** that follows. It is interesting to point out that stagnation pressure variations have no effects on the particle temperature as they do not affect the local gas temperature [118].

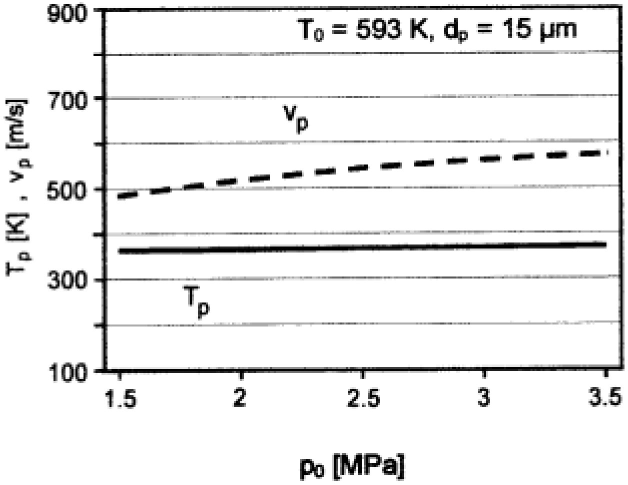

Figure 2.43. Particle temperature (T_p) and velocity (v_p) as a function of the stagnation pressure for a 15µm copper particle sprayed with nitrogen [118] (© 2002 Springer Nature).

Raising the stagnation temperature in **equation (2.25)** for a fixed stagnation pressure causes a decrease in stagnation density. Consequently, following **equation (2.24)**, the flow density decreases with an increase in stagnation temperature for a fixed Mach number (dictated by the nozzle geometry).

Nevertheless, it was shown previously that an increase in the stagnation temperature results in an increase in the local gas temperature along the nozzle (**equation (2.23)**). Therefore, with an increase in stagnation temperature, the flow density decreases but its temperature increases, which according to **equation (2.20)** results in a higher drag force and thus particle acceleration. This is due to the fact that the difference between the flow and particle velocity is squared, whereas particle acceleration varies linearly with gas density.

The choice of the process gas can also affect the performance of the CGDS process. The heat capacity ratio (k or γ) influences the Mach number of the flow, therefore affecting the in-flight velocity of the particles [108], [120], [125]. **Figure 2.44** shows cross-section images of stainless steel coatings sprayed with nitrogen $k = 1.4$ and helium $k = 1.66$, with a considerable increase in DE for the latter. More importantly, it is clear from the figure that the coating sprayed with helium is denser, because of the higher impact velocity.

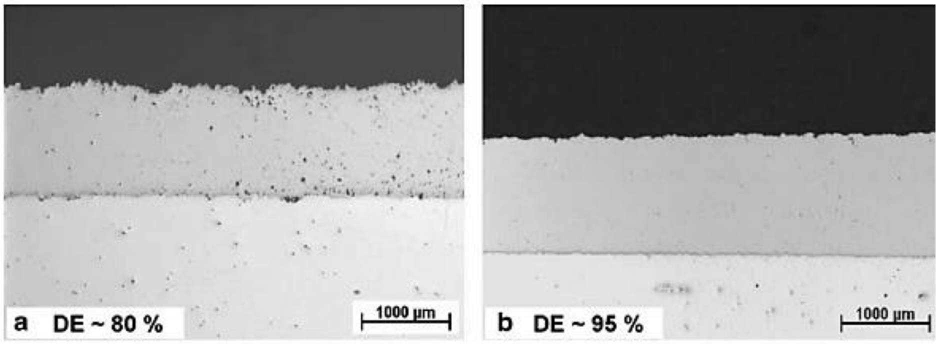

Figure 2.44. Stainless steel 316L sprayed with nitrogen in (a) and helium in (b) with particle size distribution in the range of -45 + 15 µm [108] (© 2006 Elsevier).

Finally, the spray nozzle geometry has an impact on the particle velocity. The local flow Mach number is a function of the local ratio of the cross-sectional area of the nozzle A and the nozzle throat area A^* [121], [122], [126].

$$\frac{A}{A^*} = \frac{1}{M}\left[\left(\frac{2}{k+1}\right)\left(1 + \frac{k-1}{2}M\right)\right]^{\frac{k+1}{2(k-1)}} \tag{2.26}$$

As the cross-sectional area increases for a given throat size in the diverging section of the nozzle (M>1), the Mach number will increase as shown in **Figure 2.45**.

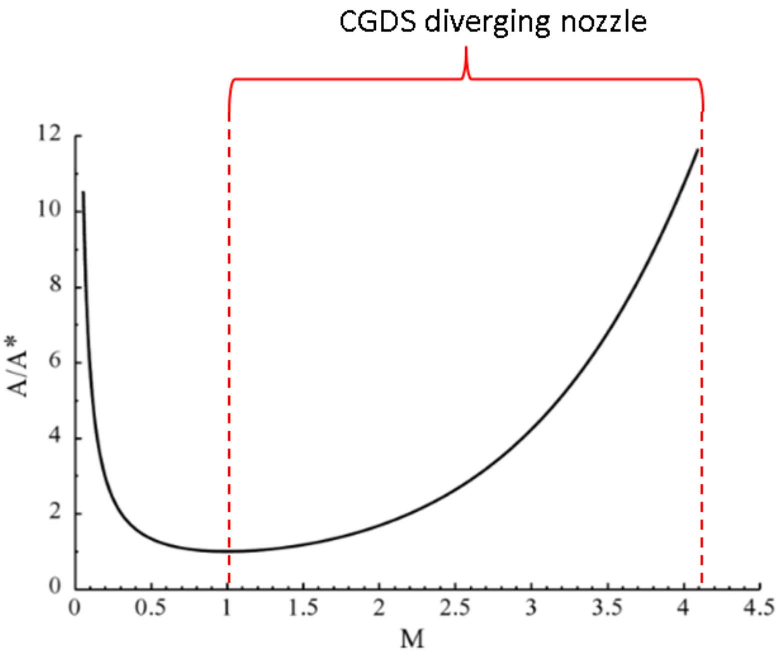

Figure 2.45. The relationship between the area ratio (A/A^*) and the Mach number M of the flow [127] (© 2007 Cambridge University Press).

Hence, the larger the exit of a diverging nozzle is, the higher the theoretical Mach number should be at its exit. Additionally, longer nozzles allow for longer exposure of the particle to the gas flow, which translates into more acceleration. Notwithstanding, design limitations exist because of the impracticality and cumbersomeness of large and extended nozzles, as well as complex interactions between shockwaves and particles at Mach numbers over 2 [128].

2.4.6 Other CGDS Parameters

Higher powder feed rates typically result in thicker coatings. There is, however, a maximum feed rate at which coating thickness reaches a maximum. If the feed rate is further increased past this limit, the coating thickness decreases and eventually coatings delaminate. The delamination at high feed rates is attributed to excessive residual stresses generated by too many impacting particles at a given location on the substrate [129].

The spray nozzle traverse speed also has an influence on coating thickness since, for a fixed feed rate, lower velocities result in longer spray times over similar areas and therefore, thicker coatings. It has also been shown that slower traverse speeds result in more local heating of the substrate by the decelerating gas, which can influence deposition [130].

Finally, the standoff distance, which is the distance between the exit of the nozzle and the substrate, is also an important parameter to consider in CGDS. Standoff distances that are too low typically result in important deceleration of the particle due to the bow shock that forms above the substrate. Standoff distances that are too large on the other hand result in the gas velocity falling below the velocity of the particle, causing it to be subjected to negative drag, which results in particle deceleration and a decrease in DE [131], [132]. **Figure 2.46** shows the effect of the standoff distance on the DE.

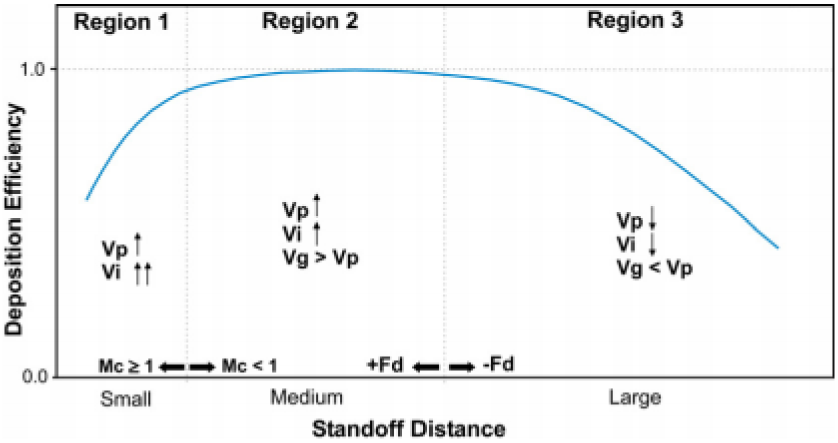

Figure 2.46. Chart displaying the effect of standoff distance on DE. Here F_d is the drag force, M_c is the Mach number, V_g is the gas velocity, V_i is the particle impact velocity and V_p is the in-flight particle velocity [132] (© 2008 Elsevier).

3 Research Objectives

3.1 General Objectives

The main aim of this work was to demonstrate that CGDS, as an AM process, can be used for the fabrication of MEET devices that exhibit good performance, at a relatively low manufacturing cost and that this process can easily be scaled up for production. For the reasons discussed in the literature review, aluminum 6061 was chosen as the electrode material (and substrate) and PEEK as the MEET-capable material. The metallization of polymeric substrates by CGDS has been thoroughly investigated [133]–[140]. However, the deposition of polymeric films on metallic substrates by CGDS is a novel achievement and is still under development [33], [141]–[143]. Thus, the main goals of this work were to: a) find the appropriate parameters for the deposition of PEEK on aluminum substrates and b) test and characterize the power generation properties of the produced MEET device.

The objective of deposition of PEEK on aluminum was divided in secondary objectives: a1) finding the appropriate surface preparation and parameters for PEEK deposition, a2) solving the LCTE discrepancy issues between PEEK and aluminum substrates, a3) improving repeatability by increasing adhesion between the deposited film and the substrate, a4) investigating the effect of substrate size and, a5) solving the pitting and inconsistent thickness issues.

3.2 PEEK Deposition of Aluminum 6061-T6 substrate

3.2.1 Surface Preparation

The first step of this work was to find the appropriate surface preparation to deposit PEEK on aluminum 6061 substrates. As-received, ground and grit-blasted substrates were used with varying spray parameters. Following these experiments, it was concluded that surface roughness resulting from grit-blasting was desirable for the adhesion of PEEK as it delayed delamination.

3.2.2 Thermal Mismatch Mitigation

The next objective of this work was to combine grit-blasted surfaces, which appeared to favour adhesion of the polymer onto the substrate, with a mixture of PEEK/alumina powders instead of pure PEEK powder. Different weight compositions of alumina were added to the PEEK powder in an attempt to decrease its LCTE and mitigate thermal mismatch with the aluminum 6061-T6 substrate. Different spray parameters were investigated for different compositions and the one that yielded the best surface coverage and fewer delamination cases was chosen for future sprays.

3.2.3 Adhesion Improvement – Pure Aluminum Bond Coat

Following the determination of the optimal weight fraction of alumina in the PEEK/alumina mixture, in order to improve adhesion, a bond coat of pure aluminum was deposited by CGDS on a ground aluminum substrate before spraying the PEEK/alumina mixture. The delamination cases of the PEEK/alumina coatings became less frequent; however, substrate size was determined to affect the thermal expansion of the deposited PEEK/alumina, resulting in delamination in some cases.

3.2.4 Substrate Dimensions

The substrate's dimensions were increased and fixed to a predetermined size, to remedy delamination issues on small substrates. Subsequently, pitting and inconsistence film thickness became a problem because of increased local heat dissipation.

3.2.5 Temperature Control

In order to control the thickness of the PEEK/Al_2O_3 layer across the substrate and resolve pitting problems, a strip-heater was used to match the in-spray steady-state surface temperature of the large substrates. Following this step, the appropriate CGDS setup to deposit PEEK/alumina was determined and used for all subsequent sprays.

3.3 Power Generation Assessment of the MEET Device

Following the manufacturing of the layered structure of pure aluminum and PEEK/alumina on aluminum 6061-T6 substrates, the final step of this work was to evaluate the electrical properties of the MEET device. To do so, Arduinos were used to record the voltage generated by the device when in contact with distilled water droplets. The device was connected to a resistor to ensure that power was being dissipated and thus generated continuously. The goal of the experiment was to study the power generation properties of the MEET device as a function of time. Finally, the performance figures of the MEET device, namely the power, power per unit area, current and current density, were computed and compared to those reported by other authors in the literature.

4 Experimental Details

The following section presents the feedstock powders used in this work, the substrate and the surface preparation techniques it was subjected to, the CGDS apparatus and the characterization tools used in the analysis of the deposited films. The equipment used in the data acquisition is also presented and discussed.

4.1 Feedstock Material

Commercially available pure aluminum powder (SST-A5001) (Centerline (Windsor) Ltd. Windsor, Ontario, Canada) was used in this work. It is an irregularly shaped, gas-atomized powder with an average particle size of 26 µm. It is shown in **Figure 4.1**.

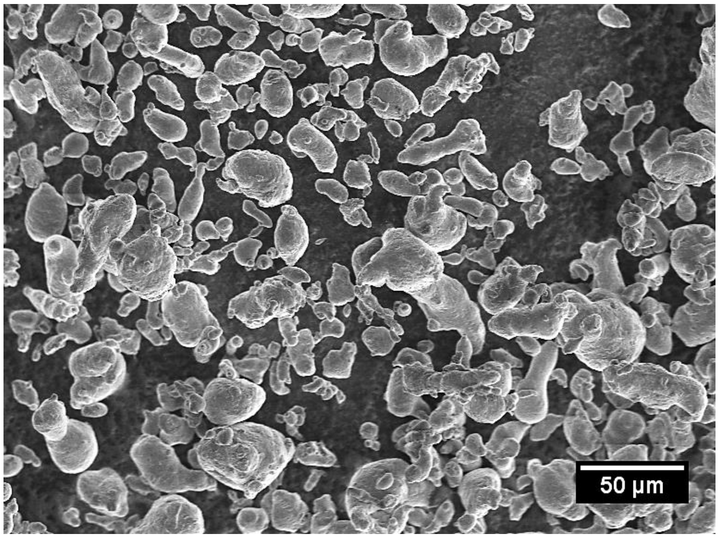

Figure 4.1. SEM image of SST-A5001 pure aluminum powder.

The PEEK powder used in this work was 150G PEEK from VICTREX® (Thornton Cleveleys, Lancashire, England, UK). It is intended for injection molding and it is shown in **Figure 4.2**. The powder appears to be irregular and made of small particles that range in size from 10 to 25 µm, as well as agglomerates (granules) of these small particles that are larger than 100 µm.

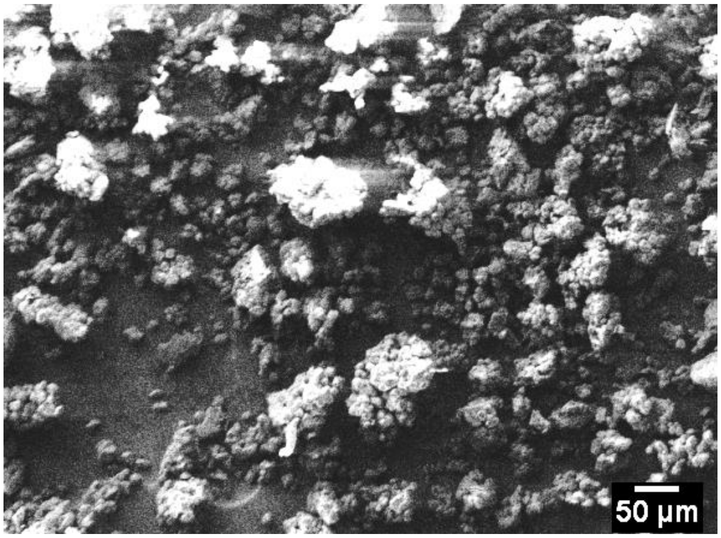

Figure 4.2. SEM image of VICTREX® PEEK 150 G powder.

Finally, alumina powder (SST-G0001) (Centerline (Windsor) Ltd. Windsor, Ontario, Canada) was also used in this work. It is irregularly shape and it is presented in **Figure 4.3**. The powder is angular and has an average size of 22 µm.

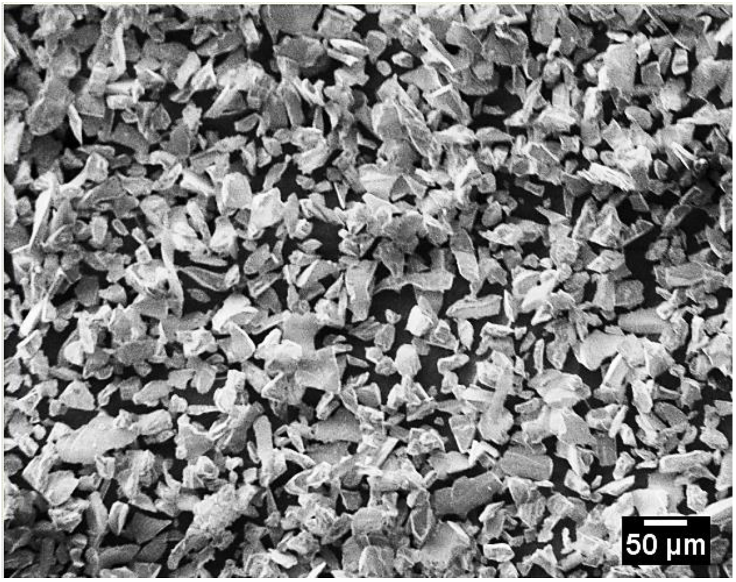

Figure 4.3. SEM image of the SST-G0001 alumina powder.

4.2 Substrate

4.2.1 Aluminum Substrates

The substrates used for the final design of the MEET devices produced in this work were 1/8” (3.175 mm) thick aluminum 6061-T6 QQA-250/11 plates (Metal Pros, Ottawa, Ontario, Canada). The substrates were used to deposit the aluminum bond coat and subsequently the PEEK/Al_2O_3 film via CGDS. Prior to the spray, they were cut to a size of 6” (152.4 mm) by 4” (101.6 mm). A picture of a typical substrate used for the manufacturing of MEET devices by CGDS is shown in **Figure 4.4**.

Figure 4.4. Aluminum substrates used for the production of MEET devices by CGDS.

4.2.2 Substrate Surface Preparation

4.2.2.1 Grit-blasting

In the initial stages of the investigation, grit-blasting was used to enhance adhesion between the PEEK coating and aluminum 6061-T6 substrates.

The grit-blasting unit uses compressed air that is passed through a 5.2 mm inner diameter steel nozzle to accelerate the grit particles. The gun is gravity fed from a hopper that is directly mounted on it. The grit-blasting was done at an approximate angle of 45° with a standoff distance of 50 mm.

The average air consumption of the grit-blasting unit is 6 CFM (170 L/min). The maximum pressure used is 90 psi (621 kPa) (Princess Auto SKU: 8140709).

The grit used in this work is comprised of 1.5 to 3 mm ferrosilicate particles (#EG 20). It is commercially available under the name "Ebonygrit – copper slag blasting abrasive" (Princess Auto SKU: 8200594). Following grit-blasting, the substrates were rinsed with ethanol in an ultrasonic bath for 2 minutes and dried using compressed air.

4.2.2.2 Ground Substrates

Silicon carbide paper was used to manually grind the substrates: P# 80, P# 500 and P# 1200 were used in that order to remove oxides and impurities from the as-received substrates.

The grinding was done in order to enhance adhesion between the aluminum bond coat and the substrate by offering more metallurgical bonding sites [101], [102].

Following grinding and before spraying, the substrates were cleaned with ethanol and dried with compressed air.

4.3 CGDS Apparatus

4.3.1 Heater and Controls

All the films for this research were produced using the commercially available SST Series EP cold spray system from Centerline (Windsor) Ltd., Windsor, ON, Canada. The system uses a 15 kW heater and is rated for a maximum stagnation pressure and temperature of 3.45 MPa (500 psi) and 650°C, respectively.

A control cabinet fitted with a touchscreen for temperature control and a valve for pressure control is used to specify the process' stagnation conditions. The temperature and pressure of the system are regularly calibrated using a Centerline (Windsor) Ltd. calibration kit. The control cabinet and the heater are presented in **Figure 4.5.**

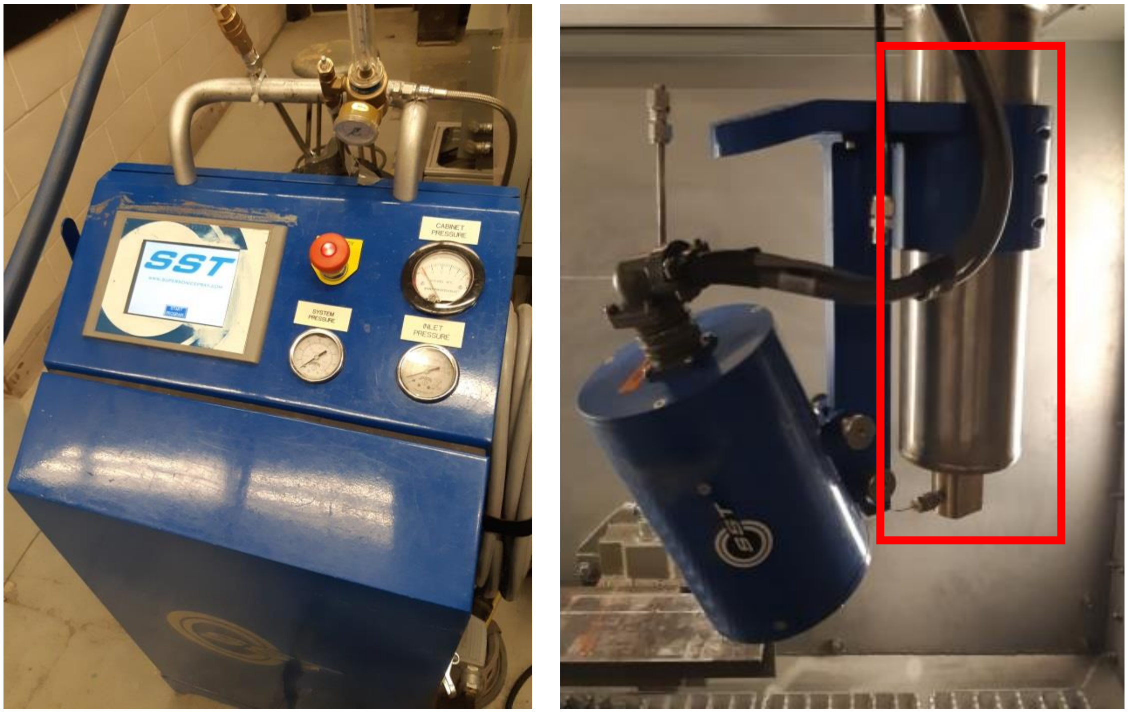

Figure 4.5. CGDS control cabinet (left) and CGDS gas heater (right) shown by the red rectangle.

4.3.2 Robotic Traverse System

An automated traverse system (shown in **Figure 4.6**) controls the movement of the CGDS gun in the X-Y plane. Stepped motors rotate power screws that result in the translation of the gun in the plane of motion. The robotic traverse system is programmed in assembly code in which the displacement of the gun, its speed and its acceleration are controlled. The maximum traverse speed of the system is limited to 200 mm/s.

Figure 4.6. Traverse system used for in the CGDS process (shown by the red rectangle).

4.3.3 Nozzles

Two nozzle assemblies were used in this work. A polymer diverging nozzle was used to spray the pure aluminum powder and a stainless steel diverging nozzle was used for spraying the PEEK/alumina mixture.

For spraying the pure aluminum powder, an SST-Utiflow polymer nozzle (Centerline (Windsor) Ltd., Windsor, ON, Canada) was used. The nozzle is made of Polybenzimidazole (PBI) in order to withstand high spraying parameters without clogging. It has a 2 mm throat and a 6.5 mm exit diameter. **Figure 4.7** shows the PBI diverging nozzle used to spray pure aluminum powder in this work.

Figure 4.7. Centerline (Windsor) Ltd. SST-Utiflow nozzle.

The nozzle assembly is composed of a nozzle holder which connects the powder feed inlet to the diverging polymer nozzle. The converging-diverging section of the nozzle holder houses a compression spring that is loaded by a nozzle fastener. The nozzle holder is connected to the gas heater of the CGDS system via a nozzle holder adapter. The polymer nozzle assembly is shown in **Figure 4.8.**

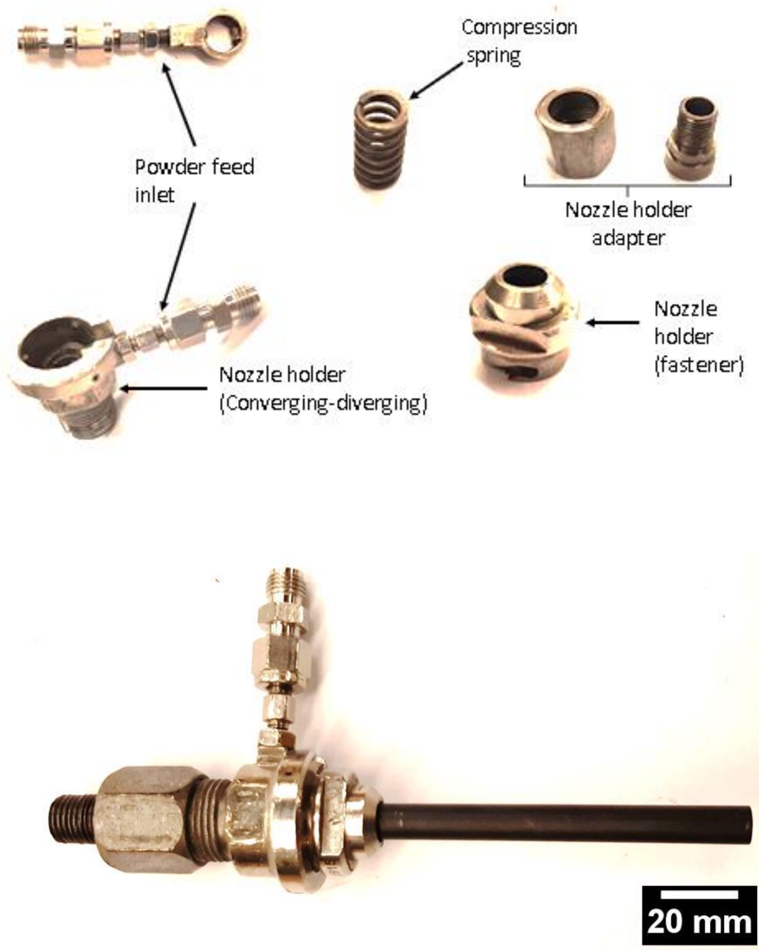

Figure 4.8. Polymer nozzle assembly.

The stainless steel diverging nozzle was procured from Centerline (Windsor) Ltd. and is shown in **Figure 4.9.** It was used to spray the PEEK/alumina mixture as alumina particles would have eroded the polymer nozzle quickly. Moreover, the likelihood of PEEK buildup on stainless steel is low, which minimizes potential clogging issues.

Figure 4.9. Centerline (Windsor) Ltd. Stainless steel nozzle.

The stainless steel nozzle assembly is shown in **Figure 4.10**. The brass orifice (converging-diverging section) has a tungsten carbide powder feed inlet at the throat, to mitigate erosion. The diverging stainless steel nozzle is secured to the brass orifice by a collet and a collet nut. Finally, the nozzle assembly is connected to the CGDS gas heater by the brass orifice and a nut.

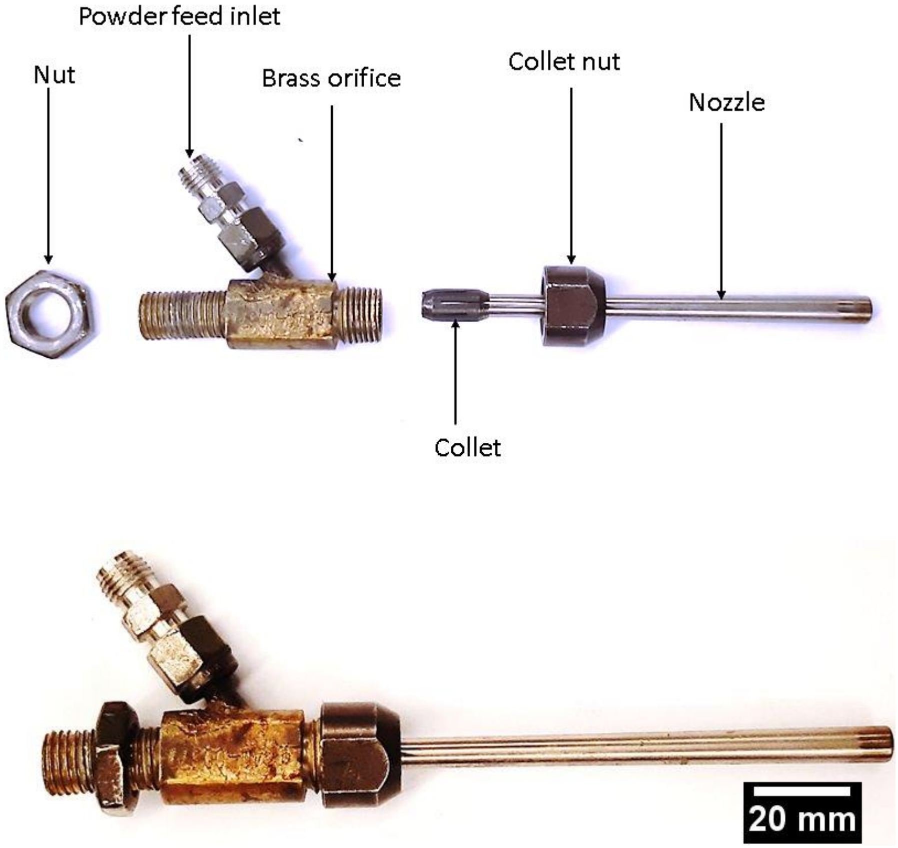

Figure 4.10. Stainless steel nozzle assembly.

4.3.4 Powder Feeding System

The system used to deliver feedstock powder to the CGDS system is a commercially available AT-1200 HP, Thermac Inc. (Appleton, Wisconsin, United States of America). The feedstock powder is poured into a pressurized canister that connects to a perforated wheel and a hammer (**Figure 4.11**). The powder is fed through the holes of the wheel as a result of the periodic tapping of the hammer on the wheel which rotates during the feeding process. Moreover, a carrier gas is used to pressurize the canister (nitrogen in this work) to 0.21 MPa (30 psi) approximately and to push the feedstock particles through the holes of the wheel.

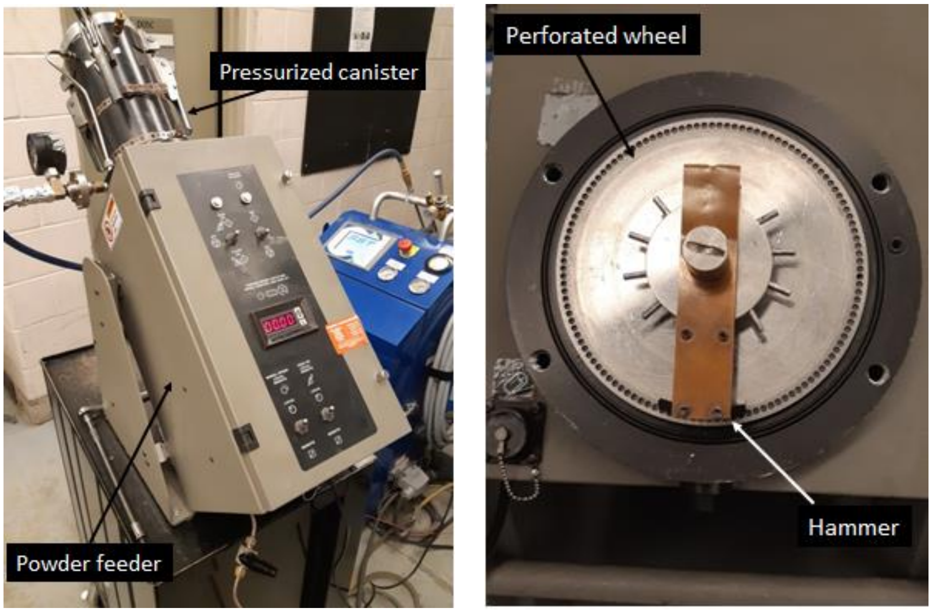

Figure 4.11. Powder feeder assembly (left) and the hammer and perforated wheel (right).

The powder feed rate is controlled by the number of revolutions of the wheel. The powder feeder allows for powder feed rate control by taking the number of revolutions per minute as a user input. The large hole powder feeder wheel was used to feed aluminum to the CGDS system and is shown in **Figure 4.12.**

Figure 4.12. Large hole powder feeder wheel with 120 holes.

The medium hole powder feeder wheel on the other hand was selected to feed the PEEK/alumina mixture to the CGDS system and is shown in **Figure 4.13.**

Figure 4.13. Medium hole powder feeder wheel with 240 holes.

The choice of the wheels was based off the flowability of the feedstock powders and the desired feed rate.

4.3.5 Spray Chamber

The CGDS process takes place in a chamber that is equipped with a dust collection system (shown in **Figure 4.14**). A vacuum is used to pull the mixture of air, gas and non-deposited particles through a water filter to trap the airborne powder particles. Once the particles are removed from the gas, the gas is passed through a HEPA filter and released in the room.

Figure 4.14. CGDS spray chamber and dust collection system.

4.3.6 Gas Delivery System

The nitrogen gas used in the CGDS process was purchased from Messer (Mississauga, Ontario, Canada) in bottle packs containing 11 bottles (**Figure 4.15**). Each bottle pack is initially pressurized at approximately 18 MPa (2600 psi).

Figure 4.15. Nitrogen bottle packs used in the CGDS process.

4.3.7 Strip Heaters

Two strip heaters (TEMPCO, Wood Dale, IL, USA) rated at 300 W and 120 V were connected in parallel and used in the preheating of the substrate. A potentiometer equipped with an ON/OFF temperature control module (Vishay Instruments Inc, Model BAM1, Malvern, PA, USA) was connected to the strip heaters. The potentiometer is fitted with a power control knob that was set to 100% for all experiments and an LED display to take the user's temperature input. In order to match the input temperature set by the user, the potentiometer is connected to an OMEGA type K thermocouple. The strip heater and the potentiometer are presented in **Figure 4.16** that follows.

Figure 4.16. Strip heater (left) and potentiometer (right).

4.4 Characterization Apparatus

4.4.1 Sample Preparation for Microscopic Analysis

All the deposited films were cut with a Struers Secotom-10 (Struers Ltd., Canada) (shown in **Figure 4.17**)

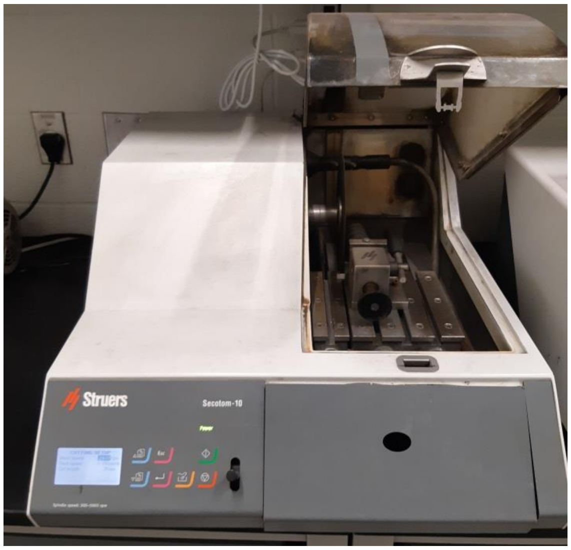

Figure 4.17. Struers Secotom-10 cutting machine.

The cuts were made following the manufacturer's recommended parameters that are presented in **Table 4.1.**

Table 4.1. Recommended cutting parameters.

Parameter	Units	Value
Wheel diameter	mm	200
Wheel speed	rpm	2200
Feed speed	mm/s	0.1

The cutter uses water as a lubricant and is fitted with a moving stage. The embedded software allows for the control of the speed of the moving stage, the cut length and the blade's rotational speed.

The deposited films and MEET devices in this work were all cut from the large aluminum substrates using a silicon carbide blade with an initial diameter of 20 cm as shown **Figure 4.18.**

Figure 4.18. Cut-off wheel used with the Struer Secotom-10 cutting machine.

Figure 4.19 shows a cut sample. These cut samples can be directly used as MEET devices by connecting a top electrode to them, or mounted in resin for microscopic analysis.

Figure 4.19. Cut sample from a larger aluminum substrate.

The mounting process is performed using the Struers LaboPress-3 machine depicted in **Figure 4.20**. The cut samples are inserted into the LaboPress-3 machine and 30 mL of thermosetting epoxy resin (MultiFast Red) are added. Heating is done at 150°C for 6 to 8 minutes and a compacting force of 20 kN is applied. Subsequently, the mounted sample is cooled for 2 to 3 minutes.

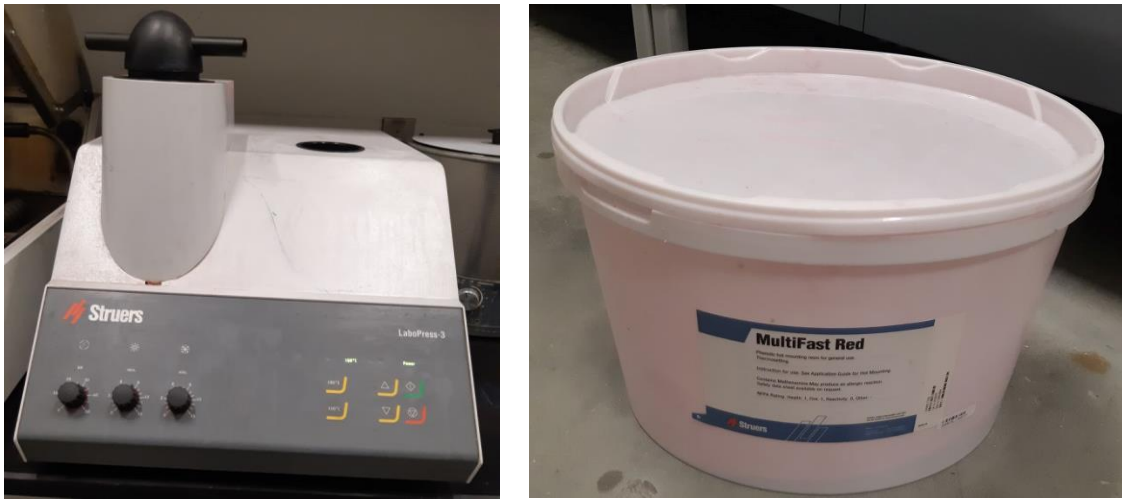

Figure 4.20. Struers LaboPress-3 mounting machine (left) and MultiFast Red resin (right).

The mounted samples were ground and polished using a Struers TegraPol-31 polishing machine, producing samples that are suitable for microscopic analysis. **Figure 4.21** shows the polishing machine and an example of a polished sample. The polishing procedure is presented in **Appendix B: Polishing Procedure**.

Figure 4.21. Struers TegraPol-31 polishing machine (left) and mounted/polished sample.

4.4.2 Optical Microscopy

The produced films were analyzed using an optical microscope (VHX-2000E, Keyence, Canada). The microscope is controlled by a computer fitted with proprietary software that supports progressive scanning, autofocus, image stitching, and fine depth composition to produce fully focused 2D images of three-dimensional surfaces, as well as 3D representations. A control pad allows for stage movement in the XY plane. The microscope's maximum magnification is 1000X. **Figure 4.22** shows the microscope, the computer and the control pad.

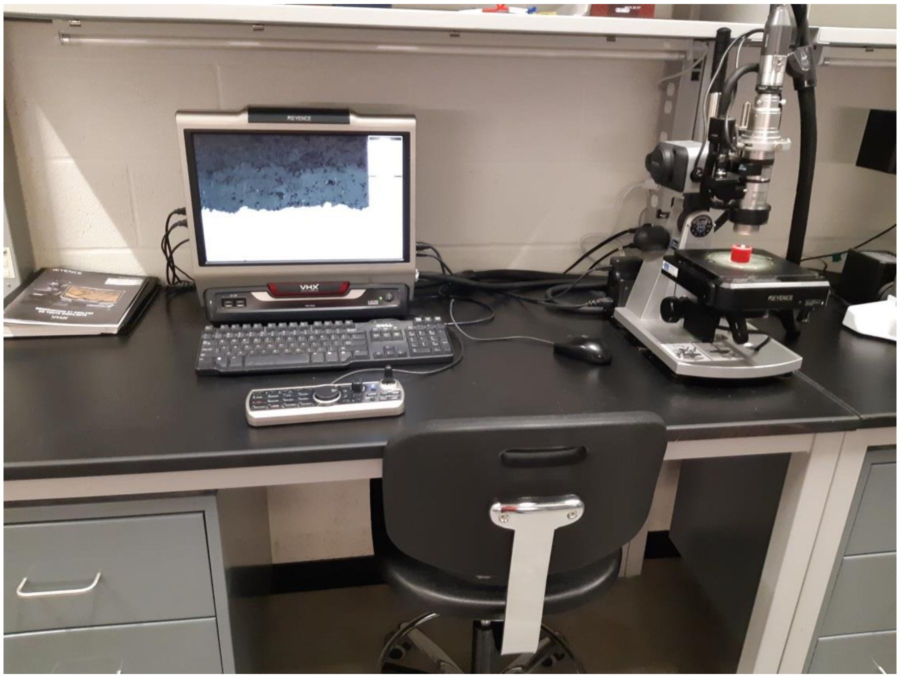

Figure 4.22. VHX-2000E digital optical microscope.

4.4.3 Scanning Electron Microscope

A Scanning Electron Microscope (SEM) was used to further investigate the microstructure of the deposited films. The SEM used in this work (EVO-MA10, Zeiss, UK) is equipped with back-scattered electron (BSE), secondary electron (SE), energy dispersive spectroscopy (EDS), electron backscatter diffraction (EBDS) and X-ray computed tomography (CT) detectors. The SEM system is shown in **Figure 4.23**.

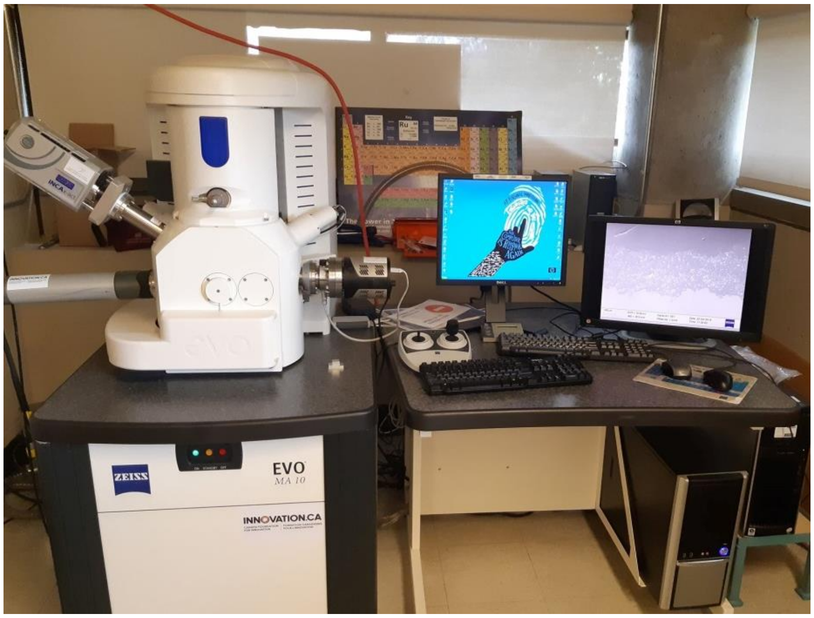

Figure 4.23. Scanning electron microscope (EVO-MA10, Zeiss, UK).

The SE detector was used to acquire high quality images of the films and the feedstock powders. The samples that were subjected to analysis by the SEM were gold sputtered using a Denton Vacuum Desk IV shown in **Figure 4.24**. The fine layer of gold makes the top of the samples conductive. By connecting a piece of copper or carbon tape from the top of the sample to the stainless steel sample holder, a conducting path allows the electrons to flow to the ground. Failure to provide this path results in electron accumulation (charging), which causes impinging electrons to be repelled and gives rise to blurry/bright images.

Figure 4.24. Denton Vacuum Desk IV gold sputtering machine.

4.4.4 Micro-hardness

The micro-hardness of the aluminum substrates and coatings were measured using a Vickers micro-hardness machine (Struers Duramin-1, Struers Inc., Cleveland, OH, USA) shown in **Figure 4.25.** All hardness measurements were taken from mounted and polished samples. The dwell time was set to 10 seconds, with a 980.7 mN (100 gf) load, corresponding to $HV_{0.1}$. All the reported micro-hardness values represent the average of 10 indentations for each sample.

Figure 4.25. Vickers micro-hardness machine.

4.4.5 Surface Roughness Measurements

All surface roughness measurements were made using a portable profilometer (SRG-4000, Phase II Plus, NJ, USA) shown in **Figure 4.26.** The profilometer is fitted with a diamond stylus that has a maximal precision of 0.001 µm and a roughness measurement range spanning from 0.005 to 16 µm for R_a. Cut-off lengths of 0.25 mm, 0.8 mm and 2.5 mm can be selected. The tracing length ranges from 1.3 to 17.5 mm in length.

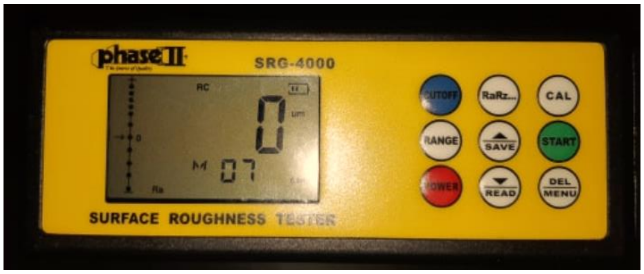

Figure 4.26. Surface roughness gauge.

4.4.6 Power Generation Characterization and Data Acquisition

Distilled water acquired from the University of Ottawa's department of Civil Engineering was used in all experiments.

A Kuman Uno (Arduino R3) microcontroller was used to acquire voltage readings from the MEET device. The ground pin of the microcontroller was connected to the negative lead of the MEET device. In order to read the generated voltage, an Analog In pin of the microcontroller was connected to the positive lead of the MEET device. A schematic of the data acquisition setup is presented in **Figure 4.27**.

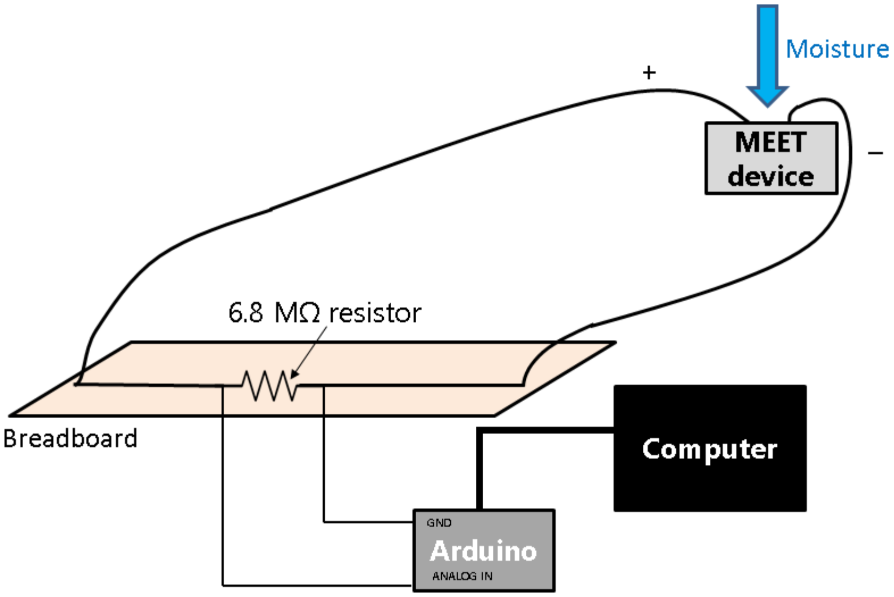

Figure 4.27. Schematic of the data acquisition setup.

The experimental data acquisition setup is shown in **Figure 4.28**.

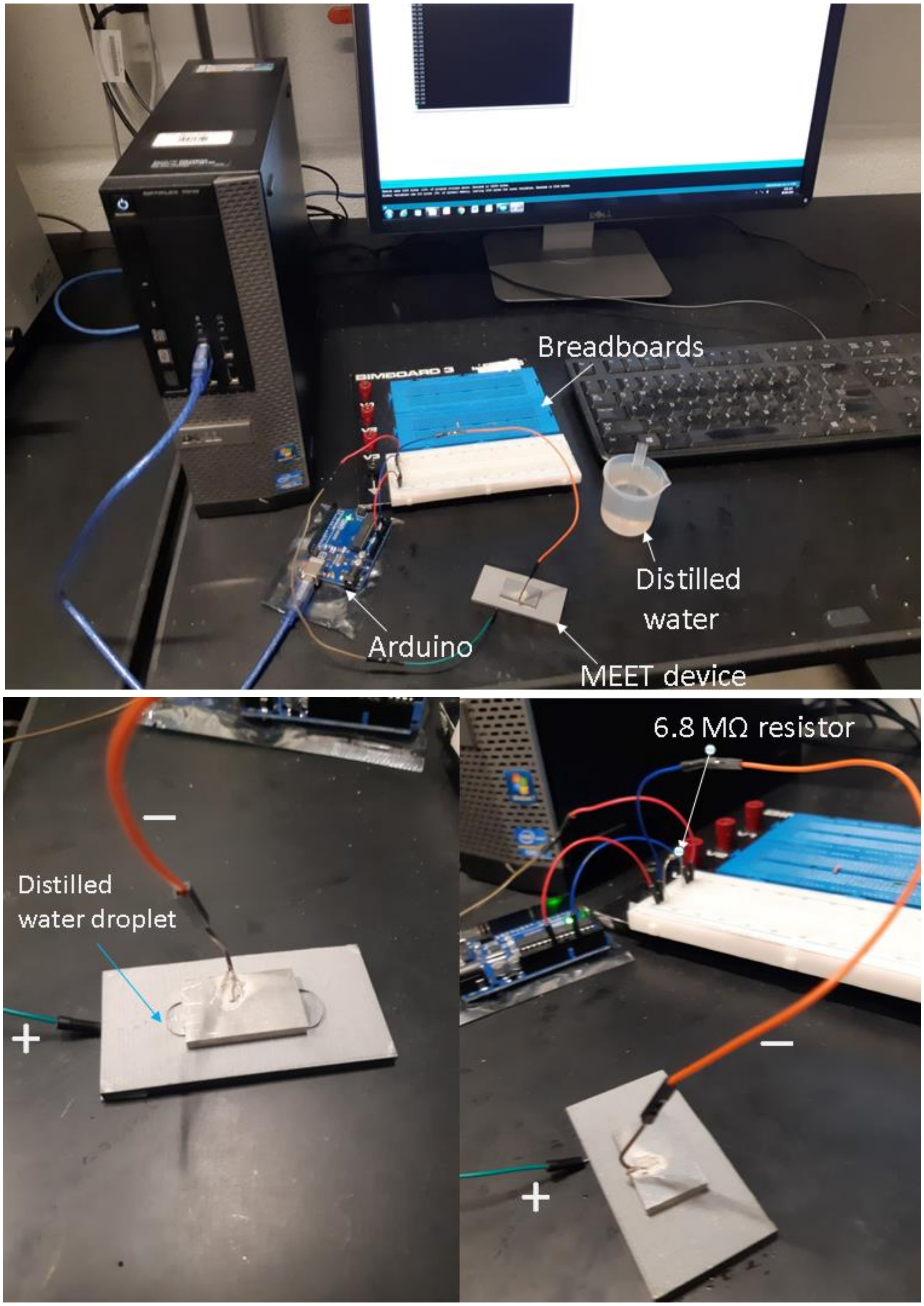

Figure 4.28. Data acquisition setup for the evaluation of the electrical properties of the manufactured MEET device.

6.8 MΩ resistors with a tolerance of ± 5% were connected in parallel to the MEET device in order to ensure that power was constantly being dissipated and thus, generated, following ohm's law:

$$P = \frac{V^2}{R} = RI^2 = VI \tag{4.1}$$

Where P is the electrical power in watts, V the voltage across the resistor in volts and R the value of the resistor in ohms. Another reason for connecting a resistor in parallel with the MEET device is to avoid random readings from the Analog In pins. Given the fact that the MEET devices act as an open-circuit when they are dry, not connecting a resistor between the ground and the Analog In pins would cause the Arduino to return arbitrary voltage readings prior to hydration. Ideally, the resistance should be close to infinite (almost an open-circuit) in order to use the Arduino to measure open-loop values with no parasitic readings; however, 6.8 MΩ was the highest resistor value available to conduct the experiment. It was deemed high enough to simulate near-open-loop conditions.

The data acquisition code was written in the C language (**Appendix A: Arduino Code**), using the Arduino IDE software. The PuTTY program was used to record the voltage readings returned by the microcontroller.

The output of the microcontroller was serialized and printed to the console (COM3). Consequently, PuTTY was set up to record the console output to a text file (.txt).

Once the text files had been acquired, they were converted to .csv format and plotted using MATLAB.

5 Results and Discussion

5.1 Cold Gas Dynamic Spray Parameter Optimization

5.1.1 Pure PEEK Trials

The deposition of PEEK on aluminum 6061-T6 substrates followed a series of iterations. The first hypothesis made in the investigation of the spray parameters of PEEK is that mechanical anchoring is the only mechanism responsible for adhesion. Therefore, aluminum 6061-T6 substrates were grit-blasted to increase their roughness ($R_a = 4.49 \pm 0.67$ µm) and pure PEEK was sprayed onto them. The standoff distance was set to 10 mm so as to avoid drastic deceleration of the particles due to the presence of a bow shock [131], [132]. Multiple trials were conducted and some CGDS parameters were fixed as shown in **Table 5.1.**

Table 5.1. Fixed CGDS parameters for the initial investigation of pure PEEK deposition on 6061-T6 substrates.

Parameter	Value
Traverse speed	2 mm/s
Step size	1 mm
Feed wheel type	240 medium holes
Powder feed rate	4 g/min
Powder feeder gas flow rate	0.85 m^3/h
Powder feeder and propellant gas	Nitrogen
Standoff distance	10 mm
Nozzle type	SS nozzle

The only parameters varied for the initial investigation of the spray parameters of PEEK on aluminum 6061-T6 substrates were the stagnation temperature and pressure. **Table 5.2** shows the parameter window used in the experiment and the observations made for every set of parameters.

Table 5.2. Stagnation pressures and temperatures chosen for the initial investigation of the spray parameters of PEEK on aluminum 6061-T6 substrates.

Stagnation temperature [°C]	Stagnation pressure [MPa]	Observation
100	0.69	No deposition
	1.38	No deposition
	2.07	No deposition
	2.76	No deposition
200	0.69	No deposition
	1.38	No deposition
	2.07	No deposition
	2.76	No deposition
300	0.69	No deposition
	1.38	No deposition
	2.07	Deposition followed by delamination
	2.76	Deposition followed by delamination
400	0.69	No Deposition
	1.38	No Deposition
	2.07	Deposition followed by delamination
	2.76	Deposition followed by delamination

The ground and as-received substrates had little and brief PEEK buildup during the spray, most of which got blown away by the nitrogen gas. This delamination was attributed to the poor adhesion of the first layer of PEEK particles to the substrate. In some rare occurrences, PEEK lumps formed on the substrate as shown in **Figure 5.1**. These lumps could easily be removed by hand.

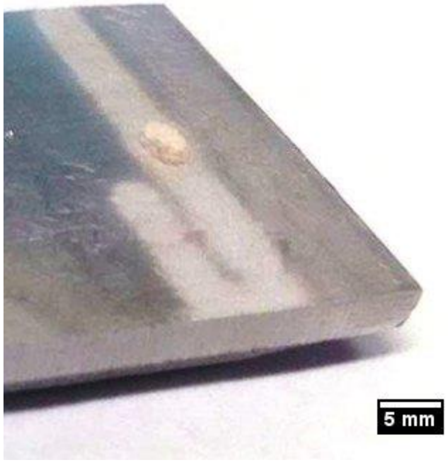

Figure 5.1. Pure PEEK trail on an as-received 6061-T6 substrate (400°C, 2.07 MPa, 2 mm/s).

On the other hand, grit-blasted surfaces had thicker PEEK deposits. It appeared that the surface roughness of the substrate delayed the delamination of the first layer, resulting in thicker PEEK buildups as shown in **Figure 5.2.** In some cases, delamination only occurred after the spray, reflecting the thermal stresses to which the polymer is subjected as a result of heating and cooling.

Figure 5.2. Delaminated trail of pure PEEK from a grit-blasted substrate (400°C, 2.07 MPa, 2 mm/s).

It was therefore concluded that the adhesion of the PEEK coatings to the substrate was the factor preventing coating formation. PEEK's cohesion appeared to be achievable at temperatures and pressures of 400°C and 2.07 MPa respectively, based on **Figure 5.1** and **Figure 5.2**.

5.1.2 PEEK/Alumina Mixture

From the previous experiment, it was concluded that surface roughness was beneficial in the deposition of PEEK on aluminum 6061-T6 substrates. Nevertheless, because of the different LCTEs of PEEK (47×10^{-6} °C^{-1} below T_g to 140×10^{-6} °C^{-1} above T_g) and aluminum (23.6×10^{-6} °C^{-1} with only small variations over a wide range of temperatures) [26], [29], [64], [67], [68], it was hypothesized that thermal stresses ultimately resulted in delamination.

LCTE is an important variable to take into consideration when combining dissimilar materials using thermal spray processes, especially polymers and metals.

The metallization of polymeric substrates or polymer matrix composites requires the LCTE of the metal coating to be close or similar to that of the substrate to minimize thermal stresses [133], [144].

Consequently, in an effort to minimize the discrepancy in the LCTE of PEEK and aluminum 6061-T6, alumina powder was added to the PEEK powder in three different weight percentages: 33%wt., 50 %wt. and 80 %wt. It has been shown by Goyal *et al.* that the addition of aluminum oxide to PEEK causes a decrease in the LCTE of PEEK to a point where it matches that of aluminum [72] as discussed in the **Thermal Properties of PEEK** section and shown in **Figure 2.20**.

Given the fact that the amount of alumina in the feedstock powder and the amount of alumina in the coating can be different, multiple compositions were tested and evaluated [141], [145]–[149]. Moreover, the addition of ceramics to metallic powders has been shown to assist with mechanical anchoring as the ceramic particles create asperities on the substrate and previously deposited particles, facilitating mechanical interlocking [146].

The traverse speed was increased to 70 mm/s in an attempt to decrease the thickness of the PEEK deposits as MEET applications require coatings in the thickness range of a few nanometers to a few hundred microns [13]–[15], [18], [61]. The aluminum 6061-T6 substrates were grit-blasted prior to the investigation. **Table 5.3** sums up the fixed parameters for all the trials.

Table 5.3. Fixed CGDS parameters for the investigation of PEEK/alumina deposition on 6061-T6 substrates.

Parameter	**Value**
Traverse speed	70 mm/s
Step size	1 mm
Feed wheel type	240 medium holes
Powder feed rate	4 g/min
Powder feeder gas flow rate	0.85 m^3/h
Powder feeder and propellant gas	Nitrogen
Standoff distance	10 mm
Nozzle type	SS nozzle

For each weight percentage composition (33% wt., 50 %wt. and 80 %wt. alumina), the stagnation pressure and temperature were varied and observations were made. **Table 5.4** shows a summary of the experiments' parameter window and the respective observations.

Table 5.4. Stagnation pressures and temperatures chosen for the investigation of the spray parameters of PEEK/alumina mixtures on aluminum 6061-T6 substrates and their following observations.

%wt. alumina	Stagnation pressure [MPa]	Stagnation temperature [°C]					
		150	250	300	350	400	450
33	1.03	No deposition	Hard coating, scattered coverage	Hard coating, scattered coverage		Post-spray delamination	
	2.07			Pits			
	2.76						
50	1.03	No deposition	Hard coating, scattered coverage	Pits	Pits	Post-spray delamination	
	2.07				Good adhesion, no pits		
	2.76				Pits		
80	1.03	No deposition	Hard coating, scattered coverage			Pits + post-spray delamination	
	2.07						
	2.76						

Only the 50 %wt. alumina PEEK/alumina mixture resulted in the successful formation of a full coating without pits or bare patches at 350°C and 2.07 MPa. It was therefore determined that the 50 %wt. alumina in PEEK/alumina was the optimal amount of ceramic out of the three compositions investigated. Consequently, the coatings at this composition were characterized as a function of the stagnation temperature and pressure and the following observations were made (explanations follow on **p. 95, p. 96**):

1. At 150 °C, there was no deposition over the three chosen stagnation pressures of 1.03 MPa, 2.07 MPa and 2.76 MPa.
2. At 250 °C, as the stagnation pressure was increased from 1.03 to 2.76 MPa, there was less coverage of the substrate.
3. At 300 °C, as the pressure was increased from 1.03 to 2.76 MPa, larger and deeper pits formed.
4. At 350 °C and 1.03 MPa, the obtained coatings had pits but did not delaminate. At 2.07 MPa, a coating with no pits that did not undergo post-spray delamination was obtained. At 2.76 MPa, a coating with pits was formed and also did not delaminate.
5. At 400 °C, as the pressure is increased from 1.03 to 2.76 MPa, the coatings get thicker but also rougher. The same trend is observed for 450 °C as the pressure is increased. The coatings sprayed at 450 °C are thicker than those sprayed at 400 °C for the same stagnation pressure. It is important to point out that at both stagnation temperatures and over all stagnation pressures, post-spray delamination occurred.

Table 5.5 gives a visual summary of the coatings obtained with 50 %wt. alumina in PEEK/alumina mixture.

Table 5.5. Top view of PEEK/alumina coatings obtained for 50 %wt. alumina in PEEK/alumina mixtures.

Gas stagnation pressure [MPa]	Gas stagnation temperature [°C]				
	250	300	350	400	450
2.76		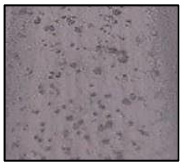	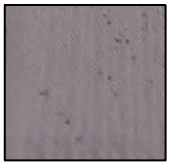	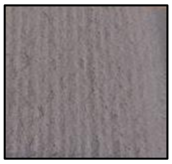	
2.07	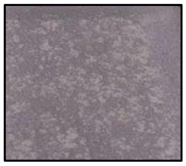				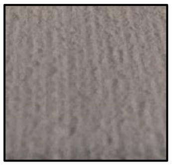
1.03			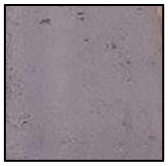	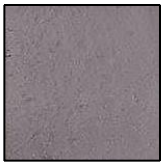	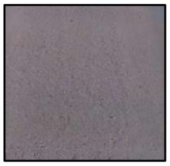

At low stagnation temperatures (below 150°C), there was no deposition on the substrate as the PEEK particles are too hard and most likely do not reach T_g (147°C) to accommodate for sufficient deformation. In fact, in other thermal spray processes (High Velocity Oxy-Fuel (HVOF), High Velocity Air Fuel (HVAF), flame spraying and plasma spraying), the upper temperature limit is the thermal degradation temperature, whereas the lower temperature limit is the melting temperature of the polymer. Hence, despite not melting the feedstock powder in CGDS, it is beneficial to increase the polymer particles' temperature to get adequate plastic deformation [150].

At stagnation temperatures of 250°C and 300°C, the PEEK particles are softer than at 150°C but are still relatively hard for successful coating formation [150]. As a result, full coverage of the substrate is not achieved. As the pressure is increased, at 250 °C and 300 °C, alumina particles cause more erosion of the deposited PEEK particles, resulting in more pits (dark visible spots in the top view images of the coatings) at higher pressures. This erosion behaviour has been observed during the metallization of polymers, where at high pressures, metal particles cause the erosion of polymeric substrates [136], [151]. This is believed to be applicable to ceramic particles (alumina in this case) because they are harder than metals [67].

All deposits obtained between 250°C and 350°C inclusively did not delaminate.

At 400°C and 450°C, despite their satisfactory appearance, post-spray delamination of the coatings occurred in all cases. This delamination is attributed to the thermal mismatch between the PEEK/alumina film and the aluminum 6061-T6 substrate, which is more pronounced at higher temperatures [26], [29], [68], [152].

Finally, at 350°C, the PEEK powder appears to be soft enough for essentially full coverage of the substrate. Nevertheless, lower pressures (1.03 MPa) and higher pressures (2.76 MPa) result in erosion of the coating and consequently, pitting. At 2.07 MPa however, there was full-coverage of the substrate and no pits. This can be explained by the fact that these stagnation conditions (2.07 MPa, 350°C) fall in an optimal trade-off region, where the temperature is high enough to accommodate for sufficient plastic deformation of the PEEK particles but is low enough to mitigate thermal stresses with the aluminum 6061-T6 substrate. The pressure on the other hand is high enough to allow alumina particles to create asperities onto the pure aluminum bond coat and the previously deposited PEEK particles, but it is also low enough to minimize the erosion of the previously deposited PEEK particles by both the impinging PEEK and alumina particles [137], [142].

Table 5.6 shows the effect of particle temperature and velocity on the quality of the PEEK – 50 %wt. alumina coating, including the optimal (trade-off) region.

Table 5.6. The effects of particle temperature and particle velocity on the PEEK – 50 %wt. alumina coatings.

Variable	Low	Optimal range	High
PEEK particle temperature	Insufficient plastic deformation	Sufficient plastic deformation of the PEEK particles, minimal erosion, sufficient asperity creation (successful trade-off)	Thermal stresses due to LCTE mismatch between PEEK and aluminum that cause bending and delamination
Alumina particle velocity (stagnation conditions)	Erosion of previously deposited PEEK particles, insufficient asperity creation		Erosion of previously deposited PEEK particles
PEEK particle velocity (stagnation conditions)	Erosion of the previously deposited PEEK particles, insufficient plastic deformation		Erosion of previously deposited PEEK particles

Figure 5.3 shows the summarized trends observed with a PEEK – 50%wt. alumina feedstock powder.

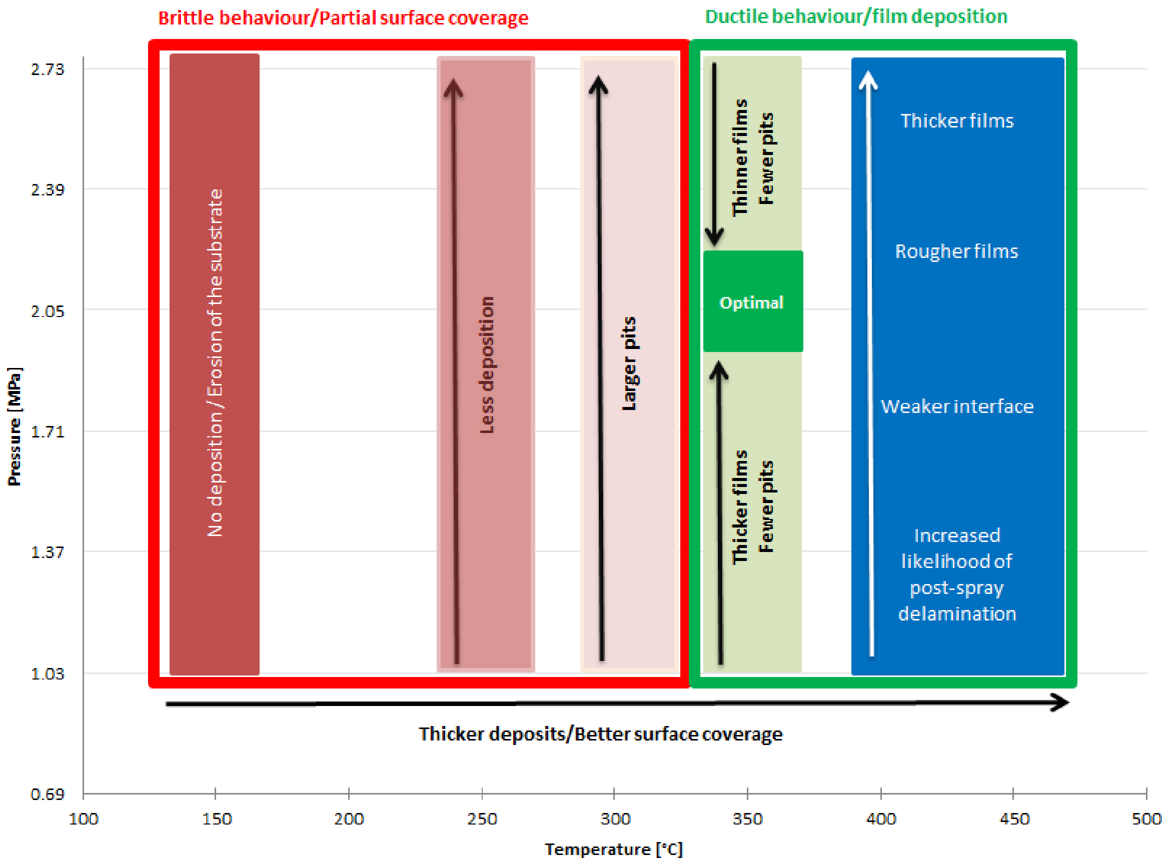

Figure 5.3. Characterization of the spray parameters of PEEK – 50 %wt. alumina over different stagnation conditions.

The findings of this characterization resulted in the use of the spray parameters for PEEK – 50% wt. alumina summed up in **Table 5.7** for all subsequent sprays.

Table 5.7. CGDS parameters for PEEK – 50%wt. alumina.

Parameter	Value
Gas pressure	2.07 MPa
Gas temperature	350 °C
Traverse speed	100 mm/s
Step size	1 mm
Feed wheel type	240 medium holes
Powder feed rate	4 g/min, 2 g/min
Powder feeder gas flow rate	0.85 m^3/h
Powder feeder and propellant gas	Nitrogen
Standoff distance	10 mm
Nozzle type	SS nozzle

5.1.3 Pure Aluminum Bond Coat Development

As more sprays were done following the parameters presented in **Table 5.7**, it became apparent that reproducibility was an issue: in some cases, the PEEK – 50 %wt. alumina film would undergo post-spray delamination. In some other cases, pits would form in the coating.

At this stage of the research, too many variables were at play to isolate the source of the problem; therefore, the focus was directed towards improving the adhesion between the substrate and the PEEK – 50 %wt. alumina film.

To further improve adhesion, an intermediate layer that separates the 6061-T6 substrate and the PEEK – 50% wt. film was considered. This intermediate layer would be deposited by

CGDS in order to increase the surface roughness required for the polymer to adhere. Moreover, this intermediate layer would have a hardness that is lower than that of the substrate, in order to maximize the effects of surface roughening of the impacting alumina particles.

Consequently, it was deemed reasonable to spray a pure aluminum bond coat on the aluminum 6061-T6 substrate prior to spraying the PEEK – 50 %wt. alumina film. Pure aluminum, even when deposited by CGDS and therefore, subjected to cold work, is softer than the 6061-T6 alloy [153]–[155]. The CGDS process would allow for the deposition of a thin layer of it (in the order of magnitude of hundreds of microns) [156], [157], therefore not significantly altering the initial design. Moreover, coatings produced by CGDS tend to have roughness values that are higher than grit-blasted surfaces [157], [158]. **Figure 5.4** shows the attempted layered structure.

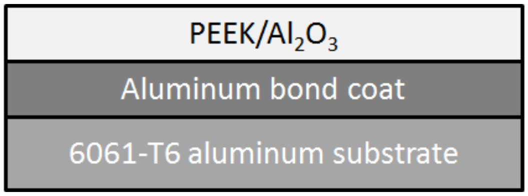

Figure 5.4. Schematic of the attempted layered structure of the MEET devices.

The aluminum 6061-T6 substrate was ground using silicon carbide paper (FEPA P#80, P#500 and P#1200) to clean its native oxide that covers the surface and promote more metallurgical bonding with the pure aluminum powder [159]–[161]. The substrates were subsequently rinsed with ethanol before the spray to dissolve any organic contaminants.

The spray parameters for pure aluminum were selected based upon the manufacturer's recommendations and are presented in **Table 5.8**.

Table 5.8. CGDS parameters for the pure aluminum bond coat.

Parameter	Value
Gas pressure	2.76 MPa
Gas temperature	400 °C
Traverse speed	100 mm/s
Step size	1 mm
Feed wheel type	120 large holes
Powder feed rate	5.5 g/min
Powder feeder gas flow rate	0.85 m^3/h
Powder feeder and propellant gas	Nitrogen
Standoff distance	15 mm
Nozzle type	Polymer nozzle

The introduction of a pure aluminum bond coat resulted in the successful deposition of the PEEK – 50 %wt. alumina film and no in-spray or post-spray delamination issues. Consequently, in order to understand the contribution of this bond coat, the hardness of the grit-blasted aluminum 6061-T6 substrate and the aluminum bond coat were measured prior to spraying the PEEK – 50 %wt. alumina film. The roughness values (R_a) were also evaluated for both surfaces using a profilometer. The results of the measurements are summarized in **Table 5.9** that follows.

Table 5.9. Comparison of the hardness and roughness values of the grit-blasted aluminum 6061-T6 substrate and the pure aluminum bond coat.

	$HV_{0.1}$	R_a [µm]
Aluminum bond coat	53.88 ± 4.78	11.98 ± 1.23
Grit-blasted 6061-T6 substrate	123.3 ± 7.16	4.69 ± 0.83

The aluminum bond coat is softer than the aluminum 6061-T6 substrate (53.88 ± 4.78 $HV_{0.1}$ and 123.3 ± 7.16 $HV_{0.1}$, respectively), and also has a higher roughness (R_a = 11.98 ± 1.23 µm and 4.69 ± 0.83 µm, respectively). These values match those reported in the literature [153], [154].

Figure 5.5 shows the cross-sectional view of an aluminum 6061-T6 substrate with a pure aluminum bond coat and a PEEK – 50%wt. alumina film sprayed according to the parameters in **Table 5.8** and **Table 5.7** (with 4 g/min feed rate) respectively.

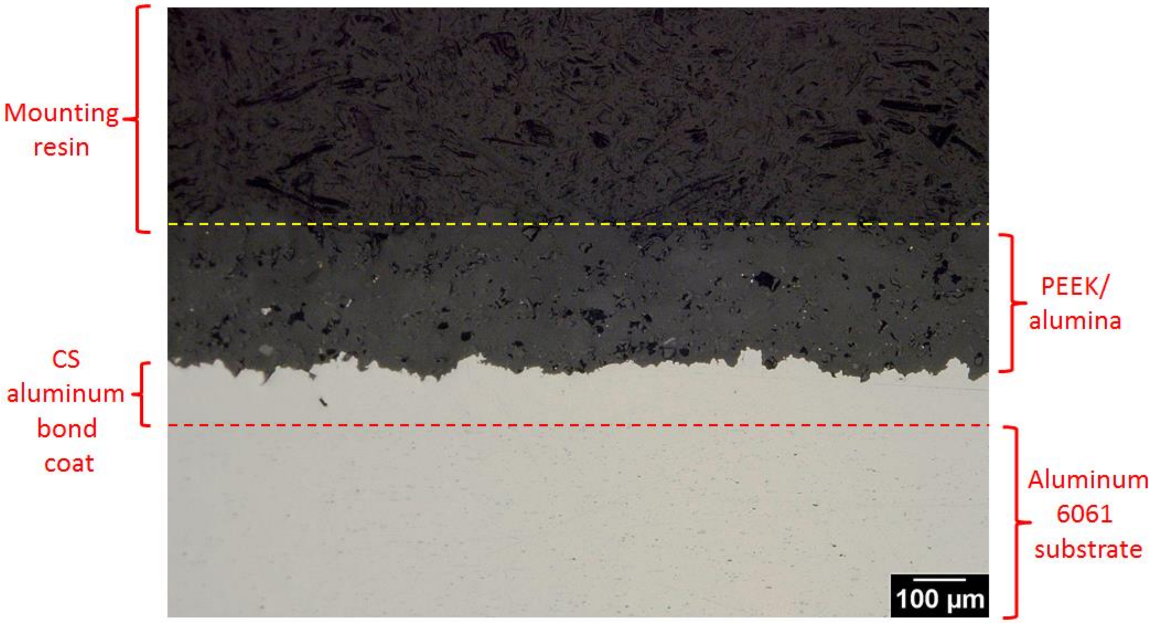

Figure 5.5. The layered structure of the MEET device comprised of aluminum 6061-T6 substrate, a pure aluminum bond coat and a PEEK – 50 %wt alumina.

In an attempt to better understand the adhesion mechanism of the PEEK – 50 %wt. alumina film on the pure aluminum bond coat, SEM analysis of the coatings was performed on the successfully deposited coatings. **Figure 5.6** shows the cross-sectional view of the interface between the PEEK – 50 %wt. alumina film and the pure aluminum bond coat.

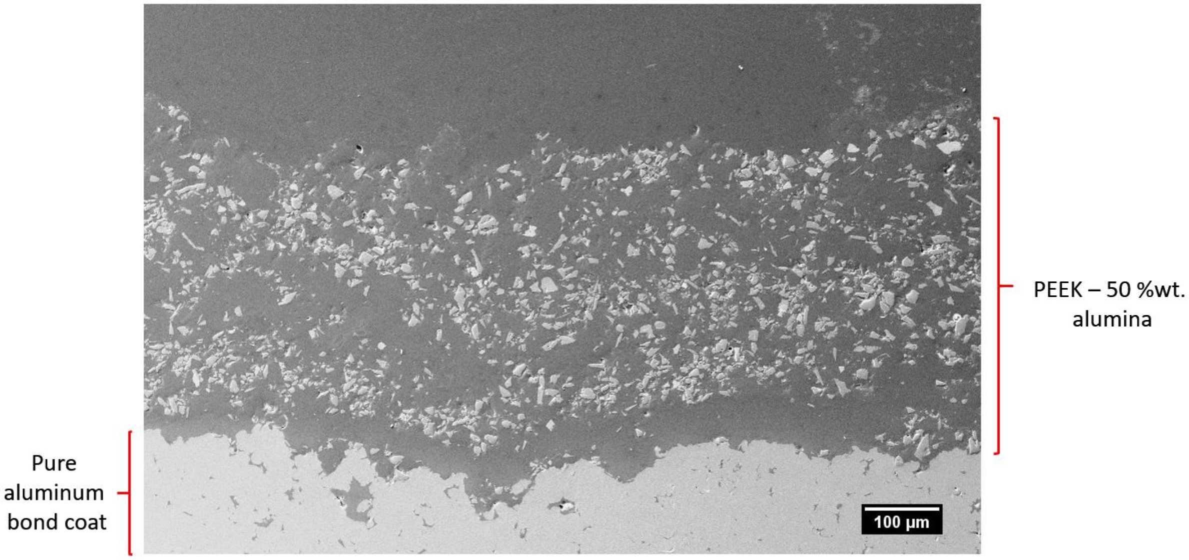

Figure 5.6. SEM image showing the interface between a PEEK – 50 %wt. alumina film deposited on a pure aluminum bond coat.

The first layer directly in contact with the pure aluminum bond coat appears to have very few alumina particles in it. This reflects the first role of the alumina particles, which is to create asperities on the substrate and previously deposited particles to improve the mechanical anchoring between the pure PEEK particles and the pure aluminum bond coat [146]. Some alumina particles inevitably get embedded in the aluminum bond coat, but for the most part, the interface between the aluminum bond coat and the PEEK – 50 %wt. alumina coating is comprised of adjacent pure aluminum and pure PEEK regions.

If the temperature of the particles is low, they do not anchor onto the asperities, because of insufficient plastic deformation. Nevertheless, the asperities have a positive impact on the adhesion under the condition that the pure PEEK particles are at temperature that is sufficiently high to accommodate for sufficient plastic deformation [150]. The adhesion improvement role of the alumina particles essentially resolved the in-spray delamination issue. To solve the post-spray delamination problem, the alumina particles played a role in decreasing the LCTE of the PEEK – 50 %wt. alumina film [72].

5.1.4 Substrate Size

Small substrates of aluminum 6061-T6 were cut to dimensions 40 mm x 30 mm x 3.175 mm to produce near-net shape parts. They were subsequently ground before the pure aluminum bond coat was sprayed onto them according to the parameters in **Table 5.8.**

PEEK – 50%wt. alumina was subsequently sprayed on the aluminum bond coat according to the parameters in **Table 5.7**.

Despite previously achieving successful deposition of the pure aluminum bond coat and the PEEK – 50%wt. alumina film, inconsistency issues kept emerging as more sprays were conducted. It was observed that delamination occurred on these small substrates, making substrate size a parameter to take into consideration. The delamination of the PEEK – 50 %wt. alumina films was attributed to the fact that small substrates got hotter and colder rapidly during and after the spray respectively, resulting in more pronounced thermal stresses. Insulation was introduced in order to minimize the thermal cycling, without success.

Therefore, the decision to make the aluminum 6061-T6 substrates larger was made. They were cut to size 152.4 mm x 101.6 mm x 3.175 mm. Insulation was used with the larger substrates to ensure more repeatability: as more sprays are conducted, the vice used in the CGDS setup and shown in **Figure 5.7** gets hotter, which leads to inconsistent spray conditions.

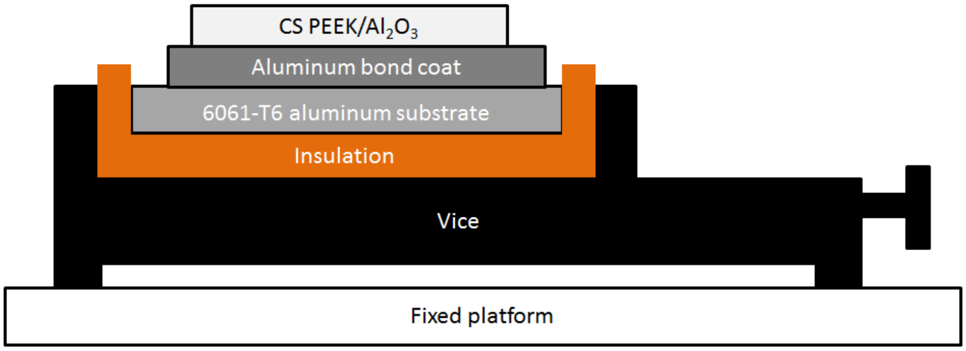

Figure 5.7. Initial CGDS setup.

To produce a continuous PEEK – 50 %wt. alumina coating on top of the pure aluminum bond coat, the CGDS gun must sweep across the substrate in cycles, as illustrated in **Figure 5.8**. The number of cycles defines the width of the coating in the x axis.

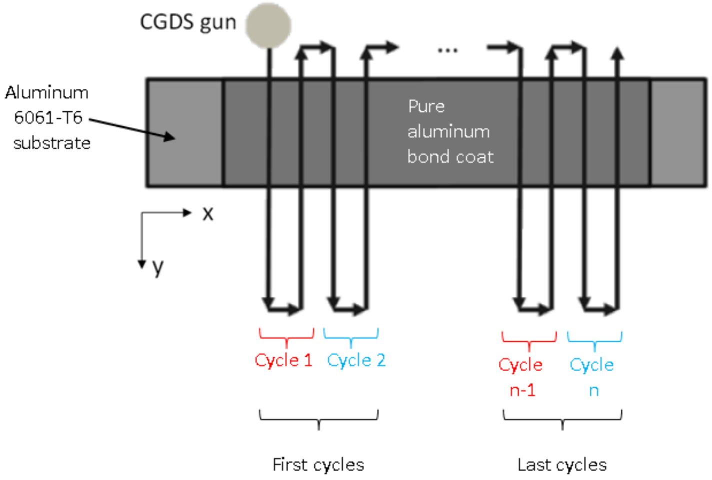

Figure 5.8. Schematic illustrating the cycling of the CGDS gun required for the deposition of coatings.

Increasing the size of the substrate solved all the delamination issues and hence, improved repeatability. Nevertheless, because of the larger substrates and thus larger volume of material, heat conduction from the region that is directly under the CGDS gun to the bulk of the substrate was enhanced. Therefore, local heat dissipation by conduction in the bulk was more pronounced and pitting remained a problem, especially during the first few cycles of the gun (**Figure 5.8**), as the substrate starts at room temperature.

The pits most likely formed because of the poor adhesion between the cold substrate and the pure PEEK particles. In HVOF, HVAF, flame spraying and plasma spraying, it is reported that spraying polymers onto cold substrates or spraying powder particles that are not sufficiently heated results in the formation of pits [150]. **Figure 5.9** shows bare regions of pure aluminum that are not covered by the PEEK – 50 %wt. alumina film.

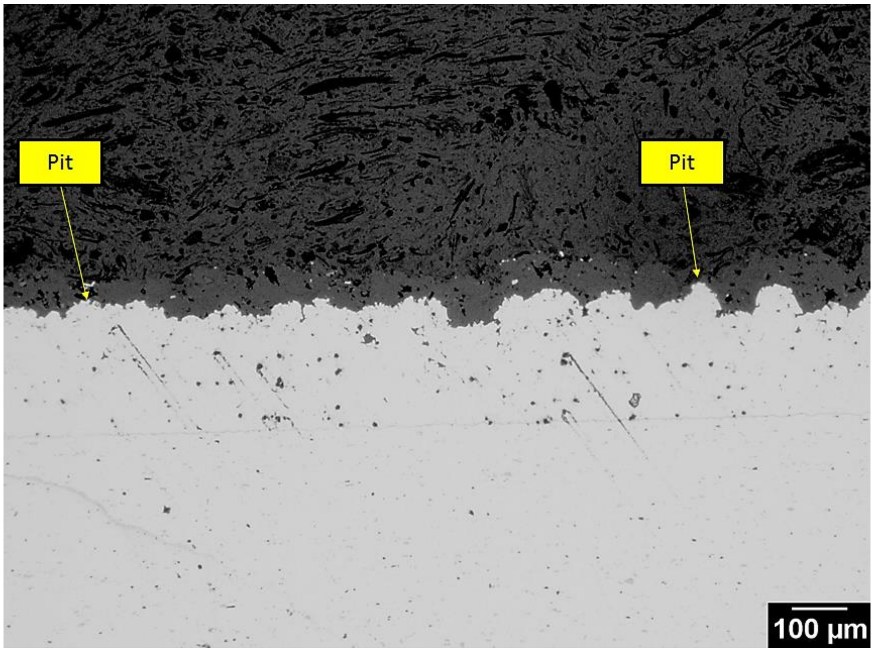

Figure 5.9. Optical microscope image of a PEEK – 50 %wt. alumina coating on a pure aluminum bond coat, showing pits.

Another issue associated with using large substrates is the non-uniform thickness of the PEEK – 50 % wt. alumina film. The first few cycles of the CGDS gun encounter a cold substrate and therefore, result in thin or no deposits. On the other hand, the last few cycles of the CGDS gun are run over a substrate that has been heated by the hot gas flow for a longer time. As a result, the last gun cycles produce more continuous and thicker coatings as the number of cycles (and consequently the spray time) increases as shown in **Figure 5.10**.

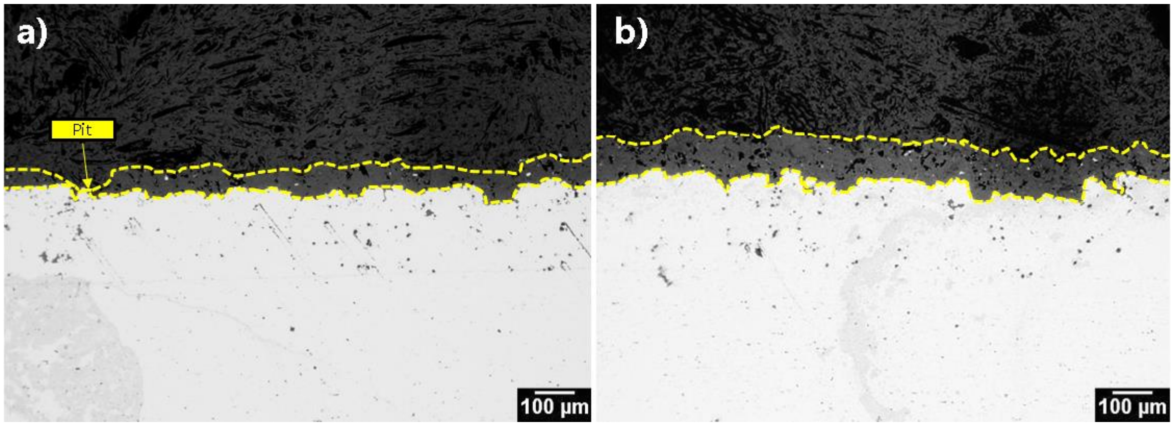

Figure 5.10. Cross-sectional view of the PEEK – 50 %wt. alumina film, (a) first gun cycles, (b) last gun cycles.

Figure 5.11 presents a schematic of the non-uniform PEEK – 50 %wt. alumina film thickness and the temperature profile of the substrate during the spray.

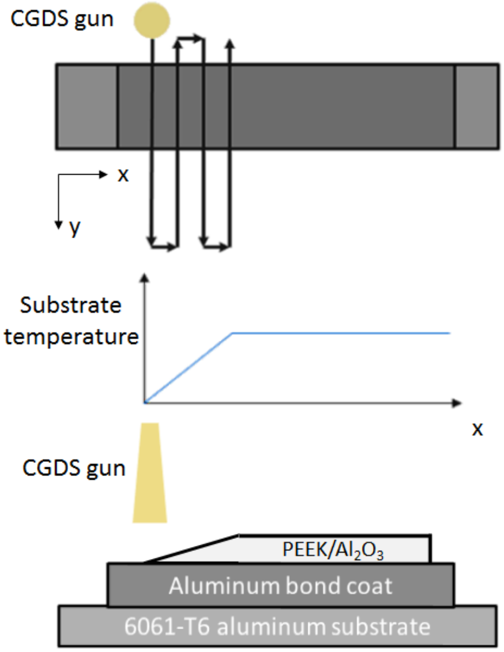

Figure 5.11. Inconsistent PEEK – 50 %wt. alumina film thickness along the cross-section.

5.1.5 Substrate Preheating

In order to resolve the pitting and non-uniform thickness issues, substrate preheating was considered.

The first step to take before implementing substrate preheating would be to determine the steady-state temperature of the substrate when subjected to the gas flow with the exact same conditions as **Table 5.7**, without powder particles.

To measure the steady-state temperature of the substrate, a thermocouple was placed at the edge of the aluminum 6061-T6 substrate, away from the gas flow. **Figure 5.12** shows the experimental setup used in this investigation.

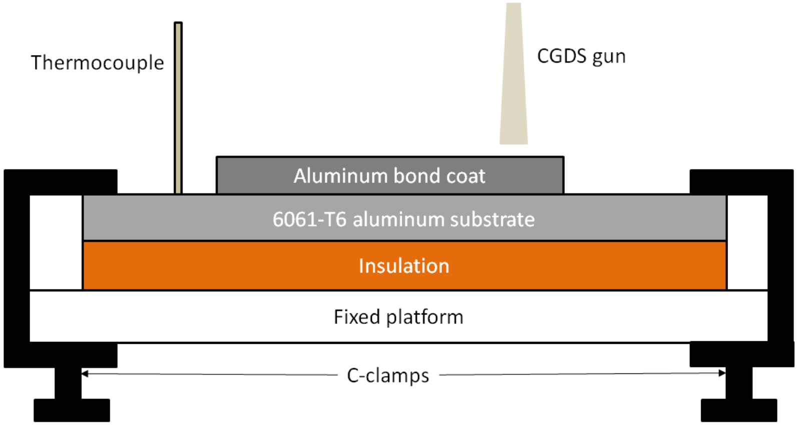

Figure 5.12. Experimental setup used for the measurement of the steady-state temperature of the substrate during the spray of the PEEK – 50%wt. alumina film on the pure aluminum bond coat.

The goal of this experiment was to measure the in-spray steady-state temperature of the substrate by means of pure conduction. Once this temperature has been measured, it would be set as the initial temperature of the substrate. With substrate preheating set to this steady-state temperature, all the points contained in the spray plane would have similar thermal histories during the spray and therefore, have relatively similar PEEK – 50% wt. coating buildups.

Multiple passes were done until the temperature of the substrate reached a constant value. This temperature was found to be 85°C. Consequently, the new and final spray setup included strip heaters in order to ensure a constant substrate temperature during the deposition of PEEK – 50 %wt. as shown in **Figure 5.13.**

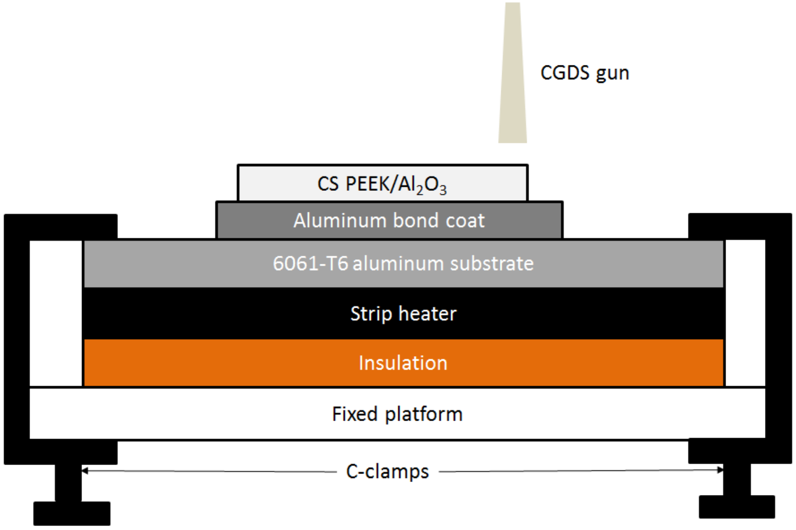

Figure 5.13. Schematic of the final CGDS setup.

The C-clamps press the top part of the aluminum 6061-T6 substrate and the fixed platform together, both of which are made of metal (respectively aluminum and steel). Therefore, there is heat transfer between these two surfaces; nevertheless, this heat transfer was deemed negligible as most of the substrate is insulated from the fixed platform. A picture of the actual experimental setup is presented in **Figure 5.14.**

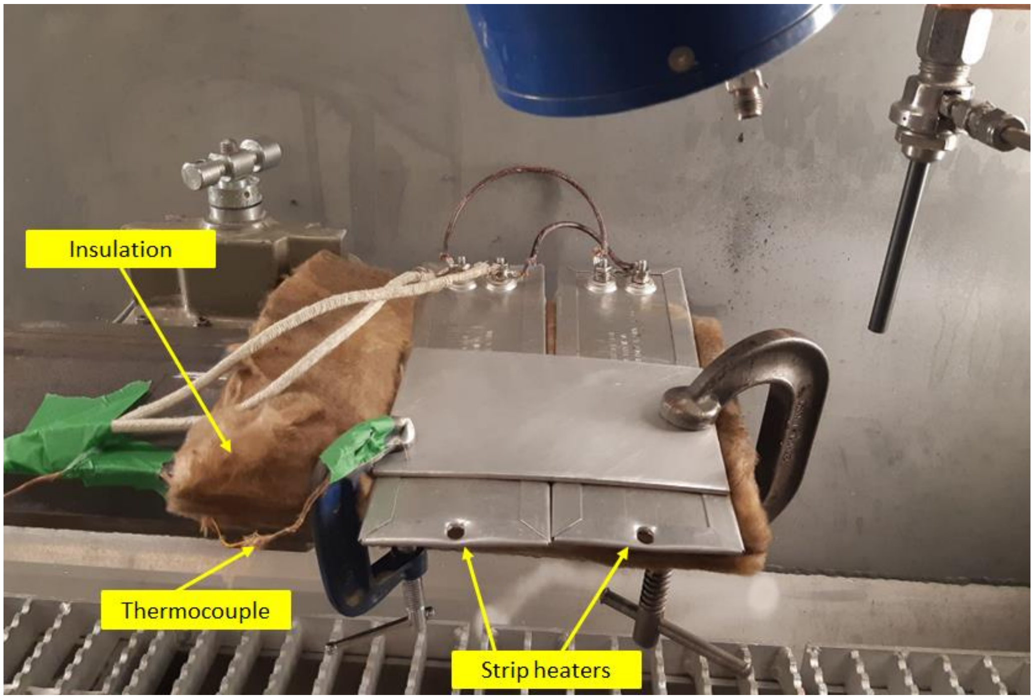

Figure 5.14. Final experimental setup.

The steady-state temperature of 85°C was inputted to the potentiometer that controls the power of the strip heaters for all subsequent sprays.

With substrate preheating, all pitting issues were resolved. The cross-sectional images of the PEEK – 50 %wt. alumina films on pure aluminum bond coats show more thickness uniformity as presented in **Figure 5.15.**

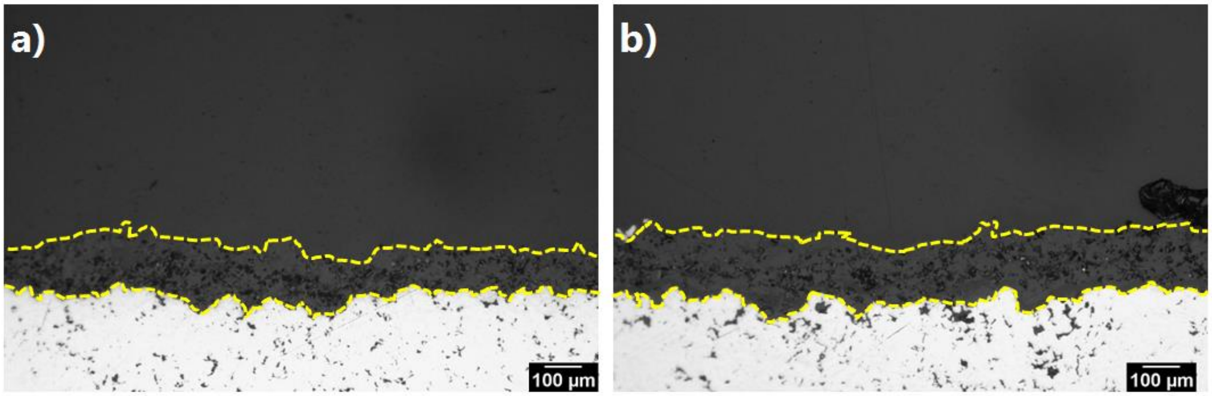

Figure 5.15. Cross-sectional view of the PEEK – 50 %wt. alumina film, (a) first gun cycles and (b) last gun cycles, both with substrate preheating at 85°C.

Despite being more uniform, the thickness of the PEEK – 50 %wt. alumina film appears to be slightly higher for the last few cycles of the gun. This is attributed to the fact that the automated control system of the strip heater is an ON/OFF one: it is too aggressive during the spray and sometimes adds extra heat to the substrate when the CGDS gun steps off the substrate. When the gun steps off the substrate, important gas mixing takes place inside the spray chamber and convection heat transfer is higher, resulting in an apparently lower substrate temperature. As a result, the thermocouple returns a temperature reading that is lower than the initial preheating temperature and the control system overcompensates by adding more power to the strip heaters. Hence, as the spray goes on, more gas mixing takes place inside the chamber, resulting in substrate temperatures that are slightly higher than the initial preheating temperature, due to the reactivity of the control system.

5.1.6 Summary

In order to sum up the workflow of the deposition of PEEK on aluminum 6061-T6 substrate, a flow chart is presented in **Figure 5.16**.

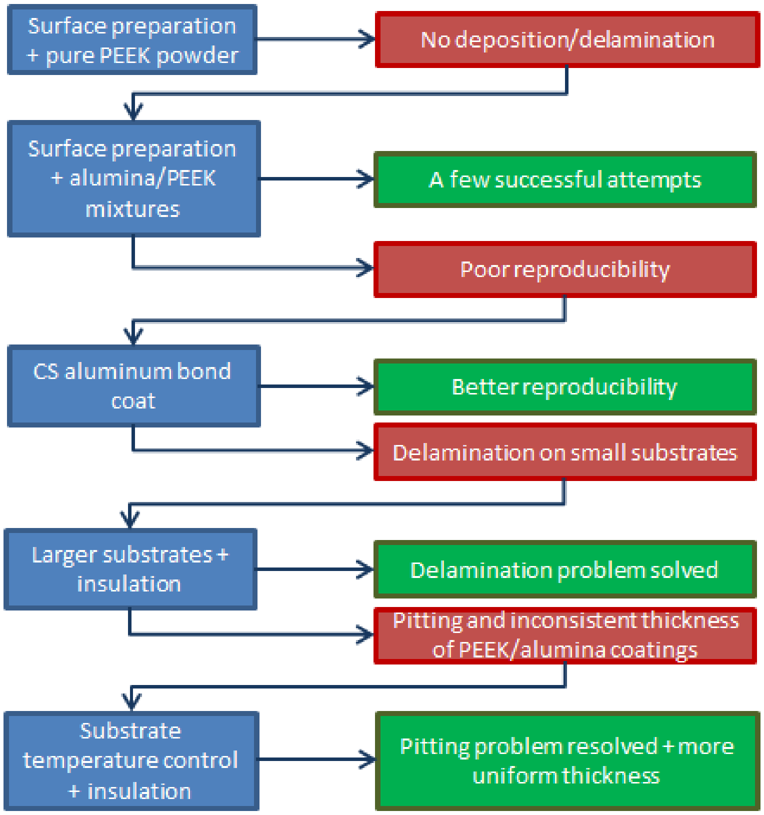

Figure 5.16. Workflow showing the steps undertaken in the development of the PEEK – 50 %wt. alumina film on aluminum 6061-T6 substrates via CGDS.

This workflow resulted in the successful deposition of PEEK – 50 %wt. alumina on the pure aluminum bond coat. All delamination, inconsistent thickness and pitting problems were resolved following the steps shown in **Figure 5.16**. The sprayed substrates were cut to different sizes to be used as the bottom electrode of the MEET devices. The final design of the bottom electrode of the MEET devices is shown in **Figure 5.17**.

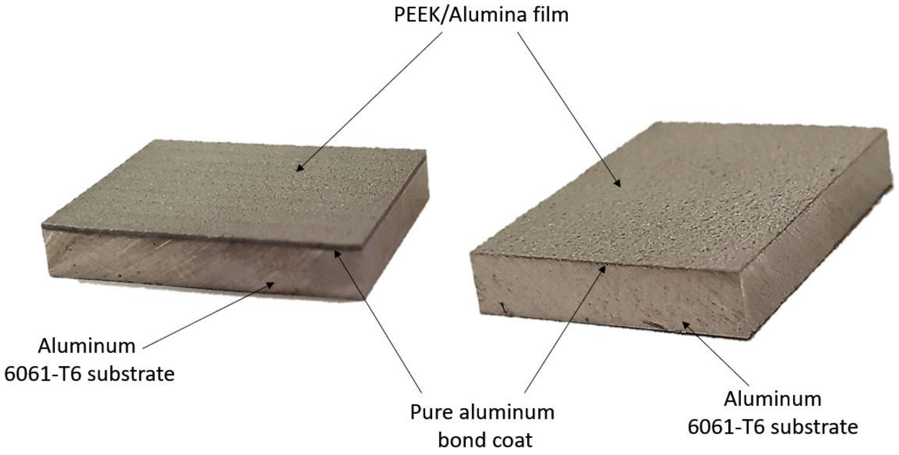

Figure 5.17. Final design of the bottom electrode (aluminum 6061-T6 substrate + pure aluminum bond coat) and diffusive medium (PEEK – 50 %wt. alumina) of the MEET devices.

The PEEK – 50 %wt. alumina film used for the diffusion experiments had a thickness of ~120 µm.

5.2 MEET Device Testing

Following the successful deposition of PEEK – 50 %wt. alumina films on aluminum 6061-T6 substrates, the next objective of this work consisted of investigating the MEET potential of the manufactured devices.

In order to assess the electrical properties of the manufactured MEET device, diffusion experiments were designed. A few considerations were taken in evaluating the diffusive performance of the PEEK – 50 %wt. alumina film.

5.2.1 Choice of the Top Electrode

The first consideration was that the top and bottom electrodes that are in direct contact with the PEEK – 50 %wt. alumina films must be made of the same material. PEEK absorbs water and can therefore result in galvanic corrosion between the top and bottom electrodes if they are made of dissimilar materials [67], [162]. Interestingly, the U.S. Army Missile Command published a study that demonstrated that galvanic corrosion can not only occur between dissimilar materials, but also between different alloys of the same material [162]. Therefore, it is crucial that the top and bottom electrodes of the MEET device are made of the same material.

To ensure that the positive and negative leads of the MEET device are not generating a voltage as a consequence of galvanic corrosion, the negative lead was made by CGDS. It was produced by spraying a pure aluminum coating on an aluminum 6061-T6 substrate following the parameters presented in **Table 5.8**. Essentially, the top electrode (negative lead) shown in **Figure 5.18** has the same layered structure as the bottom electrode (positive lead) with the exception that the latter has a PEEK – 50 %wt. alumina film covering it.

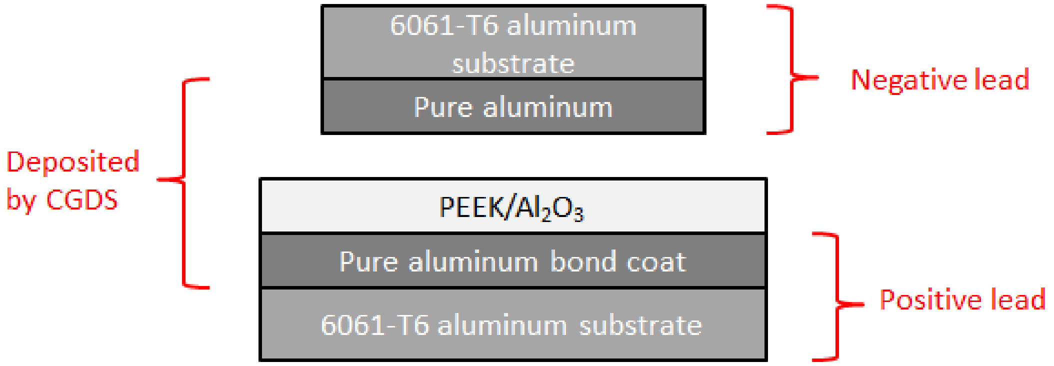

Figure 5.18. Schematic of the final design of the MEET devices produced by CGDS.

The surface roughness of the pure aluminum coating and the PEEK/Al_2O_3 films is beneficial in the diffusion of water through the thickness of the PEEK – 50 %wt. alumina. This roughness leaves micro-gaps between the negative lead and the polymeric film, allowing water to infiltrate them. Additionally, the metal surface of the top electrode has higher surface energy than the PEEK – 50 %wt. alumina film and therefore, assists with drawing and diffusing water from the peripheral region towards the centre [163]. With this design, the wetted area is increased and the PEEK – 50 %wt. alumina underneath the negative lead is more easily hydrated as shown in **Figure 5.19**.

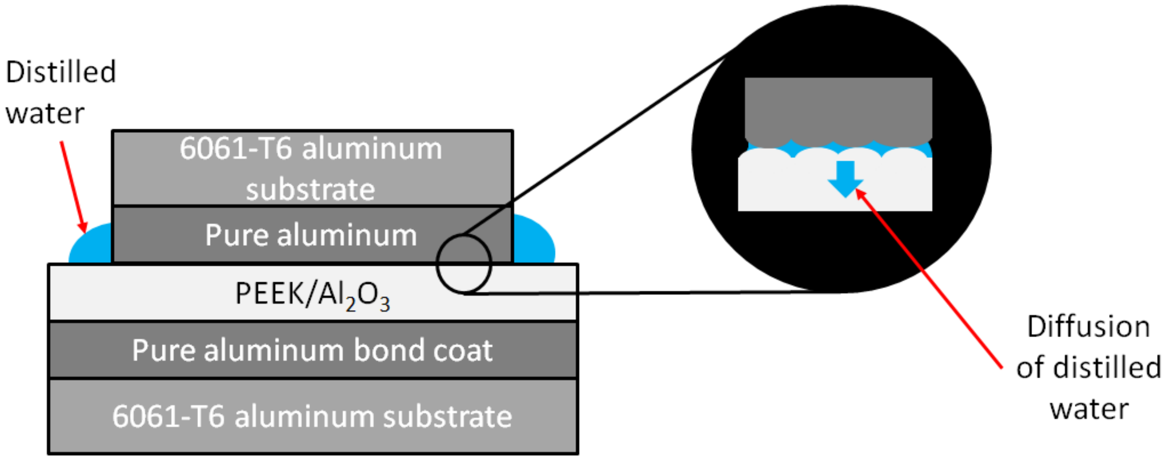

Figure 5.19. Schematic of a MEET device composed of an aluminum 6061-T6 substrate, pure aluminum bond coat and a PEEK – 50 %wt. alumina for the bottom half, and an aluminum 6061-T6 substrate and a pure aluminum coat for the top electrode.

Using aluminum tape or depositing a layer of pure aluminum on top of the PEEK – 50 %wt. alumina film via CGDS would restrict the flow of water in the PEEK/alumina region that is directly underneath the top electrode as illustrated in the schematic in **Figure 5.20**, which would result in a decrease in the performance of the device.

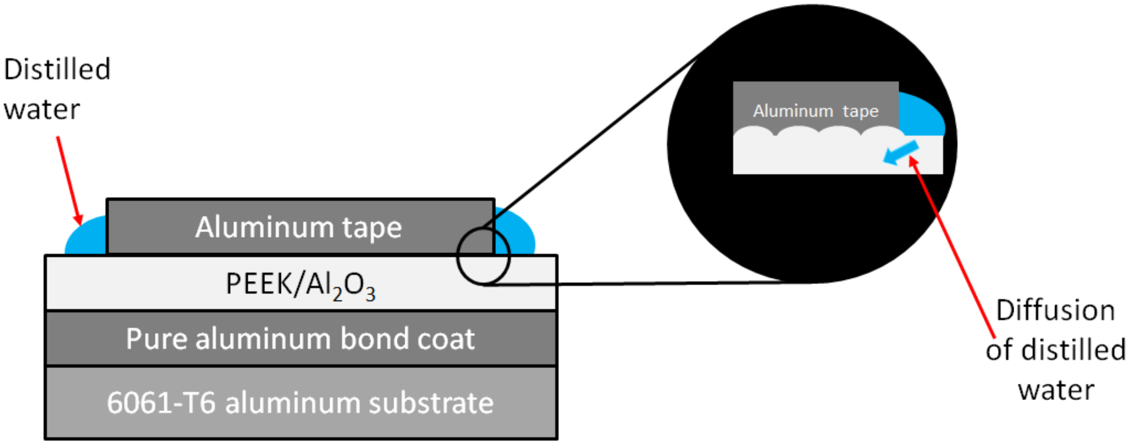

Figure 5.20. Schematic of a MEET device composed of an aluminum 6061-T6 substrate, pure aluminum bond coat and a PEEK – 50 %wt. alumina for the bottom half, and an aluminum tape top electrode.

5.2.2 Diffusion Experiments

Another important consideration when conducting diffusion experiments is the use of distilled water, in order to minimize the amount of foreign electrolytes and impurities in general. These impurities can cause discrepancies between the different testing scenarios if they are not present in water in the same concentrations for each test, which can lead to voltage readings that are not solely a product of diffusion.

Moreover, it is crucial to ensure that the water droplets are contained within the surface of the PEEK – 50 %; if water leaks through the sides, diffusion is hindered, and the output voltages do not reflect the actual efficiency of the diffusion process. **Figure 5.21** presents a schematic of the diffusion experiments.

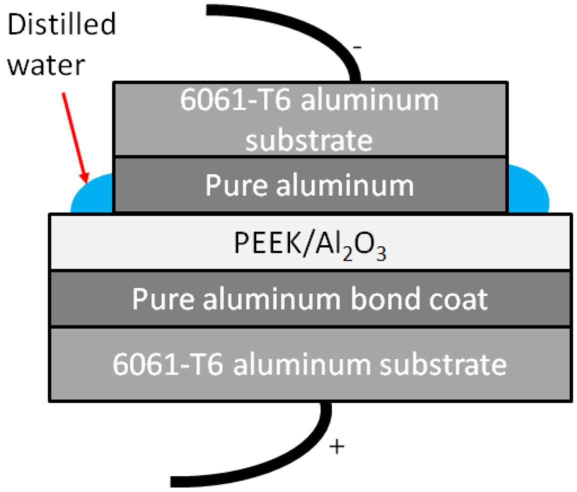

Figure 5.21. Schematic of the diffusion experiment conducted with the manufactured MEET device.

In order to test the manufactured MEET device, multiple hydration scenarios were planned. The aim of conducting multiple testing scenarios was to ensure that the device operated under more than one set of conditions and was therefore ready for implementation in the environment. Moreover, in an attempt to understand the underlying mechanisms and physics of hydration and power generation, it was deemed appropriate to vary the wetting conditions of the device. Although the computation of statistically significant figures like averages and standard deviations is crucial for the development of PEEK-based MEET devices, the primary focus of this work is to demonstrate the proof of concept.

The hydration scenarios are presented in **Table 5.10** that follows. The relative humidity of the room was monitored for all experiments and was in the range of 40 to 60 % at a constant ambient temperature of 23°C.

Table 5.10. Hydration configurations chosen for the diffusion experiments.

Experiment	Schematic	Label of the experiment
Two water droplets in contact with the top electrode	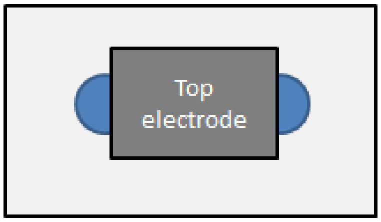	2 Droplets – Direct Contact
Two water droplets away from the electrode (~5 mm between the electrode's side and the closest point on the water droplet's circumference)	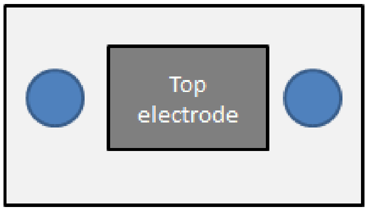	2 Droplets – Away
Six water droplets away from the electrode (~5 mm between the electrode's side and the closest point on the water droplet's circumference)	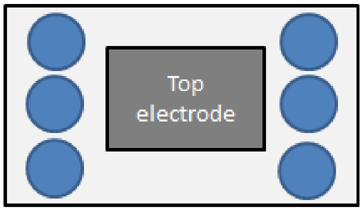	6 Droplets – Away
Multiple water droplets that are not in contact with the electrode	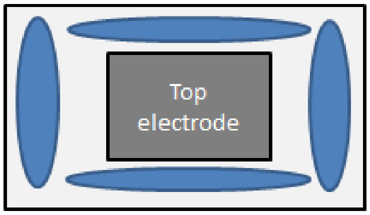	Multiple Droplets – Away
Two water droplets in contact with the top electrode and multiple water droplets not in contact with the electrode	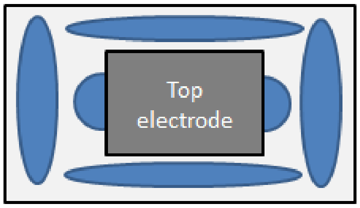	2 Droplets – Direct Contact + Multiple Droplets – Away
Full coverage of the PEEK – 50 %wt. alumina film with water	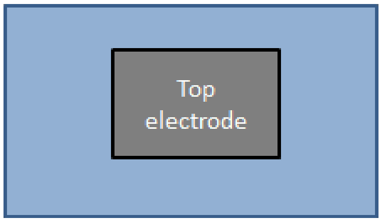	Flooded

5.2.2.1 Two Droplets in Direct Contact with the Top Electrode

Figure 5.22 shows the output voltage of the MEET device when the top electrode is in contact with two water droplets of approximately the same size (~ 0.5 mL). It can be seen from the plot that the voltage increases up to 180 mV almost immediately after the addition of the two water droplets. Approximately 11 minutes (0.18 hours) after the start of the experiment, the voltage drops to a local minimum of 68 mV. From 0.18 hours to 1.56 hours, the voltage increases, reaching a maximum value of 136.8 mV. Finally, from 1.56 hours to the end of the experiment, the voltage decreases until it reaches a value of zero after the 3.3 hour mark.

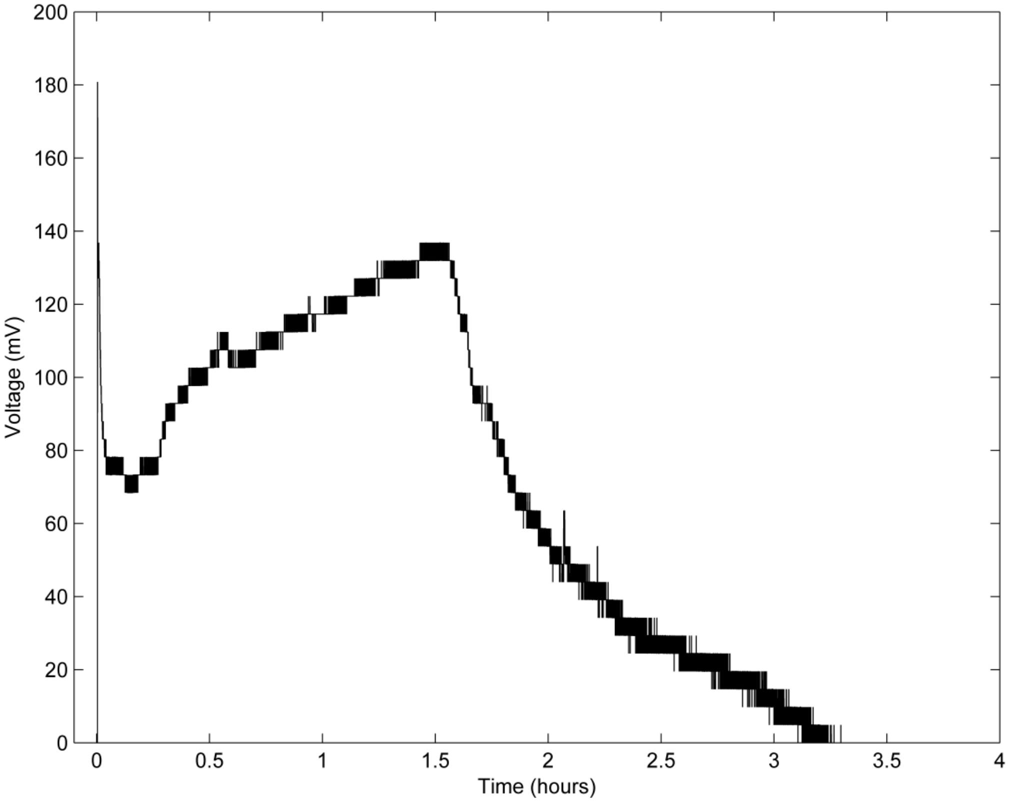

Figure 5.22. Output voltage of the MEET device for the "2 Droplets – Direct Contact" scenario as a function of time.

As previously mentioned in the **Diffusion in Polymer/Ceramic Composites** section, there are two diffusion processes in polymer composites. **Figure 5.23** shows these two diffusion processes: diffusion through the polymer matrix (which is a slow process), and diffusion through the micro-voids (which is a fast process).

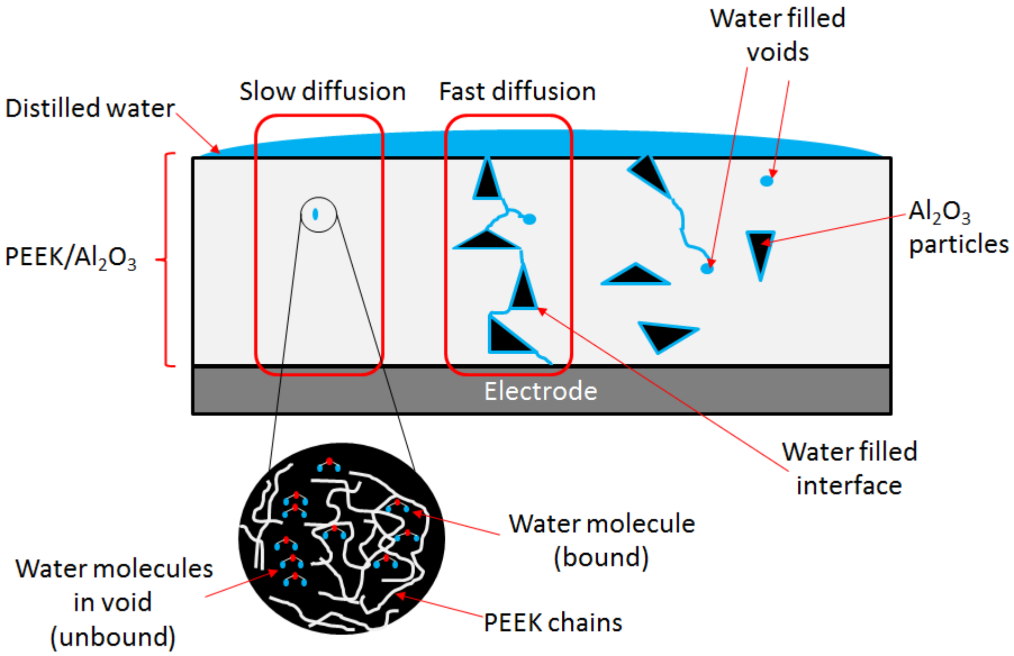

Figure 5.23. Schematic of the absorption mechanisms in the PEEK – 50% wt. alumina film.

The rapid increase and decrease in voltage observed in the early stages of the experiment (**Figure 5.22**) are thought to be due to the fast absorption kinetics of polymer composites. Diffusion in voids is a quick process that results in a sharp output voltage, but because the voids get filled with water rapidly, this diffusion mechanism comes to a halt soon after its start, and the voltage drops in a short period of time. This diffusion process is believed to be Fickian as previously explained in the **Diffusion in Polymer/Ceramic Composites** section [89] [90].

Once the voids have been filled with water, the diffusion mechanism is slowed down as it is limited by the kinetics of diffusion in the polymer matrix. This diffusion process occurs through the amorphous regions of the PEEK and the free volume between them. Water molecules react with the polar ketone group of the PEEK molecule, resulting in the relaxation of the polymer chains and swelling. More water uptake ensues, resulting in higher output voltages (from 0.18 hours to 1.56 hours). This secondary diffusion mechanism is believed to be non-Fickian [22], [23], [84], [85], [87], [89], [91].

The decreasing voltage from 1.56 hours to the end of the experiment is due to the combination of water absorption in the PEEK – 50 %wt. alumina film and evaporation to the room (and not saturation) as the non-Fickian diffusion mechanism takes up to several months to reach saturation [22]–[24], [87].

5.2.2.2 Two Droplets Away from the Electrode

Figure 5.24 shows the response of the MEET device when exposed to two water droplets that are not in direct contact with the top electrode. The output voltage of the device is zero for roughly 20 minutes (0.36 hours), point at which it sharply increases to 244.4 mV. At the 24-minute mark (0.40 hours), thus only 4 minutes after the maximum peak voltage, the voltage has essentially dropped to zero, with slight oscillations close to 0 mV.

Interestingly, it can be seen from the plot that there is a slight increase in voltage between 1 hour and 2 hours, with a maximum recorded value of 19.55 mV.

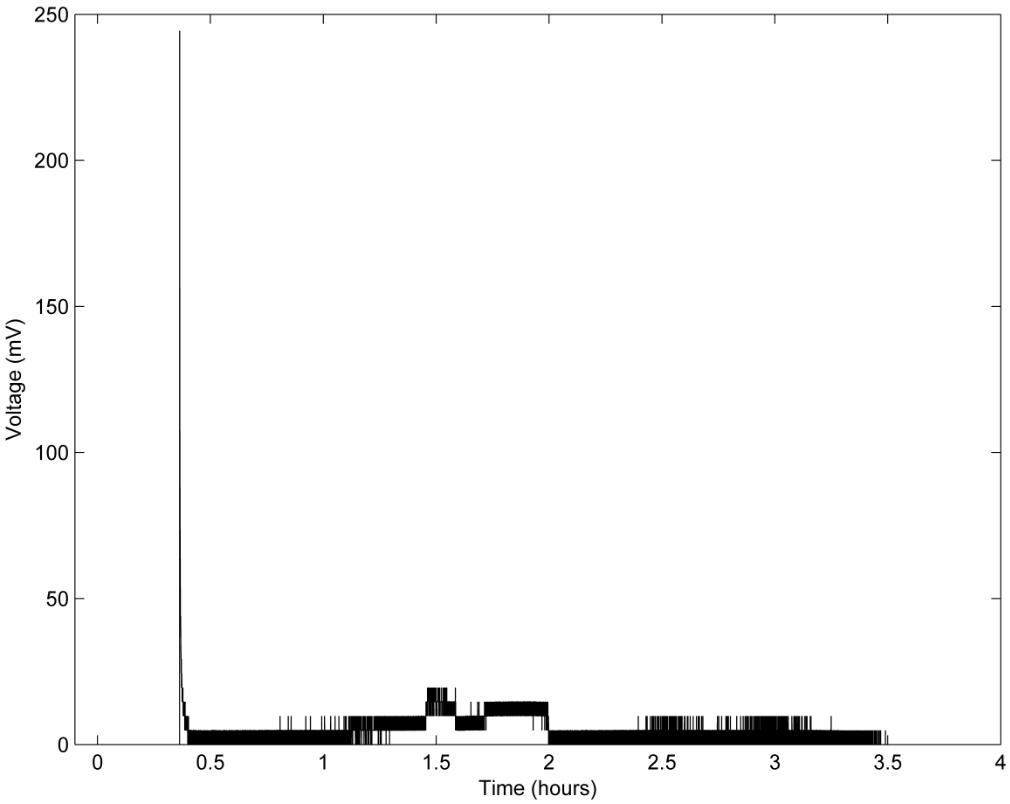

Figure 5.24. Output voltage of the MEET device for the "2 Droplets – Away" scenario as a function of time.

The voltage is nil for the first 20 minutes because the two water droplets have not spread from their initial location to the top electrode to allow current to be collected. PEEK has low surface energy and is consequently hydrophobic in nature [163], [164]. Nevertheless, because of surface modifications introduced by alumina particles in the CGDS process as well as the voids between the alumina particles and the PEEK matrix, wettability is increased [164], [165]. Hence, the water droplets slowly spread onto the surface, moving inwards towards the electrode as shown in the schematic in **Figure 5.25.**

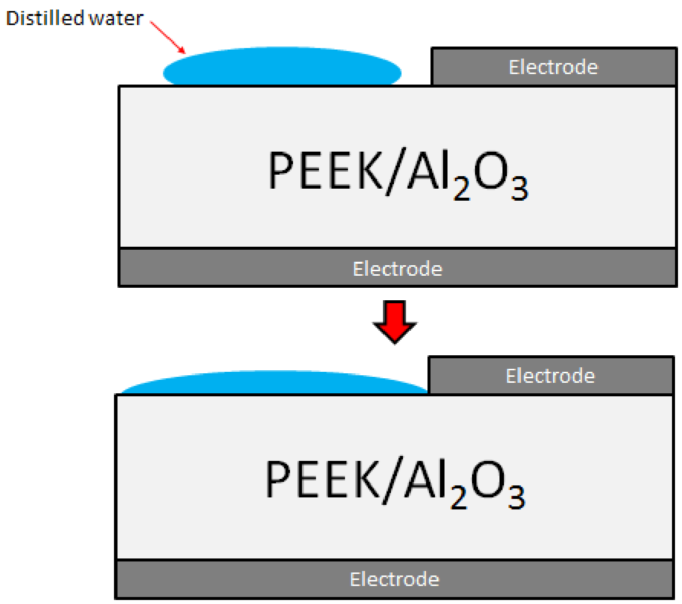

Figure 5.25. Surface wetting of the PEEK – 50 %wt. alumina film.

When the water comes in contact with the top electrode, the voltage increases to 244.4 mV but it quickly drops back to zero: it is seen in **Figure 5.22** (**Two Droplets in Direct Contact with the Top Electrode** scenario) that after 20 minutes (~ 0.33 hours), the secondary (slower) diffusion mechanism has started. Hence, in this scenario, when the water droplets come in contact with the top electrode through surface wetting, both diffusion mechanisms (PEEK matrix diffusion and void diffusion) are underway, which may explain why the peak voltage for this scenario (244.4 mV) is higher than the peak voltage for the **Two Droplets in Direct Contact with the Top Electrode** scenario, for which it is hypothesized that only the Fickian diffusion mechanism is underway at 0.18 hours. Moreover, given the fact that water spreads to the top electrode after 20 minutes, the wetted area at the time of contact of the water droplet with the electrode is larger than for the previous scenario.

It is worth noting that because of the increased wetting area for the same amount of water as the **Two Droplets in Direct Contact with the Top Electrode** scenario, drying occurred earlier and resulted in lower voltages overall.

5.2.2.3 Six Droplets Away from the Electrode

Figure 5.26 displays the output voltage of a MEET device exposed to 6 droplets of water that are not initially in direct contact with the top electrode. The output voltage is essentially zero for the first 1.4 hours, with small oscillations at 4.89 mV. Between 1.4 hours and 2 hours, the output voltage appears to be increasing, and between 2 hours and approximately 3 hours, the voltage appears to reach a plateau at about 50 mV. Voltage oscillations range from 39.1 mV to a maximum of 97.75 mV, showing a skew towards the higher values. After the 3 hour mark, the output voltage follows a decreasing trend overall, with occasional voltage surges, and reaches a value of zero after 4.3 hours.

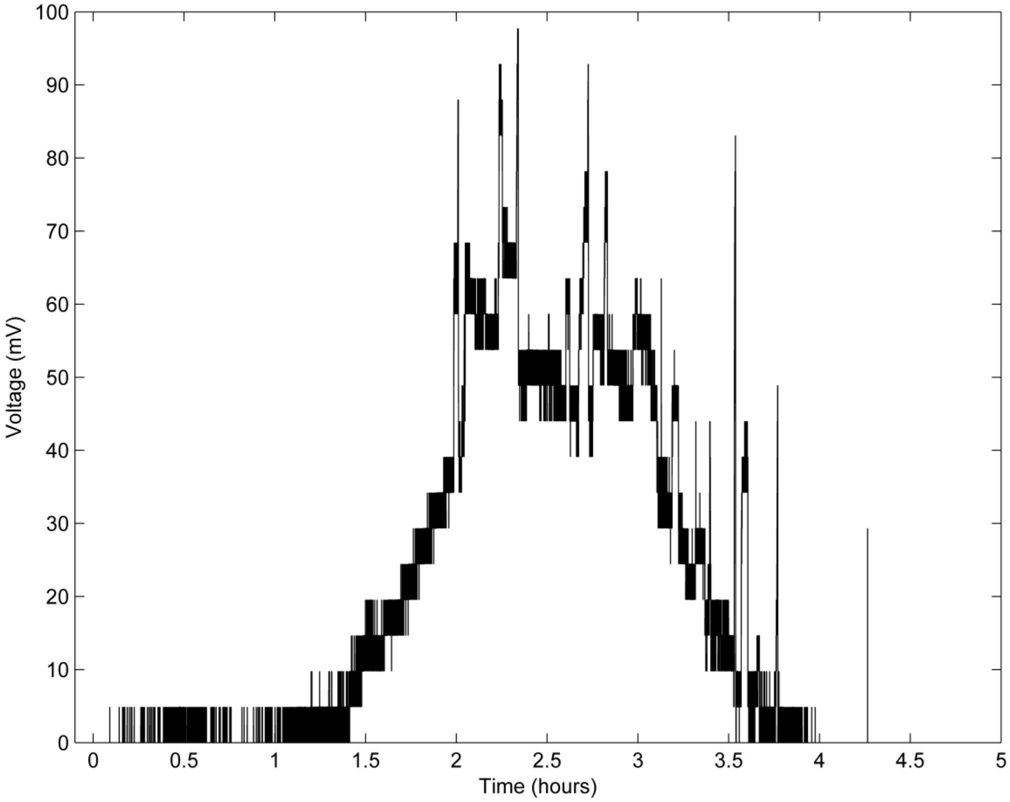

Figure 5.26. Output voltage of the MEET device for the “6 Droplets – Away” scenario as a function of time.

The 6 droplets diffused towards the outside more than they did towards the inside, moving mainly towards the edges as shown in **Figure 5.27.**

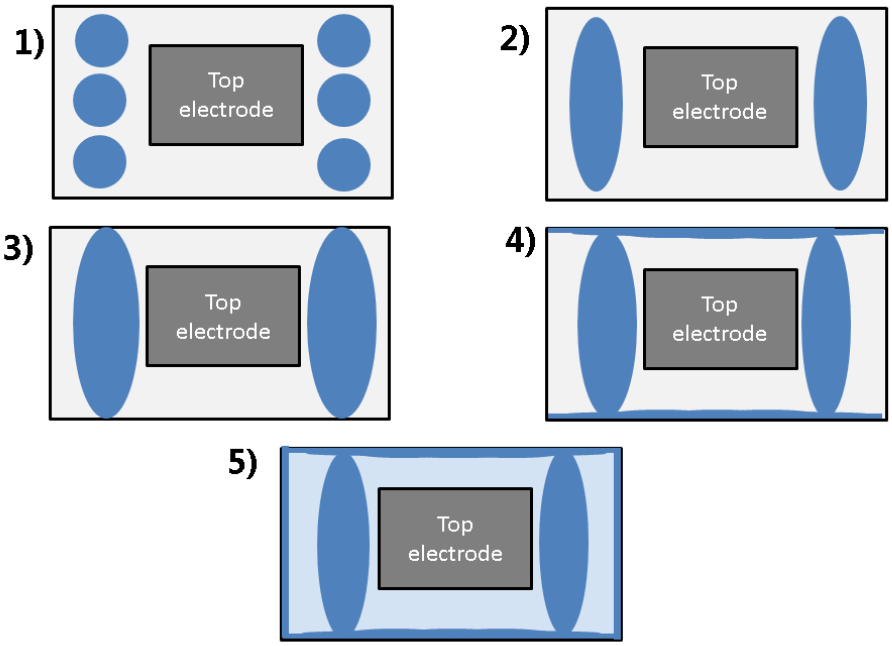

Figure 5.27. Schematic of the combination of the water droplets onto the PEEK – 50 %wt. alumina film (chronologically numbered from 1 to 5) and their diffusion along the edges of the MEET device.

This surface wetting behaviour was attributed to the fact that the three water droplets on each side of the electrode coalesced while spreading onto the surface of the device. Once the water droplets came into contact with the sides of the device, they got drawn towards its edges because of their high surface energy [166]. This did not happen in the previous scenario (**Two Droplets Away from the Electrode**) because there were fewer water droplets, and those were more central. Consequently, absorption and evaporation to the room brought the experiment to an end before the wetting could reach the sides of the device.

The surface wetting behaviour of the six droplets resulted in a more gradual wetting of the PEEK – 50 %wt. alumina film, from the edges of the MEET device towards the top electrode in the centre. Thus, the voltage essentially oscillated around zero for the first 1.4 hours following hydration. Once the film absorbed water and moisture came into contact with the top electrode, the output voltage of the device increased, plateaued and eventually dropped back to nil after 4.3 hours following drying. The absence of an initial voltage peak as seen in the **Two Droplets in Direct Contact with the Top Electrode** and **Two Droplets Away from**

the Electrode scenarios is due to the fact that the water droplets diffused towards the electrode not because of surface wetting, but rather in depth water absorption. When moisture got to the top electrode, after 1.4 hours, the generated voltage was mainly a result of diffusion through the PEEK matrix, following the non-Fickian diffusion model. As previously shown in **Figure 5.22** and **Figure 5.24**, after 1.4 hours, the void filling Fickian diffusion mechanism is no longer the predominant one as no sharp voltage peaks are recorded. Once again, the voltage dropped back to zero because of a combination of water absorption and evaporation to the room, and not saturation. The voltage oscillations observed in the decreasing part of output are thought to be the result of a local diffusion phenomenon that occurs during drying, where there could possibly be local sites that are still undergoing void filling diffusion. This mechanism is possibly triggered by the voids left by evaporating water molecules and requires further investigation.

5.2.2.4 Multiple Droplets Away from the Electrode

Figure 5.28 shows the output of the MEET device when multiple droplets are placed on the PEEK – 50 %wt. alumina film, away from the top electrode. Soon after the addition of the water droplets, the voltage peaks at 24.44 mV but drops to zero after approximately 20 seconds. The voltage remains at zero up until 1.08 hours, when two voltage peaks appear: 78.2 mV at 1.08 hour and 68.43 mV at 1.27 hours. The voltage drops to zero at 1.18 hours, between these two local peaks. The voltage also drops back to zero past the 1.34 hour mark, until 1.56 hours: the output voltage essentially increases until it reaches a maximum value of 200.4 mV at 7.92 hours. After 7.92 hours, the voltage decreases until it reaches a value of zero at about 13.7 hours. The voltage remains above 100 mV for more than 5 hours.

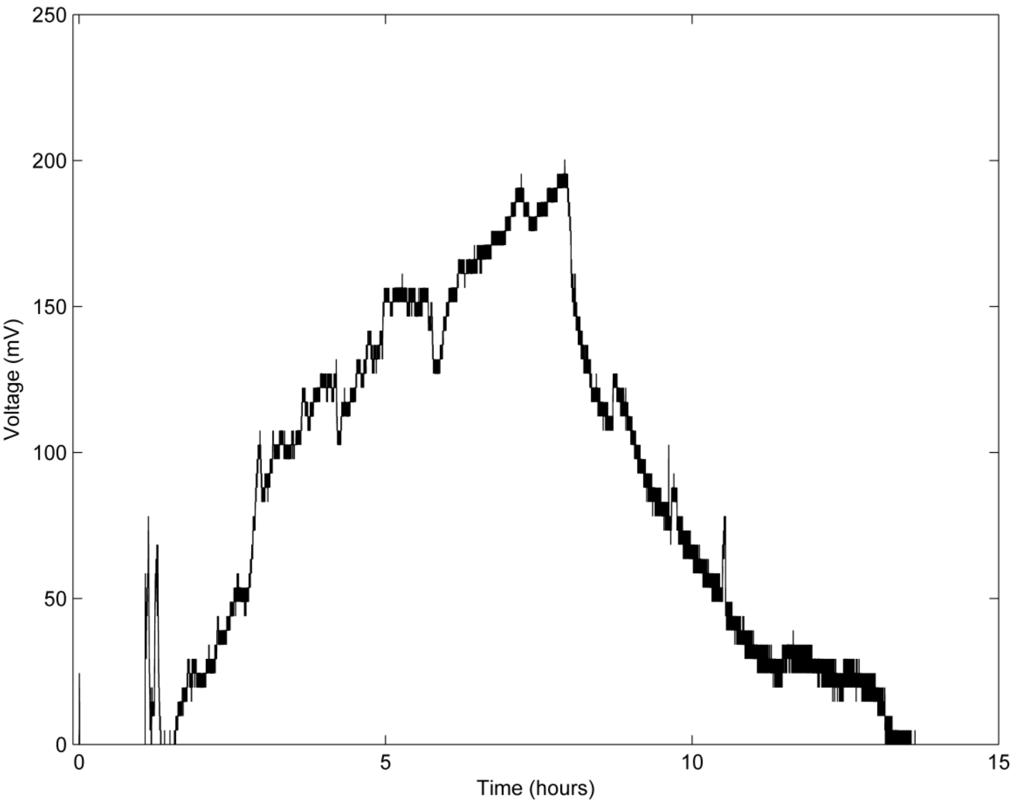

Figure 5.28. Output voltage of the MEET device for the “Multiple Droplets – Away” scenario as a function of time.

The peak voltages recorded at 20 seconds, 1.08 hours and 1.27 hours are attributed to the Fickian void filling diffusion mechanism as water spread onto the surface of the PEEK – 50 %wt. alumina film and came into contact with the top electrode. Similarly to the **Six Droplets Away from the Electrode** scenario, the water droplets spread towards the outside (sides) of the MEET device despite the fact that this time, because of the larger amount of water, the water reached the top electrode while the Fickian diffusion mechanism was still underway (20 seconds, 1.08 hours and 1.27 hours) and was therefore captured. The peaks are brief and resemble those observed in **Figure 5.22** and **Figure 5.24**. On the other hand, the voltage increase after 1.56 hours is mainly attributed to the slow, non-Fickian diffusion inside the pure PEEK matrix. It is notable that the voltage output spanned over about 13 hours, which is substantially longer than the previous hydration scenarios, because of the higher amount of water used in the experiment. The voltage dropped back to zero after 13.7 hours because of the evaporation of water to the room and not saturation.

5.2.2.5 Two Droplets in Direct Contact with Top Electrode & Multiple Droplets Away

Figure 5.29 shows the output voltage of a MEET device when two droplets of water are in direct contact with the top electrode, and multiple water droplets are placed in the periphery of the electrode. Soon after water droplets are put in contact with the top electrode (54 seconds), the voltage surges to 112.4 mV. The voltage drops back to zero after approximately 6 minutes until a second peak is observed at time 0.78 hours where the output voltage reaches a value of 97.75 mV. Subsequently, the output voltage essentially decreases, with some slight oscillations, down to a value of 24.44 mV at time 1.68 hours.

Following this trough, the voltage increases up to a value of 175.9 mV at time 15.47 hours. From 15.47 hours to the end of the experiment, the voltage decreases.

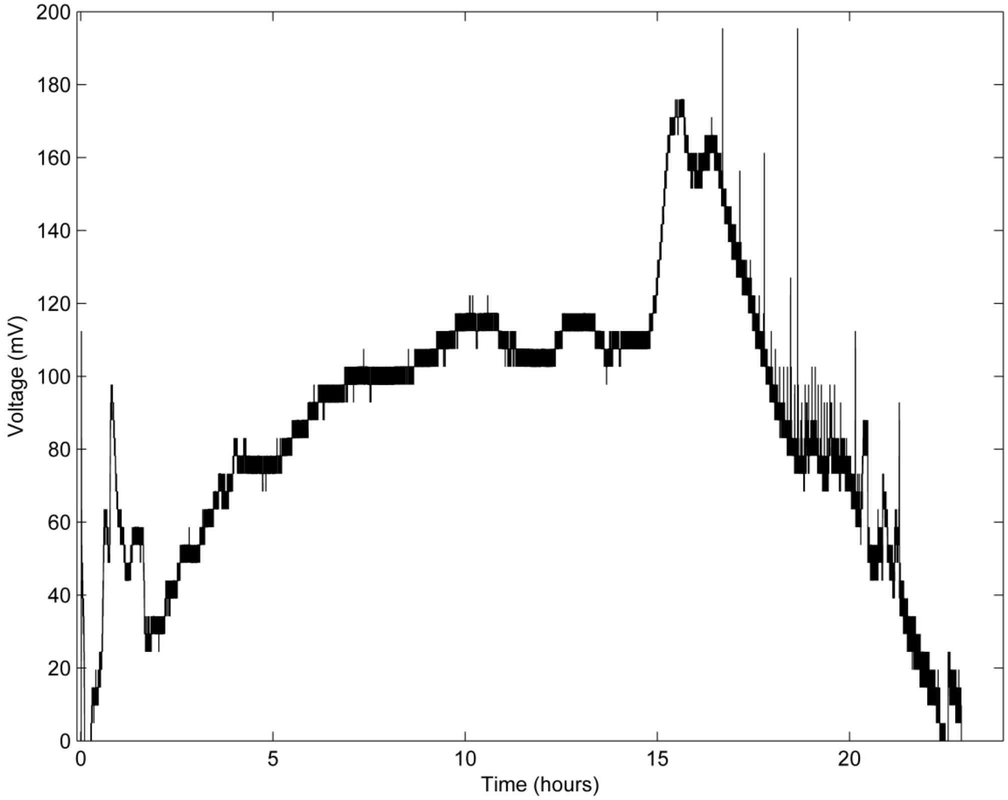

Figure 5.29. Output voltage of the MEET device for the "2 Droplets – Direct Contact + Multiple Droplets - Away" scenario as a function of time.

It is worth noting that there appears to be an abrupt change in slope in the voltage at ~ 15 hours. It was experimentally observed that this change occurs when water droplets are no longer visible on the PEEK – 50 %wt. alumina film, due to a combination of evaporation to the room and water absorption by the MEET device. A potential explanation to this change in slope could be that, at 15 hours, an optimal ratio between the number of H_2O molecules and H^+ ions was reached. In other words, there was enough water absorbed by the PEEK – 50 %wt. alumina film to produce a large number of H^+ ions and because of the decreasing number of H_2O molecules (solvent) due to evaporation to the room, the concentration of the ions increased, resulting in a higher output voltage.

After this peak, the voltage decreases overall because of the recombination of the H^+ ions and the negatively charged oxygens in the PEEK molecules. This decreasing trend however, has marked oscillations: in fact, the highest recorded voltage occurs during this decreasing voltage phase, where two peaks are observed at 195.5 mV (this behaviour is observed in the **Six Droplets Away from the Electrode** scenario and its causes briefly hypothesized).

With the addition of more water compared to the previous scenarios, the device generated electricity for approximately 23 hours. Once again, the output voltage dropped to zero because of the evaporation of water.

The initial voltage surge is again attributed to micro-void Fickian diffusion resulting from the diffusion of the water droplets that are in direct contact with the top electrode, following a similar trend as the one observed in **Figure 5.22**. The subsequent voltage peak at 0.79 hours is also attributed to this same micro-void diffusion: the droplets from the periphery spread towards the centre, on the surface of the PEEK – 50 %wt. alumina film. This surface wetting occurs early enough, before the Fickian part of the diffusion reaches equilibrium, to be captured by the output voltage of the device, unlike in the **Six Droplets Away from the Electrode** scenario.

5.2.2.6 Flooded MEET Device

Figure 5.30 shows the output of the “Flooded” watering scenario, where the whole surface of the MEET device is covered in water. This testing case is the most general one. In fact, the experiment intended to visualize the output voltage of the MEET device when exposed to water droplets added at different intervals, to assess the stability of the output voltage over an extended period of time.

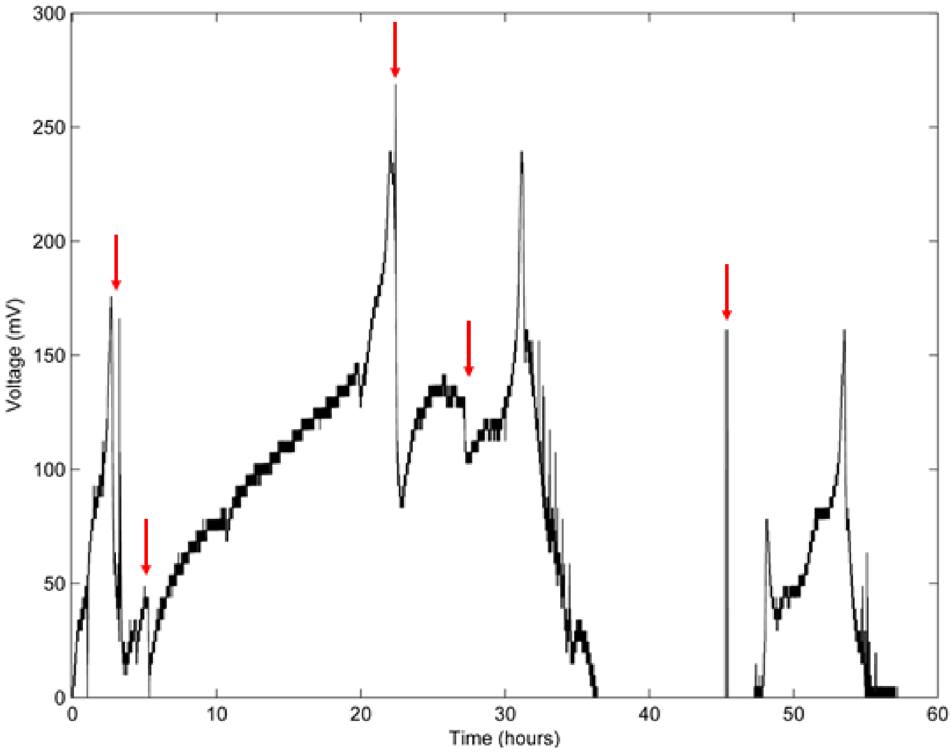

Figure 5.30. Output voltage of the MEET device for the "Flooded" scenario as a function of time. The arrows indicate the addition of more water to the device.

To ensure that the whole surface of the MEET device is wetted adequately, water droplets were deposited onto it prior to the experiment. In other words, the top electrode was removed and the entire surface of the MEET device was pre-wetted for an hour. Consequently, as seen in **Figure 5.31**, there is no sharp increase in voltage during the first few minutes following the start of the experiment, due to the void filling mechanism (Fickian diffusion) taking place during the pre-wetting phase, which preceded data acquisition.

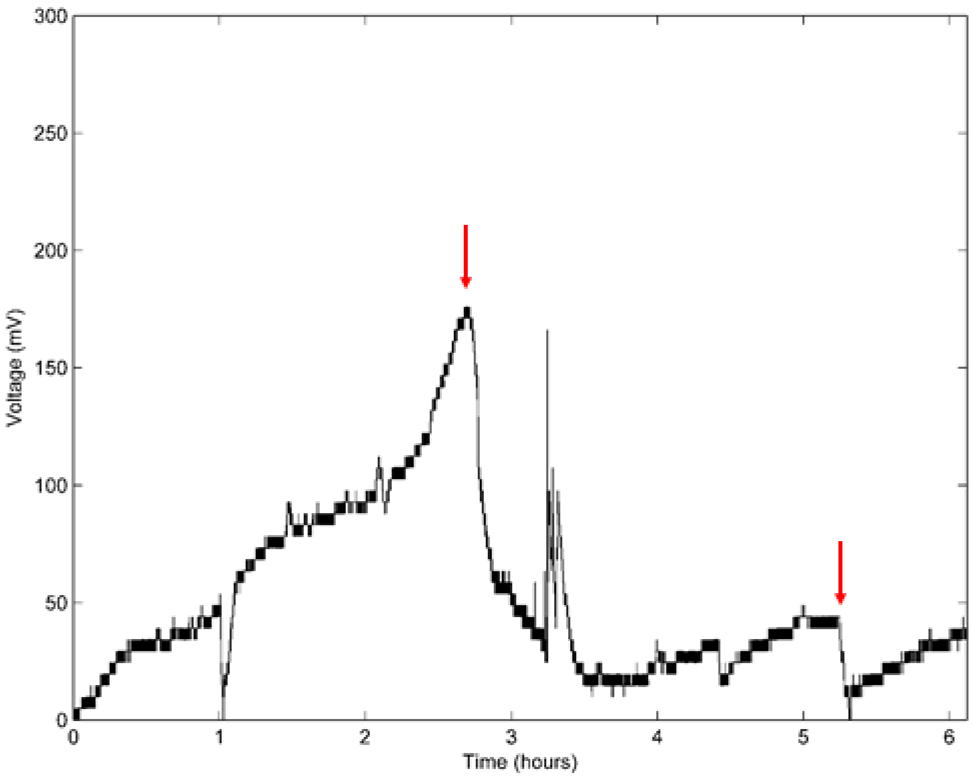

Figure 5.31. Output voltage of the MEET device for the "Flooded" scenario as a function of time, shown between time = 0 and time = 6 hours. The arrows indicate the addition of more water to the device.

The voltage drops to 0 mV at 1.03 hour and 5.32 hours because the water rose above the sides of the top electrode and came into contact with the wire that connects to it, resulting in a reverse voltage. The wires used to connect the electrodes are tinned copper wires: tin is more noble than aluminum and therefore, if both materials are submerged in a solution, an electrochemical cell is formed with a positive tin and a negative aluminum lead [67]. **Figure 5.32** shows a schematic of the electrochemical cell.

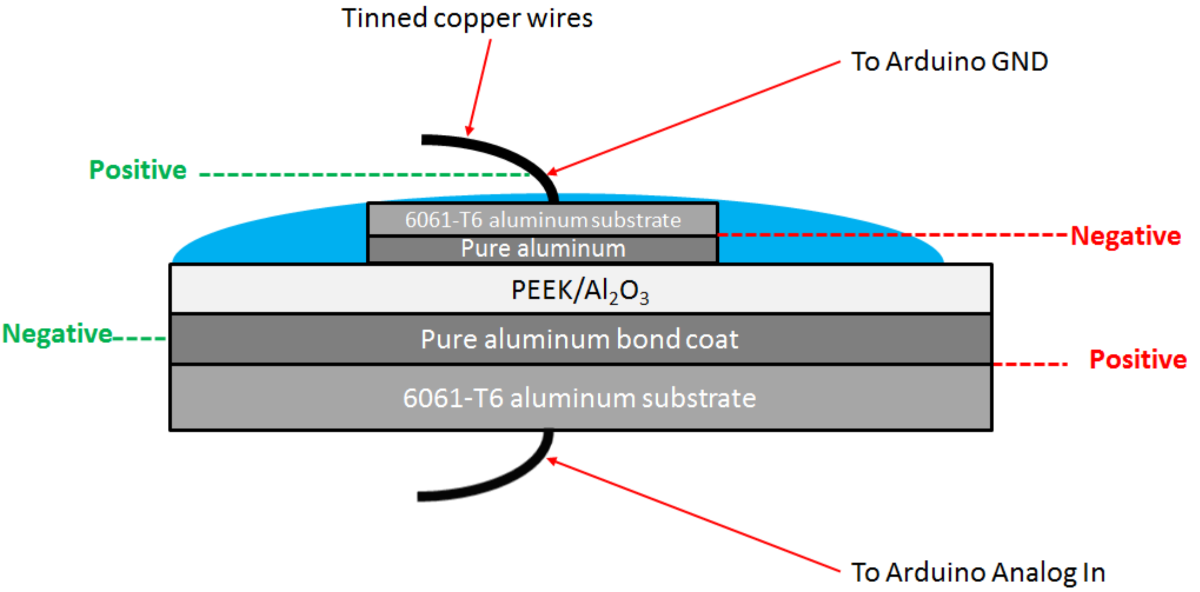

Figure 5.32. Schematic illustrating the expected polarity (in red) and the tin-aluminum electrochemical cell system (in green) formed because of water leakage.

Because the Analog In Arduino pins can only sample positive voltages, this polarity reversal goes undetected and instead, 0 mV is shown. Immediately after this voltage reversal was noticed and confirmed using a multimeter, a piece of tissue was used to pull some water off the top of the PEEK – 50 %wt. alumina film via capillary action, to reduce the water level to below the top surface of the top electrode. From **Figure 5.31**, it appears that the trend of the output voltage resumes normally after water removal, as no change of slope takes place.

The main observation made in this experiment is that the addition of water "disrupts" the output voltage. Before the 40 hour mark, and excluding the initial wetting at time zero, water was added to the device 4 times as shown by the arrows in **Figure 5.30.** It is apparent that, each time water was added to the device, the output voltage dropped. A potential explanation to this phenomenon could be that, with the addition of water, the concentration of H^+ ions decreased given the larger amount of solvent. The rapid decrease in voltage is attributed to the water infiltrating the voids (Fickian diffusion). When the voltage reached a local maximum (2.7 hours, 175.9 mV), (22.4 hours, 268.8 mV) and (31.18 hours, 239.5 mV), the water appeared to mostly have dried or been absorbed by the PEEK – 50% alumina film. The 4.985

hours, 48.88 mV peak is not considered here because of the water-leakage that caused polarity reversal (**Figure 5.32**). Once again, a change of slope is observed at these peak voltages (clearly seen in **Figure 5.30**) and is once again attributed to the increasing concentration of H^+ ions because of the decreasing number of solvent molecules (H_2O).

The PEEK – 50 %wt. alumina film was left to dry between 36.35 hours and 45.25 hours, after which water was added to the film to cover the whole surface. This time however, the top electrode was not removed to pre-wet the whole surface but rather, water was simply added in the periphery of the device. The flooding of the top surface ensured that water came into contact with the top electrode. **Figure 5.33** shows the output of the device following its hydration.

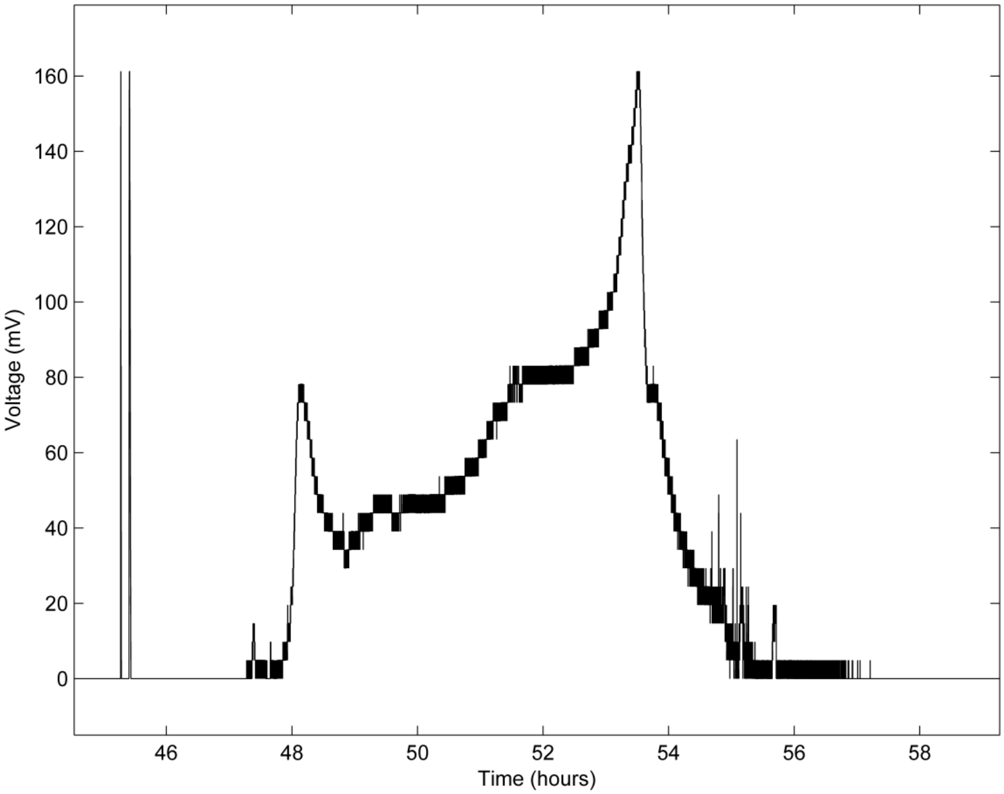

Figure 5.33. Voltage output of the MEET device after drying for approximately 9 hours then hydrated at 45.27 hours.

The behaviour observed in this experiment is similar to the **Two Droplets in Direct Contact with Top Electrode & Multiple Droplets Away** scenario shown in **Figure 5.29**. It is notable that there is, however, a longer delay between the two initial voltage peaks at times 45.27 hours and 45.41 hours (void filling diffusion mechanism) and the more gradual voltage increase which starts at 47.29 hours (free volume diffusion in the PEEK matrix). This delay was also observed in **Figure 5.28** for the **Multiple Droplets Away from the Electrode** scenario. In this scenario, the delay can be attributed to the fact that, because the whole surface is wetted, the void filling mechanism is underway early for the entirety of the device. Because the water is in contact with the top electrode from the start, the output voltage resulting from the void filling mechanism is captured. Once the void filling diffusion mechanism has come to a halt, there is a delay until the diffusion in the PEEK matrix starts (non-Fickian diffusion) at ~ 48 hours.

5.2.3 MEET Device in Numbers

Following the diffusion experiments, from the **Flooded MEET Device** scenario, calculations of the maximum output power and the maximum output current were done, following ohm's law (**equation (4.1)**). These two numbers were subsequently divided by the area of the device (66 mm by 34 mm) to compute respectively the power per unit area and the current density. **Table 5.11** sums up the principle figures of the manufactured MEET device and other numbers reported by authors in the literature.

Table 5.11. Reported numbers for MEET devices.

Authors	Maximum power density or power	Maximum output voltage	Maximum current density or current	Activation source	Size	Time to saturation / Longest cycle	Manufacturing process
This work	10.63 nW (4.736 μW/m^2)	268 mV	39.53 nA (17.62 μA/m^2)	Liquid water	66 mm by 34 mm	+ 30 hours	CGDS
Zhao *et al.* [13]	4.2 mW/m^2	30 mV	5.5 μA/cm^2	Breathing	0.5 cm by 0.5 cm	5 sec	Aqueous suspension + Moisture-Electric Annealing
Liang *et al.* [60]		0.7 V	0.2 μA	Moist air	0.8 mm^2	450 s	Solvent evaporation
Cheng *et al.* [14]		70 mV	12 mA/cm^2	Touch proximity		Less than 30 secs	Filtration of dispersion + laser patterning + Moisture-Electric Annealing
Zhao *et al.* [16]		40 mV	0.3 mA/cm^2	RH change		Less than 1 s	Oxidizing reaction + longitudinal unzipping + dimensionally confined freezing
Cheng *et al.* [62]	4.2 mW/m^2	260 mV		RH change		Less than 10 s	Aqueous dispersion + freeze-drying + heteroatoms doping
Zhao *et al.* [17]	1 mW/cm^2	260 mV	3.2 mA/cm^2	RH change		Less than 10 s	Chemical solution + freeze-drying + Moisture-Electric Annealing
Huang *et al.* [15]	1.86 mW/cm^2	270 mV	24 mA/cm^2	RH change		Less than 10 s	Chemical solution + Moisture-Electric Annealing

Table 5.11 (continued)

Authors	Maximum power density or power	Maximum output voltage	Maximum current density or current	Activation source	Size	Time to saturation / Longest cycle	Manufacturing process
Liu *et al.* [18]	0.7 mW/m^2		6.2 μA/cm^2	Breathing		400 s	Chemical solution + hierarchical soaking
Shen *et al.* [19]	4 μW/cm^2	520 mV	8 μA/cm^2	RH change, breathing	1.2 cm by 1.2 cm	Less than 400 s	Chemical solution + electrophoretic deposition + Moisture-Electric Annealing
Xue *et al.* [63]	6.9 mW/m^2	60 mV	10 μA/cm^2	RH change, breathing	1.3 cm^2	Less than 10 s	Chemical solution + electrochemical polymerization
Xue *et al.* [61]	53 nW	1 V	100-105 nA	Liquid water	1.25 cm by 2.5 cm	+ 160 hours	Ethanol flame carbon collection + heat treatment + plasma treatment

5.2.4 Advantages of PEEK-based MEET Devices Manufactured via CGDS

The figures of the MEET device manufactured in this work show great promise in comparison to other designs. Despite displaying lower power and current densities, it exhibits a significantly longer power generation cycle, which is an important attribute for potentially useful applications.

Realistically, it would be extremely difficult to harvest electrical energy from devices that can only generate a voltage for a few seconds or minutes, given the low power figures reported in **Table 5.11**. It would also be challenging to combine devices that generate power for short time intervals (and that can undergo pole reversal) in series and parallel to increase the output voltage and current, respectively. CGDS-manufactured PEEK-based MEET devices, because of their long power generation cycles as well as the absence of pole reversal (as long as wire connections are properly insulated), can be combined in series and parallel to obtain the desired power output figures.

Another important point to address is that a design that uses water droplets is more advantageous than a design that uses humid gas. For the latter, a forced flow on the device must be maintained for as long as a power output is required, which can be inconvenient in most setups. Moreover, this mode of operation is a line-of-sight one and can be cumbersome if multiple devices are combined in series and parallel. Oppositely, relying on water droplets to generate electrical power makes the configuration of series and parallel combinations more flexible. The wetting process is not a line-of-sight one and MEET devices can be disposed in towers (like the Warka Tower), where the only required condition for their operation is that water comes into contact with them. As a result, the PEEK-based MEET devices produced via CGDS can be stacked in vertical structures, occupying very little open space and having minimal impact on the fauna and the flora.

Finally, an important advantage of these PEEK-based MEET devices is their simple design and manufacturing process. The CGDS process does not require the equipment, the products (chemicals), the measurement precision and the labour force of other chemical approaches. Therefore, the process is suitable for large-scale production and can satisfy a large demand thanks to its throughput (in the order of square meters per minute), near-full automation and ability to produce films on large plates.

6 Conclusions

6.1 Summary of Results

This work explored the AM potential of CGDS in the fabrication of MEET devices. The deposition of pure PEEK on aluminum 6061-T6 was unsuccessful due to thermal mismatch between the two materials. The delaminated PEEK coatings showed good cohesion between the particles as thick buildups formed onto grit-blasted substrates. Nevertheless, adhesion to the substrate was poor due to thermal stresses.

It was subsequently found that depositing an in-situ composite of PEEK and 50 %wt. alumina on a pure aluminum bond coat resulted in successful coating deposition. It was shown that spraying a pure aluminum bond coat on aluminum 6061-T6 substrates resulted in significantly higher surface roughness compared to grit-blasted aluminum 6061-T6 substrates, which mitigated the delamination of PEEK – 50 %wt. alumina films. Moreover, it was determined that substrate preheating, size and insulation were crucial in depositing PEEK – 50 %wt. alumina and ensuring repeatability, as polymers are more sensitive to temperature variations than metals. The optimal spray parameters were also determined to be 350°C and 2.07 MPa for the stagnation conditions. A traverse speed of 100 mm/s combined with a feed rate of 2 and 4 g/min resulted in a PEEK – 50 %wt. alumina film thicknesses of 120 and 300 µm, respectively.

The PEEK – 50 %wt. alumina film did not saturate after continuous exposure to moisture for over 30 hours based on the output voltage. Dual diffusion modes were hypothesized to be the main mechanisms of operation of the manufactured MEET device: diffusion through the voids, which is thought to be a quick Fickian mechanism, and diffusion through the PEEK matrix, which is believed to be a slow non-Fickian mechanism that can result in a long time to saturation and important water uptake.

The maximum output voltage of a 66 mm x 34 mm MEET device with a PEEK – 50 %wt. alumina film thickness of 120 µm was 268 mV with a 6.8 MΩ resistor. The top electrode had dimensions of 27 mm x 17 mm. The maximum output power of the device was calculated to be 10.63 nW (4.736 µW/m^2). Finally, the maximum output current and maximum current density was computed to be 39.53 nA and 17.62 µA/m^2, respectively.

In summary, through this work, CGDS proved to be a simple process for the manufacturing of MEET devices as opposed to the chemical methods used in the literature. Its speed, automation and scalability make it an excellent candidate for the large-scale manufacturing of MEET devices. Additionally, the water absorption properties of the PEEK – 50 %wt. alumina film are suitable for the implementation of these MEET devices in vertical structures (like the Warka Tower, wells or even underground) and to extract power from water with minimal impact on the environment. Therefore, this technology can be extended to remote areas like forests and jungles to power sensors, without affecting the landscape and the wildlife.

Finally, the high melting point of PEEK and its excellent resistance to corrosion make PEEK-based MEET devices a serious alternative to power generation in deserts, where dew can be taken advantage of during nighttime to generate electrical power and therefore complement solar technology.

6.2 Future Work

While the suitability of PEEK as a MEET material was proven and the deposition of PEEK using CGDS achieved, there remains additional work that needs to be undertaken to fully characterize the manufacturing of PEEK-based MEET devices via CGDS, as well as their properties:

1. Determine the most appropriate alumina weight percentage in PEEK using the final setup that includes substrate preheating and insulation from a mechanical and a power generation standpoint. Such information would be crucial in optimizing the process as well as the output power of the manufactured devices.

2. Study the effect of the thickness of the PEEK/Al_2O_3 film on the output voltage of the devices. With this information, both the manufacturing process and the power generation properties would be optimized, as less material and power would be lost.

3. Investigate the size effect of the bottom and top electrode and find the most suitable ratio for optimal power output and wetting of the PEEK/Al_2O_3 film.

4. Combine MEET devices in series and in parallel to assess their power generation properties in different configurations. This would result in higher output voltages and currents, which can be used to power useful devices.

5. Conduct experiments that are solely focused on studying diffusion in PEEK or PEEK/Al_2O_3 films and correlate the water absorption properties with the output voltages generated by the devices.

6. Study and isolate the effect of alumina particles on the water absorption properties of PEEK/Al_2O_3 films by producing films with varying alumina compositions, to understand the effects of the ceramic on the water absorption properties of the devices.

7. Produce in-situ composites of PEEK and other ceramics, like silicon carbide and titanium oxide, and assess their mechanical and electrical properties. Alumina assisted with the deposition of PEEK via CGDS, but other ceramic materials could potentially have the same effect and additionally, offer better advantages in terms of power generation and cost.

8. Standardize the testing method of the MEET devices by precisely controlling the size of the droplets of water and their positioning on the PEEK film.

9. Study the surface energy and contact angle of water droplets with the PEEK/ceramic film to better comprehend the surface wetting mechanism.

10. Study the effect of crystallinity and amorphousness of PEEK on the properties of the manufactured MEET devices by comparing the crystallinity values of the feedstock powder and the sprayed coating, and introducing quenching and heat-treatment of the deposited films. The electrical properties of the MEET devices can therefore be further controlled and optimized, and the CGDS process parameters finely tuned.

11. Perform microscopic and spectroscopic analyses of the MEET devices before and after exposure to moisture, in order to assess any degradation mechanisms that take place, like corrosion and fatigue due to cyclic density changes.

References

[1] Global System for Mobile Communications Association, “Understanding the Internet of Things (IoT),” London, UK, Jul. 2014.

[2] Y.-K. Chen, “Challenges and Opportunities of Internet of Things,” in *17th Asia and South Pacific Design Automation Conference*, Sydney, Australia, 2012, pp. 383–388.

[3] R. Khan *et al.*, “Future Internet: The Internet of Things Architecture, Possible Applications and Key Challenges,” in *2012 10th International Conference on Frontiers of Information Technology*, Islamabad, Pakistan, 2012, pp. 257–260.

[4] K. S. Yeo *et al.*, “Internet of Things: Trends, Challenges and Applications,” in *2014 International Symposium on Integrated Circuits (ISIC)*, Singapore, 2014, pp. 568–571.

[5] W. Ejaz *et al.*, “Efficient Energy Management for the Internet of Things in Smart Cities,” *IEEE Commun. Mag.*, vol. 55, no. 1, pp. 84–91, Jan. 2017.

[6] M. Casini, “Internet of Things for Energy Efficiency of Buildings,” *Archit. Eng.*, p. 5.

[7] H. Jayakumar *et al.*, “Powering the Internet of Things,” in *Proceedings of the 2014 International Symposium on Low Power Electronics and Design - ISLPED ’14*, La Jolla, California, USA, 2014, pp. 375–380.

[8] C. Zhu *et al.*, “Green Internet of Things for Smart World,” *IEEE Access*, vol. 3, pp. 2151–2162, 2015.

[9] S. C. Mukhopadhyay, Ed., *Internet of Things: Challenges and Opportunities*. Cham: Springer, 2014.

[10] R. J. Bord *et al.*, “Public Perceptions of Global Warming: United States and International Perspectives,” *Clim Res*, p. 10, 1998.

[11] M. Gorlatova *et al.*, “Movers and Shakers: Kinetic Energy Harvesting for the Internet of Things,” *IEEE J. Sel. Areas Commun.*, vol. 33, no. 8, pp. 1624–1639, Aug. 2015.

[12] N. S. Shenck *et al.*, “Energy Scavenging with Shoe-Mounted Piezoelectrics,” *IEEE Micro*, vol. 21, no. 3, pp. 30–42, Jun. 2001.

[13] F. Zhao *et al.*, “Direct Power Generation from a Graphene Oxide Film Under Moisture,” *Adv. Mater.*, vol. 27, no. 29, pp. 4351–4357, Aug. 2015.

[14] H. Cheng *et al.*, “Flexible In-Plane Graphene Oxide Moisture-Electric Converter for Touchless Interactive Panel,” *Nano Energy*, vol. 45, pp. 37–43, Mar. 2018.

[15] Y. Huang *et al.*, “Highly Efficient Moisture-Triggered Nanogenerator Based on Graphene Quantum Dots,” *ACS Appl. Mater. Interfaces*, vol. 9, no. 44, pp. 38170–38175, Nov. 2017.

[16] F. Zhao *et al.*, “Graphene Oxide Nanoribbon Assembly Toward Moisture-Powered Information Storage,” *Adv. Mater.*, vol. 29, no. 3, p. 1604972, Jan. 2017.

[17] F. Zhao *et al.*, “Highly Efficient Moisture-Enabled Electricity Generation from Graphene Oxide Frameworks,” *Energy Environ. Sci.*, vol. 9, no. 3, pp. 912–916, 2016.

[18] J. Liu *et al.*, “Moisture-Enabled Electricity Generation from Gradient Polyoxometalates-Modified Sponge-Like Graphene Oxide Monolith,” *J. Mater. Sci.*, vol. 54, no. 6, pp. 4831–4841, Mar. 2019.

[19] D. Shen *et al.*, “Self-Powered Wearable Electronics Based on Moisture Enabled Electricity Generation,” *Adv. Mater.*, vol. 30, no. 18, p. 1705925, May 2018.

[20] P. Dhiman *et al.*, “Harvesting Energy from Water Flow Over Graphene,” *Nano Lett.*, vol. 11, no. 8, pp. 3123–3127, Aug. 2011.

[21] A. Vittori, “Warka Water,” *Warka Water, Every Drop Counts*, 13-Aug-2019. [Online]. Available: http://www.warkawater.org/. [Accessed: 13-Aug-2019].

[22] M. A. Grayson *et al.*, “The Solubility and Diffusion of Water in Poly(Aryl-Ether-Ether-Ketone) (PEEK),” *J. Polym. Sci. Part B Polym. Phys.*, vol. 25, no. 1, pp. 31–41, Jan. 1987.

[23] G. Mensitieri *et al.*, “Water Sorption Kinetics in Poly(Aryl Ether Ether Ketone),” *J. Appl. Polym. Sci.*, vol. 37, no. 2, pp. 381–392, Jan. 1989.

[24] A. Buchman *et al.*, “Water Absorption of some Thermoplastic Composites,” p. 9.

[25] J. Grasmeder, “Victrex | A Closer Peek at PEEK.” [Online]. Available: https://www.victrex.com/en/blog/2017/a-closer-peek-at-peek. [Accessed: 09-Apr-2019].

[26] S. X. Lu *et al.*, “Thermal Stability and Thermal Expansion Studies of PEEK and Related Polyimides,” *Polymer*, vol. 37, no. 14, pp. 2999–3009, Jul. 1996.

[27] K. Bigham, “Powering Motor Performance: An Introduction to PEEK Extrusions,” *Zeus*, p. 11, 2017.

[28] K. J. Bigham, “New Focus on PEEK,” *Zeus*, p. 11, Oct. 2018.

[29] R. May, “Polyetheretherketones,” in *Encyclopedia of Polymer Science and Technology*, John Wiley & Sons, Inc., ed. Hoboken, NJ, USA: John Wiley & Sons, Inc., 2008.

[30] H. Zhang, “Fire-Safe Polymers and Polymer Composites,” Office of Aviation Research, Washington, DC, DOT/FAA/AR-04/11, Sep. 2004.

[31] J. B. Rose *et al.*, “Thermoplastic Aromatic Polyetherketones.”, 4320224, Mar. 1982.

[32] J. Perry *et al.*, “Pin Fin Array Heat Sinks by Cold Spray Additive Manufacturing: Economics of Powder Recycling,” *J. Therm. Spray Technol.*, vol. 28, no. 1–2, pp. 144–160, Jan. 2019.

[33] R. N. Raoelison *et al.*, “Cold Gas Dynamic Spray Additive Manufacturing Today: Deposit Possibilities, Technological Solutions and Viable Applications,” *Mater. Des.*, vol. 133, pp. 266–287, 2017.

[34] Y. Hu *et al.*, “Cold Gas-Dynamic Spray Repair on Gas Turbine Engine Components,” Jun-2005.

[35] A. W. James *et al.*, “Cold Spray Repair Process,” Dec-2002.

[36] W. Li *et al.*, “Solid-State Additive Manufacturing and Repairing by Cold Spraying: A Review,” *J. Mater. Sci. Technol.*, vol. 34, no. 3, pp. 440–457, Mar. 2018.

[37] S. Pathak *et al.*, “Development of Sustainable Cold Spray Coatings and 3D Additive Manufacturing Components for Repair/Manufacturing Applications: A Critical Review,” *Coatings*, vol. 7, no. 8, p. 122, Aug. 2017.

[38] S. Yin *et al.*, “Cold Spray Additive Manufacturing and Repair: Fundamentals and Applications,” *Addit. Manuf.*, vol. 21, pp. 628–650, May 2018.

[39] Y. Cormier *et al.*, “Finite Element Analysis and Failure Mode Characterization of Pyramidal Fin Arrays Produced by Masked Cold Gas Dynamic Spray,” *J. Therm. Spray Technol.*, vol. 24, no. 8, pp. 1549–1565, Dec. 2015.

[40] Y. Cormier *et al.*, “Additive Manufacturing of Pyramidal Pin Fins: Height and Fin Density Effects Under Forced Convection,” *Int. J. Heat Mass Transf.*, vol. 75, pp. 235–244, 2014.

[41] Y. Cormier *et al.*, “Net Shape Fins for Compact Heat Exchanger Produced by Cold Spray,” *J. Therm. Spray Technol.*, vol. 22, no. 7, pp. 1210–1221, Oct. 2013.

[42] Y. Cormier *et al.*, “Pyramidal Fin Arrays Performance Using Streamwise Anisotropic Materials by Cold Spray Additive Manufacturing,” *J. Therm. Spray Technol.*, vol. 25, no. 1–2, pp. 170–182, Jan. 2016.

[43] P. Dupuis *et al.*, “Heat Transfer and Flow Structure Characterization for Pin Fins Produced by Cold Spray Additive Manufacturing,” *Int. J. Heat Mass Transf.*, vol. 98, pp. 650–661, 2016.

[44] C. A. Howells, “Piezoelectric Energy Harvesting,” *Energy Convers. Manag.*, vol. 50, no. 7, pp. 1847–1850, Jul. 2009.

[45] E. Lefeuvre *et al.*, “Piezoelectric Energy Harvesting Device Optimization by Synchronous Electric Charge Extraction,” *J. Intell. Mater. Syst. Struct.*, vol. 16, no. 10, pp. 865–876, Oct. 2005.

[46] Y. C. Shu *et al.*, “Analysis of Power Output for Piezoelectric Energy Harvesting Systems,” *Smart Mater. Struct.*, vol. 15, no. 6, pp. 1499–1512, Dec. 2006.

[47] H. A. Sodano *et al.*, “Comparison of Piezoelectric Energy Harvesting Devices for Recharging Batteries,” *J. Intell. Mater. Syst. Struct.*, vol. 16, no. 10, pp. 799–807, Oct. 2005.

[48] H. A. Sodano *et al.*, “Estimation of Electric Charge Output for Piezoelectric Energy Harvesting,” *Strain*, vol. 40, no. 2, pp. 49–58, May 2004.

[49] J. Chen *et al.*, “Reviving Vibration Energy Harvesting and Self-Powered Sensing by a Triboelectric Nanogenerator,” *Joule*, vol. 1, no. 3, pp. 480–521, Nov. 2017.

[50] F.-R. Fan *et al.*, “Flexible Triboelectric Generator,” *Nano Energy*, vol. 1, no. 2, pp. 328–334, Mar. 2012.

[51] T.-C. Hou *et al.*, “Triboelectric Nanogenerator Built Inside Shoe Insole for Harvesting Walking Energy,” *Nano Energy*, vol. 2, no. 5, pp. 856–862, Sep. 2013.

[52] L. Lin *et al.*, “Segmentally Structured Disk Triboelectric Nanogenerator for Harvesting Rotational Mechanical Energy,” *Nano Lett.*, vol. 13, no. 6, pp. 2916–2923, Jun. 2013.

[53] X. Pu *et al.*, “Ultrastretchable, Transparent Triboelectric Nanogenerator as Electronic Skin for Biomechanical Energy Harvesting and Tactile Sensing,” *Sci. Adv.*, vol. 3, no. 5, p. E1700015, May 2017.

[54] Y. Yang *et al.*, “Human Skin Based Triboelectric Nanogenerators for Harvesting Biomechanical Energy and as Self-Powered Active Tactile Sensor System,” *ACS Nano*, vol. 7, no. 10, pp. 9213–9222, Oct. 2013.

[55] W. Guo *et al.*, “Bio-Inspired Two-Dimensional Nanofluidic Generators Based on a Layered Graphene Hydrogel Membrane,” *Adv. Mater.*, vol. 25, no. 42, pp. 6064–6068, Nov. 2013.

[56] S. Ghosh *et al.*, “Carbon Nanotube Flow Sensors,” vol. 299, p. 4, 2003.

[57] J. Lao *et al.*, “Flow-Induced Voltage Generation in Graphene Network,” *Nano Res.*, vol. 8, no. 8, pp. 2467–2473, Aug. 2015.

[58] Y. Xu *et al.*, “Generating Electricity from Water Through Carbon Nanomaterials,” *Chem. - Eur. J.*, vol. 24, no. 24, pp. 6287–6294, Apr. 2018.

[59] O. Goushcha *et al.*, “Interactions of Vortices with a Flexible Beam with Applications in Fluidic Energy Harvesting,” *Appl. Phys. Lett.*, vol. 104, no. 2, p. 21919, Jan. 2014.

[60] Y. Liang *et al.*, “Electric Power Generation via Asymmetric Moisturizing of Graphene Oxide for Flexible, Printable and Portable Electronics,” *Energy Environ. Sci.*, vol. 11, no. 7, pp. 1730–1735, 2018.

[61] G. Xue *et al.*, “Water-Evaporation-Induced Electricity with Nanostructured Carbon Materials,” *Nat. Nanotechnol.*, vol. 12, no. 4, pp. 317–321, May 2017.

[62] H. Cheng *et al.*, “Graphene-Based Functional Architectures: Sheets Regulation and Macrostructure Construction Toward Actuators and Power Generators,” *Acc. Chem. Res.*, vol. 50, no. 7, pp. 1663–1671, Jul. 2017.

[63] J. Xue *et al.*, “Vapor-Activated Power Generation on Conductive Polymer,” *Adv. Funct. Mater.*, vol. 26, no. 47, pp. 8784–8792, Dec. 2016.

[64] VICTREX®, “VICTREX® PEEK 150G / 151G,” *VICTREX® Datasheets*, VICTREX®, 2019.

[65] T. W. Giants, “Crystallinity and Dielectric Properties of PEEK, Poly(Ether Ether Ketone),” *IEEE Trans. Dielectr. Electr. Insul.*, vol. 1, no. 6, pp. 991–999, Dec. 1994.

[66] D. Kemmish, *Update on the Technology and Applications of Polyaryletherketones*. Shawbury: Ismithers, 2010.

[67] W. D. Callister, *Materials Science and Engineering: An Introduction*, 6th ed. New York, NY: John Wiley & Sons, 2003.

[68] D. J. Kemmish, *Practical Guide to High Performance Engineering Plastics*. Shawbury: Ismithers, 2011.

[69] M. C. Kuo *et al.*, “PEEK Composites Reinforced by Nano-Sized SiO_2 and Al_2O_3 Particulates,” *Mater. Chem. Phys.*, vol. 90, no. 1, pp. 185–195, Mar. 2005.

[70] J. Sandler *et al.*, “Carbon-Nanofibre-Reinforced Poly(Ether Ether Ketone) Composites,” *Compos. Part Appl. Sci. Manuf.*, vol. 33, no. 8, pp. 1033–1039, Aug. 2002.

[71] A. Saleem *et al.*, “High Performance Thermoplastic Composites: Study on the Mechanical, Thermal, and Electrical Resistivity Properties of Carbon Fiber-Reinforced Polyetheretherketone and Polyethersulphone,” *Polym. Compos.*, vol. 28, no. 6, pp. 785–796, Dec. 2007.

[72] R. K. Goyal *et al.*, “Thermal Expansion Behaviour of High Performance PEEK Matrix Composites,” *J. Phys. Appl. Phys.*, vol. 41, no. 8, p. 85403, Apr. 2008.

[73] VICTREX®, “Chemical Resistance, VICTREX® PEEK Polymers.” *VICTREX® Datasheets*, VICTREX®, 2019.

[74] J. Ho *et al.*, “Effect of Crystallinity and Morphology on Dielectric Properties of PEEK at Elevated Temperature,” in *2013 IEEE International Conference on Solid Dielectrics (ICSD)*, Bologna, Italy, 2013, pp. 385–388.

[75] S. Kaliaguine *et al.*, “Properties of SPEEK Based Pems for Fuel Cell Application,” *Catal. Today*, vol. 82, no. 1–4, pp. 213–222, Jul. 2003.

[76] L. Li, “Sulfonated Poly(Ether Ether Ketone) Membranes for Direct Methanol Fuel Cell,” *J. Membr. Sci.*, vol. 226, no. 1–2, pp. 159–167, Dec. 2003.

[77] M. Gil *et al.*, “Direct Synthesis of Sulfonated Aromatic Poly(Ether Ether Ketone) Proton Exchange Membranes for Fuel Cell Applications,” *J. Membr. Sci.*, vol. 234, no. 1–2, pp. 75–81, May 2004.

[78] Z. Gaowen *et al.*, “Organic/Inorganic Composite Membranes for Application in DMFC,” *J. Membr. Sci.*, vol. 261, no. 1–2, pp. 107–113, Sep. 2005.

[79] S. M. Zaidi *et al.*, “Proton Conducting Composite Membranes from Polyether Ether Ketone and Heteropolyacids for Fuel Cell Applications,” *J. Membr. Sci.*, vol. 173, no. 1, pp. 17–34, Jul. 2000.

[80] A. Basile *et al.*, “Sulfonated PEEK-WC Membranes for Proton-Exchange Membrane Fuel Cell: Effect of the Increasing Level of Sulfonation on Electrochemical Performances,” *J. Membr. Sci.*, vol. 281, no. 1–2, pp. 377–385, Sep. 2006.

[81] T. Maharana *et al.*, “Polyetheretherketone (PEEK) Membrane for Fuel Cell Applications,” in *Advanced Energy Materials*, A. Tiwari and S. Valyukh, Eds. Hoboken, NJ, USA: John Wiley & Sons, Inc., 2014, pp. 433–464.

[82] M. Rikukawa *et al.*, “Proton-Conducting Polymer Electrolyte Membranes Based on Hydrocarbon Polymers,” *Prog Polym Sci*, p. 40, 2000.

[83] H. Mehrer, *Diffusion in Solids: Fundamentals, Methods, Materials, Diffusion-Controlled Processes*. Berlin ; New York: Springer, 2007.

[84] J. Crank, *The Mathematics of Diffusion*, 2. ed., Reprinted. Oxford: Oxford Univ. Press, 2009.

[85] G. Allen *et al.*, “Relaxation Phenomena in some Aromatic Polymers: Effect of Water Content on the Low Temperature Relaxation,” *Polymer*, vol. 12, no. 2, pp. 85–100, Feb. 1971.

[86] R. D. Priestley, “Structural Relaxation of Polymer Glasses At Surfaces, Interfaces, and in Between,” *Science*, vol. 309, no. 5733, pp. 456–459, Jul. 2005.

[87] H. Ardebili *et al.*, “Characterization of Encapsulant Properties,” in *Encapsulation Technologies for Electronic Applications*, Elsevier, 2019, pp. 221–258.

[88] C. J. Tsenoglou *et al.*, “Evaluation of Interfacial Relaxation Due to Water Absorption in Fiber–Polymer Composites,” *Compos. Sci. Technol.*, vol. 66, no. 15, pp. 2855–2864, Dec. 2006.

[89] X. Lu *et al.*, “Moisture-Absorption, Dielectric Relaxation, and Thermal Conductivity Studies of Polymer Composites,” p. 7.

[90] J. Comyn, *Polymer Permeability*. London: Elsevier Applied Science, 1985.

[91] J. Clayden *et al.*, *Organic Chemistry*, 2nd ed. Oxford ; New York: Oxford University Press, 2012.

[92] Natural Resources Canada, “Minerals and Metals Fact Book,” 2016.

[93] J. R. Davis, Ed., *Alloying: Understanding the Basics*. Materials Park, OH: ASM International, 2001.

[94] J. G. Kaufman, *Introduction to Aluminum Alloys and Tempers*. Materials Park, OH: ASM International, 2000.

[95] S. Fickling, “The Capacitor Book,” p. 158.

[96] A. Papyrin, “The Development of the Cold Spray Process,” in *The Cold Spray Materials Deposition Process*, Elsevier, 2007, pp. 11–42.

[97] A. P. Alkhimov *et al.*, “Gas Dynamic Spraying Method for Applying a Coating,” 5302414.

[98] J. Villafuerte, *Modern Cold Spray: Materials, Process, and Applications*. 2015.

[99] V. K. Champagne, Ed., *The Cold Spray Materials Deposition Process: Fundamentals and Applications*. Cambridge: Woodhead, 2007.

[100] R. C. Dykhuizen *et al.*, “Impact of High Velocity Cold Spray Particles,” *J. Therm. Spray Technol.*, vol. 8, no. 4, pp. 559–564, Dec. 1999.

[101] T. Hussain *et al.*, “Bonding Mechanisms in Cold Spraying: The Contributions of Metallurgical and Mechanical Components,” *J. Therm. Spray Technol.*, vol. 18, no. 3, pp. 364–379, 2009.

[102] A. Nastic *et al.*, “Experimental and Numerical Study of the Influence of Substrate Surface Preparation on Adhesion Mechanisms of Aluminum Cold Spray Coatings on 300M Steel Substrates,” *J. Therm. Spray Technol.*, vol. 26, no. 7, pp. 1461–1483, Oct. 2017.

[103] M. Grujicic *et al.*, “Adiabatic Shear Instability Based Mechanism for Particles/Substrate Bonding in the Cold-Gas Dynamic-Spray Process,” *Mater. Des.*, vol. 25, no. 8, pp. 681–688, Dec. 2004.

[104] H. Assadi *et al.*, “Bonding Mechanism in Cold Gas Spraying,” *Acta Mater.*, vol. 51, no. 15, pp. 4379–4394, Sep. 2003.

[105] T. Samson *et al.*, “Effect of Pulsed Waterjet Surface Preparation on the Adhesion Strength of Cold Gas Dynamic Sprayed Aluminum Coatings,” *J. Therm. Spray Technol.*, vol. 24, no. 6, pp. 984–993, Aug. 2015.

[106] T. Marrocco *et al.*, “Production of Titanium Deposits by Cold-Gas Dynamic Spray: Numerical Modeling and Experimental Characterization,” *J. Therm. Spray Technol.*, vol. 15, no. 2, pp. 263–272, Jun. 2006.

[107] W.-Y. Li *et al.*, “Study on Impact Fusion At Particle Interfaces and its Effect on Coating Microstructure in Cold Spraying,” *Appl. Surf. Sci.*, vol. 254, no. 2, pp. 517–526, Nov. 2007.

[108] T. Schmidt *et al.*, “Development of a Generalized Parameter Window for Cold Spray Deposition,” *Acta Mater.*, vol. 54, no. 3, pp. 729–742, 2006.

[109] T. Schmidt *et al.*, “From Particle Acceleration to Impact and Bonding in Cold Spraying,” *J. Therm. Spray Technol.*, vol. 18, no. 5–6, pp. 794–808, Dec. 2009.

[110] ASTM Standard, “ASTM 633-79 Standard Test Method for Adhesion or Cohesion Strength of Thermal Spray Coatings,” vol. 3, reapproved, pp. 1–7, 1979.

[111] “Accepted Practice to Test Bond Strength of Thermal Spray Coatings,” *J. Therm. Spray Technol.*, vol. 22, no. 8, pp. 1263–1266, Dec. 2013.

[112] D01 Committee, “Test Method for Pull-Off Strength of Coatings Using Portable Adhesion Testers,” ASTM International.

[113] C.-J. Li *et al.*, “Influence of Spray Materials and Their Surface Oxidation on the Critical Velocity in Cold Spraying,” *J. Therm. Spray Technol.*, vol. 19, no. 1–2, pp. 95–101, Jan. 2010.

[114] C.-J. Li *et al.*, “Examination of the Critical Velocity for Deposition of Particles in Cold Spraying,” *J. Therm. Spray Technol.*, vol. 15, no. 2, pp. 212–222, Jun. 2006.

[115] X.-J. Ning *et al.*, “Numerical Study of In-Flight Particle Parameters in Low-Pressure Cold Spray Process,” *J. Therm. Spray Technol.*, vol. 19, no. 6, pp. 1211–1217, Dec. 2010.

[116] T. Schmidt *et al.*, “New Developments in Cold Spray Based on Higher Gas and Particle Temperatures,” *J. Therm. Spray Technol.*, vol. 15, no. 4, pp. 488–494, Dec. 2006.

[117] J. Wu *et al.*, “Measurement of Particle Velocity and Characterization of Deposition in Aluminum Alloy Kinetic Spraying Process,” *Appl. Surf. Sci.*, vol. 252, no. 5, pp. 1368–1377, Dec. 2005.

[118] T. Stoltenhoff *et al.*, “An Analysis of the Cold Spray Process and its Coatings,” *J. Therm. Spray Technol.*, vol. 11, no. 4, pp. 542–550, Dec. 2002.

[119] J. G. Legoux *et al.*, “Effect of Substrate Temperature on the Formation Mechanism of Cold-Sprayed Aluminum, Zinc and Tin Coatings,” *J. Therm. Spray Technol.*, vol. 16, no. 5–6, pp. 619–626, Dec. 2007.

[120] D. L. Gilmore *et al.*, “Particle Velocity and Deposition Efficiency in the Cold Spray Process,” *J. Therm. Spray Technol.*, vol. 8, no. 4, pp. 576–582, Dec. 1999.

[121] R. W. Fox *et al.*, *Fox and Mcdonald’s Introduction to Fluid Mechanics*, 8th ed. Hoboken, NJ : Chichester: John Wiley & Sons, Inc. ; John Wiley [Distributor], 2011.

[122] Y. Nakayama *et al.*, *Introduction to Fluid Mechanics*. London : New York: Arnold ; J. Wiley & Sons, 1999.

[123] H. Fukanuma *et al.*, “In-Flight Particle Velocity Measurements with DPV-2000 in Cold Spray,” *Surf. Coat. Technol.*, vol. 201, no. 5, pp. 1935–1941, Oct. 2006.

[124] M. Winnicki *et al.*, “Numerical and Experimental Analysis of Copper Particles Velocity in Low-Pressure Cold Spraying Process,” *Surf. Coat. Technol.*, vol. 268, pp. 230–240, Apr. 2015.

[125] R. Huang *et al.*, “Study of the Influence of Particle Velocity on Adhesive Strength of Cold Spray Deposits,” *J. Therm. Spray Technol.*, vol. 21, no. 3–4, pp. 541–549, Jun. 2012.

[126] R. C. Dykhuizen *et al.*, “Gas Dynamic Principles of Cold Spray,” *J. Therm. Spray Technol.*, vol. 7, no. 2, pp. 205–212, Jun. 1998.

[127] P. A. Durbin *et al.*, *Fluid Dynamics with a Computational Perspective*. Oxford ; New York: Cambridge University Press, 2007.

[128] B. Jodoin, “Cold Spray Nozzle Mach Number Limitation,” *J. Therm. Spray Technol.*, vol. 11, no. 4, pp. 496–507, Dec. 2002.

[129] K. Taylor *et al.*, “Particle Loading Effect in Cold Spray,” *J. Therm. Spray Technol.*, vol. 15, no. 2, pp. 273–279, Jun. 2006.

[130] M. Fukumoto *et al.*, “Effect of Substrate Temperature on Deposition Behavior of Copper Particles on Substrate Surfaces in the Cold Spray Process,” *J. Therm. Spray Technol.*, vol. 16, no. 5–6, pp. 643–650, Dec. 2007.

[131] W.-Y. Li *et al.*, “Effect of Standoff Distance on Coating Deposition Characteristics in Cold Spraying,” *Mater. Des.*, vol. 29, no. 2, pp. 297–304, Jan. 2008.

[132] J. Pattison *et al.*, “Standoff Distance and Bow Shock Phenomena in the Cold Spray Process,” *Surf. Coat. Technol.*, vol. 202, no. 8, pp. 1443–1454, 2008.

[133] R. Gonzalez *et al.*, “A Review of Thermal Spray Metallization of Polymer-Based Structures,” *J. Therm. Spray Technol.*, vol. 25, no. 5, pp. 897–919, Jun. 2016.

[134] M. Gardon *et al.*, “Cold Gas Spray Titanium Coatings onto a Biocompatible Polymer,” *Mater. Lett.*, vol. 106, pp. 97–99, Sep. 2013.

[135] A. Ganesan *et al.*, “Cold Spray Coating Deposition Mechanism on the Thermoplastic and Thermosetting Polymer Substrates,” *J. Therm. Spray Technol.*, vol. 22, no. 8, pp. 1275–1282, Dec. 2013.

[136] R. Lupoi *et al.*, “Deposition of Metallic Coatings on Polymer Surfaces Using Cold Spray,” *Surf. Coat. Technol.*, vol. 205, no. 7, pp. 2167–2173, 2010.

[137] P. C. King *et al.*, “Embedment of Copper Particles Into Polymers by Cold Spray,” *Surf. Coat. Technol.*, vol. 216, pp. 60–67, Feb. 2013.

[138] D. Giraud *et al.*, “Metallization of a Polymer Using Cold Spray: Application to Aluminum Coating of Polyamide 66,” p. 7.

[139] C. Chen *et al.*, “Metallization of Polyether Ether Ketone (PEEK) by Copper Coating Via Cold Spray,” *Surf. Coat. Technol.*, vol. 342, pp. 209–219, May 2018.

[140] X. L. Zhou *et al.*, “Preparation of Metallic Coatings on Polymer Matrix Composites by Cold Spray,” *Surf. Coat. Technol.*, vol. 206, no. 1, pp. 132–136, Oct. 2011.

[141] N. Sanpo *et al.*, “Antibacterial Property of Cold-Sprayed HA-Ag/PEEK Coating,” *J. Therm. Spray Technol.*, vol. 18, no. 1, pp. 10–15, Mar. 2009.

[142] Y. Xu *et al.*, “Cold Spray Deposition of Thermoplastic Powder,” *Surf. Coat. Technol.*, vol. 201, no. 6, pp. 3044–3050, Dec. 2006.

[143] A. S. Alhulaifi *et al.*, “Numerical and Experimental Investigation of Cold Spray Gas Dynamic Effects for Polymer Coating,” *J. Therm. Spray Technol.*, vol. 21, no. 5, pp. 852–862, Sep. 2012.

[144] A. Sturgeon *et al.*, “Cold Sprayed Coatings for Polymer Composite Substrates,” p. 5.

[145] K. I. Triantou *et al.*, “Microstructure and Tribological Behavior of Copper and Composite Copper + Alumina Cold Sprayed Coatings for Various Alumina Contents,” *Wear*, vol. 336–337, pp. 96–107, Aug. 2015.

[146] R. Fernandez *et al.*, “Cold Spray Aluminum–Alumina Cermet Coatings: Effect of Alumina Content,” *J. Therm. Spray Technol.*, vol. 27, no. 4, pp. 603–623, Apr. 2018.

[147] E. Sansoucy *et al.*, “Properties of SiC-Reinforced Aluminum Alloy Coatings Produced by the Cold Gas Dynamic Spraying Process,” *Surf. Coat. Technol.*, vol. 202, no. 16, pp. 3988–3996, May 2008.

[148] E. Irissou *et al.*, “Investigation of Al-Al_2O_3 Cold Spray Coating Formation and Properties,” *J. Therm. Spray Technol.*, vol. 16, no. 5–6, pp. 661–668, Dec. 2007.

[149] F. Sevillano *et al.*, “Cold-Sprayed Ni-Al_2O_3 Coatings for Applications in Power Generation Industry,” *J. Therm. Spray Technol.*, vol. 22, no. 5, pp. 772–782, Jun. 2013.

[150] E. Petrovicova *et al.*, “Thermal Spraying of Polymers,” *Int. Mater. Rev.*, vol. 47, no. 4, pp. 169–190, Aug. 2002.

[151] H. Che *et al.*, “Metallization of Carbon Fibre Reinforced Polymers by Cold Spray,” *Surf. Coat. Technol.*, vol. 313, pp. 236–247, Mar. 2017.

[152] A. J. C. Wilson, “The Thermal Expansion of Aluminium from 0 to 650 ℃,” *Proc. Phys. Soc.*, vol. 53, no. 3, pp. 235–244, May 1941.

[153] S. Rech *et al.*, “Influence of Pre-Heated Al 6061 Substrate Temperature on the Residual Stresses of Multipass Al Coatings Deposited by Cold Spray,” *J. Therm. Spray Technol.*, vol. 20, no. 1–2, pp. 243–251, Jan. 2011.

[154] R. M. German, *Particulate Composites*. New York, NY: Springer Science + Business Media, 2016.

[155] J. R. Davis *et al.*, Eds., *Aluminum and Aluminum Alloys*. Materials Park, OH: ASM International, 1993.

[156] M. Diab *et al.*, “The Effect of Pure Aluminum Cold Spray Coating on Corrosion and Corrosion Fatigue of Magnesium (3% Al-1% Zn) Extrusion,” *Surf. Coat. Technol.*, vol. 309, pp. 423–435, Jan. 2017.

[157] R. Ghelichi *et al.*, “Microstructure and Fatigue Behavior of Cold Spray Coated Al5052,” *Acta Mater.*, vol. 60, no. 19, pp. 6555–6561, Nov. 2012.

[158] T. Suhonen *et al.*, “Residual Stress Development in Cold Sprayed Al, Cu and Ti Coatings,” *Acta Mater.*, vol. 61, no. 17, pp. 6329–6337, 2013.

[159] K. Ogawa *et al.*, “Characterization of Low-Pressure Cold-Sprayed Aluminum Coatings,” *J. Therm. Spray Technol.*, vol. 17, no. 5–6, pp. 728–735, Dec. 2008.

[160] W.-Y. Li *et al.*, “Numerical Simulation of Deformation Behavior of Al Particles Impacting on Al Substrate and Effect of Surface Oxide Films on Interfacial Bonding in Cold Spraying,” *Appl. Surf. Sci.*, vol. 253, no. 11, pp. 5084–5091, Mar. 2007.

[161] S. Yin *et al.*, “Interfacial Bonding Features of Ni Coating on Al Substrate with Different Surface Pretreatments in Cold Spray,” *Mater. Lett.*, vol. 138, pp. 143–147, Jan. 2015.

[162] C. M. Forman, “Practical Galvanic Series,” Redstone Arsenal, Alabama, RS-TR.67-11.

[163] S. Ebnesajjad *et al.*, *Surface Treatment of Materials for Adhesive Bonding*, Second Edition. Amsterdam: William Andrew, An Imprint of Elsevier, 2014.

[164] S. Kim *et al.*, “Polyetheretherketone (PEEK) Surface Functionalization by Low-Energy Ion-Beam Irradiation Under a Reactive O_2 Environment and its Effect on the PEEK/Copper Adhesives,” *Langmuir*, vol. 20, no. 1, pp. 157–163, Jan. 2004.

[165] K. J. Kubiak *et al.*, “Wettability Versus Roughness of Engineering Surfaces,” *Wear*, vol. 271, no. 3–4, pp. 523–528, Jun. 2011.

[166] R. Gill, *Chemical Fundamentals of Geology and Environmental Geoscience*, Third Edition. Chichester, West Sussex: John Wiley & Sons, Inc, 2015.

[167] W. C. Conner *et al.*, Eds. Fluid Transport in Nanoporous Materials, *Proceedings of the NATO Advanced Study Institute on Fluid Transport in Nanoporous Materials, La Colle Sur Loup, France, 16 - 28 June 2003*. Dordrecht: Springer, 2006.

Appendix A: Arduino Code

```
void setup() {
Serial.begin(9600);
}

void loop() {
//Read from Analog In 1
int val = analogRead(1);
while(1){
  //Print the input voltage in mV
  Serial.println(val/1023.0*5.0*1000);
  //Delay 200 ms
  delay(200);
  //Read Analog In 1
  val = analogRead(1);
}
Serial.println(val/1023.0*5.0*1000);
}
```

Appendix B: Polishing Procedure

	Surface	Suspension/ Lubricant	Suspension size (μm)	Process time	Force per sample [N]	Disc rotation speed [RPM]	Sample holder speed [RPM]
1	Piano 220	Water	N/A	2m00s	25	300	100
2	Largo	Largo	9	4m00s	25	150	50
3	Mol	Mol	3	5m00s	15	150	150
4	Chem	OP-S	0.05	2m00s	10	150	100
5	Chem	Water	N/A	2m40s	10	150	100

Clockwise	Counter-clockwise